Development of an Implosion-Driven Hypervelocity Launcher for Orbital Debris Impact Simulation

Justin Huneault

Masters of Engineering

Department of Mechanical Engineering

McGill University

Montreal, Quebec

April 16, 2013

A thesis submitted to the
Faculty of Graduate Studies and Research
In partial fulfilment of the requirements of the degree
Master of Engineering

ACKNOWLEDGEMENTS

I would like to begin by thanking my supervisor, Andrew Higgins, for his support, guidance, and passion for this project. His willingness to take me on as a graduate student under difficult circumstances, his belief in my abilities, as well as his desire to push me to achieve my full potential have been instrumental to the success of my research. I also owe a great deal of gratitude to Jason Loiseau for his continued support throughout my Masters work. His help in introducing me to the project, performing launcher experiments, and developing a design framework for the launcher has been invaluable. I would also like to thank Vincent Tanguay for his help in introducing me to the world of gasdynamics and getting me started on the right path. I would also like to acknowledge the help and support of the entire SWPG group. The help, thoughtful discussion, criticism, and camaraderie have been an important part of my experience. I would also like to thank the mechanical engineering technical staff, notably Gary Savard, John Boisvert, Tony Micozzi, Andy Hoffman, and Mathieu Beauchesne, for their help in the fabrication and execution of launcher experiments. Finally, I would like to thank my family for their unwavering support, my friends for the good times that make it all worth it, and Melissa for her love and patience.

ABSTRACT

The ability to soft-launch projectiles to velocities exceeding 10 km/s is of interest for a number of scientific fields, including orbital debris impact testing. Current soft-launch technologies have reached a performance plateau below this operating range. In the implosion-driven launcher (IDL) concept, explosives are used to linearly implode a pressurized steel tube, thereby dynamically compressing a light driver gas to significantly higher pressures and temperatures than typical light-gas launchers. As a result, the IDL has the potential to significantly outperform current state of the art hypervelocity launchers. This work will focus on establishing an understanding of the critical design parameters of the IDL with the goal of improving the velocity potential of the launcher. For this purpose, a computational gasdynamics solver capable of simulating the internal ballistics of the IDL has been developed. The elevated pressure and temperature in the driver gas lead to a number of non-ideal effects during the launch cycle, including expansion of the launcher walls, convective heat transfer, and gas leakage, which have a significant effect on launcher performance. These effects have been simulated by coupling the gasdynamics solver to loss models. Specifically, a structural hydrocode has been developed to provide a realistic model of reservoir and launch tube expansion, which has been identified as the main source of performance loss in the launch cycle. The complete internal ballistics solver will be used in conjunction with classical internal ballistics theory and experimental results, in order to gain valuable understanding of the key design parameters of the launcher and improve the design of the McGill IDL. This analysis has led to the development of an IDL capable of launching a 0.1-g projectile to 9.1 km/s.

ABRÉGÉ

La capacité d'accéléré des projectiles à des vitesses au-delà de 10 km/s est d'intérêt pour de nombreuses applications, incluant la protection contre les débris spatiaux. La performance des lanceurs hyper-vitesse de pointe n'est pas capable de rejoindre ces vitesses. Le lanceur à implosion utilise des explosifs pour comprimer un gaz léger de façon dynamique, afin d'atteindre des pressions et des températures beaucoup plus élevés que des lanceurs hyper-vitesse typiques. Pour cette raison, le lanceur à implosion à le potentiel de surpasser la performance de tout autre lanceur. Ce travail mettra l'accent sur l'établissement d'une compréhension des paramètres de conception critiques du lanceur à implosion dans le but d'améliorer la performance du lanceur. A cet effet, un code capable de simuler la balistique interne du lanceur a été développé. La pression et la température élevées dans le gaz causent plusieurs pertes durant le cycle de lancement, y compris l'expansion des parois du lanceur, le transfert de chaleur par convection, et les fuites de gaz. Ces pertes ont un effet important sur la performance du lanceur. Les modèles utilisés pour simuler ces pertes sont aussi présentés. Le code complet sera utilisé en conjonction avec la théorie classique de la balistique interne ainsi que des résultats expérimentaux afin d'amélioré le lanceur. Cette analyse a conduit à l'élaboration d'un lanceur à implosion capable d'accéléré un projectile de 0,1 g à 9,1 km/s.

TABLE OF CONTENTS

ACKNOWLEDGEMENTS ii

ABSTRACT iii

ABRÉGÉ iv

LIST OF TABLES viii

LIST OF FIGURES ix

1 Introduction 1

1.1 Requirements for Simulating Orbital Debris Impacts 1
1.2 Limitations of Current Technologies 5
1.2.1 Two-Stage Light Gas Guns 6
1.2.2 Railguns 10
1.2.3 Inhibited Shaped Charge 11
1.2.4 Titov Launcher 14
1.3 Implosion-Driven Launcher 15
1.3.1 Linear Explosive Driver 18
1.3.2 Single Stage Implosion Driven Launcher 26
1.3.3 Auxiliary Pump Cycle 32
1.4 Scope of Study 35

2 Development of a Quasi 1-D Lagrangian Gasdynamics Internal Ballistics Model 36

2.1 Introduction to the von Neumann Richtmyer Scheme 38
2.2 Finite Difference Equations for the von Neumann Richtmyer Scheme 40
2.3 Validation of the Numerical Scheme 46
2.3.1 Gasdynamics Validation Tests 46
2.3.2 Launcher Validation Tests 52

3 Modeling of Non-Ideal Effect in an Implosion-Driven Launcher 60

3.1 Reservoir Expansion 62
3.1.1 Modeling Approach 63
3.1.2 One-Dimensional Radial Hydrocode 64

3.1.2.1 Cylindrical Geometry . . . 65
3.1.2.2 Equation of State . . . 65
3.1.2.3 Material Strength Effects . . . 70
3.1.2.4 Launcher Simulations with Reservoir Expansion . . . 76
3.2 Non-Ideal Driver Effects . . . 76
3.3 Loss of Driver Gas through Sealing Cone . . . 87
3.4 Propellant Equation of State . . . 90
3.5 Gas Friction and Heat Transfer Effects . . . 96
3.6 Experimental Validation . . . 102

4 Internal Ballistics Considerations of an Ideal Implosion Driven Launcher 106

4.1 Introduction to the Internal Ballistics Design Parameters . . . 106
4.2 Analytical Launcher Analysis . . . 109
4.2.1 Unsteady Expansion Process . . . 110
4.2.2 Propellant Considerations . . . 111
4.2.3 Effect of Finite Driver Gas Mass in a Constant Area Launcher 117
4.2.4 Effect of Chambrage . . . 120
4.2.5 Projectile Considerations . . . 124
4.2.6 Propellant Fill Pressure . . . 127
4.2.7 Effect of Reservoir Length . . . 127
4.2.8 Further Compression of the Driver Gas . . . 129

5 Parametric Study of Single-Stage Implosion-Driven Launcher . . . 132

5.1 Implosion-Driven Launcher Scalability . . . 133
5.2 Projectile Considerations . . . 140
5.3 Driver Gas Considerations . . . 148
5.4 Explosively Driven Piston Velocity . . . 153
5.5 Driver Geometry . . . 158
5.6 Reservoir Geometry . . . 162
5.6.1 Shape of Area Change Section . . . 162
5.6.2 Projectile Offset from Area Change Section . . . 164
5.6.3 Reservoir Length . . . 165
5.7 Launcher Mechanical Design . . . 171
5.8 Summary of Single-Stage Launcher Parametric Study . . . 173
5.9 Recommended Experiments . . . 174

6 Velocity Augmentation Techniques . . . 176

6.1 Auxiliary Pump Cycle . . . 176
6.1.1 Stress Wave Timing . . . 176
6.1.2 Auxiliary Pump Experiments . . . 182
6.1.3 Future Work . . . 185

6.2 Accelerating Driver Piston 185

7 Conclusion 188

Appendix A – Nomenclature 190

Appendix B – Self-Sealing Projectile Design 192

Appendix C – Radial Hydrocode Finite Difference Equations 195

Appendix D – Phase Velocity 199

References 201

LIST OF TABLES

Table page

1–1 Recommended design parameters for a linear explosive driver [38, 5] . 26

1–2 Physics International single stage implosion driven launcher experiments [38, 5] . . . 28

1–3 Physics International experimental results for auxiliary pump launcher experiments [38] . . . 34

3–1 Comparison of simulation velocity predictions to experimental results . 103

4–1 Summary of the major design parameters of the implosion driven launcher . . . 107

5–1 Summary of experiments in which launchers of similar design were fired with large differences in initial fill pressure. . . . 145

5–2 Summary of experiments in which launchers of similar design were fired with low thickness projectiles, resulting in sporadic velocity results . . . 147

5–3 Summary of implosion launcher experiments comparing the performance of helium and hydrogen as driver gases . . . 153

5–4 Summary of experiments in which the shape of the area change section was varied . . . 164

5–5 Summary of experiments in which the offset between the end of the explosively driven piston and the beginning of the area change section was varied . . . 168

6–1 Summary of two launcher experiments comparing the performance of an implosion-driven launcher with and without an auxiliary pump cycle . . . 183

LIST OF FIGURES

Figure page

1–1 Growth of orbital debris population in recent decades (taken from NASA Orbital Debris Quarterly News [3]) 2

1–2 Cross sectional view of a typical projectile-sabot assembly travelling down a launch tube 4

1–3 Overview of hypervelocity launching capabilities 5

1–4 Overview of launcher technologies reviewed in this work 7

1–5 Operation of a two-stage light gas gun 9

1–6 Operation of a shaped charge 12

1–7 Operation of an inhibited shaped charge 13

1–8 Operation of the Titov gascumulative launcher 14

1–9 Schematic of the launch cycle of the implosion-driven launcher 17

1–10 Ideal operation of the linear explosive driver 19

1–11 Non-ideal operation of the linear explosive driver 21

1–12 Typical decay of the projectile driving pressure as of function of velocity in an implosion-driven launcher 27

1–13 Drawing of a typical implosion driven launcher and self sealing projectile 30

1–14 Operation of an implosion-driven launcher with an auxiliary pump cycle 33

2–1 Diagram of the von Neumann Richtmyer numerical scheme for a two cell system 42

2–2 Schematic of CFL condition in a Lagrangian frame of reference 45

2–3 Wave diagram for the shock tube validation problem 47

2–4 Comparison of velocity, density, and pressure profiles between the Lagrangian solver and an analytical Riemann solver for the shock tube validation case 48

2–5 Sensitivity of the L^2 norm error to the number of cells used in the simulation 49

2–6 Wave diagram of the strong shock validation problem 50

2–7 Comparison of velocity, density, and pressure profiles between the Lagrangian solver and an analytical Riemann solver for the strong shock validation case 50

2–8 Comparison of velocity, density, and pressure profiles between the Lagrangian solver and the analytical solution for the planar piston problem 51

2–9 Schematic of the leaky piston validation problem 52

2–10 Comparison of the velocity profile between the Lagrangian solver and the analytical solution to the leaky piston problem 53

2–11 $x - t$ wave diagram showing the interaction of expansion waves with the projectile in a constant area PPIG 54

2–12 Comparison of the Lagrangian solver to the analytical solution for an infinite chamber PPIG 55

2–13 Comparison of the Lagrangian solver to published computational solutions for a constant area PPIG 56

2–14 Comparison of the Lagrangian solver to published computational solutions for a chambered PPIG 57

2–15 Comparison of the Lagrangian solver to an Eulerian gasdynamics solver for a complete implosion-driven launcher simulation 57

2–16 Convergence study performed on a typical implosion-driven launcher simulation 58

2–17 Convergence study performed on a typical implosion-driven launcher simulation 59

3–1 Comparison of the predicted velocity for an ideal implosion launcher simulation and the corresponding experimental result. The launcher dimensions are: $D_{LT} = 5$ mm, $D_D = \sqrt{5}D_{LT}$, $L_D = 37D_D$, $U_D = 7$ km/s, Gas = 4MPa He, $L_R = 0.10L_D$, $L_{\text{offset}} = 3D_{LT}$, Proj = $0.5(L/D)$ ZK60 . . . 61

3–2 Schematic of the approach used to simulate the expansion of the launcher walls in the internal ballistics solver . . . 64

3–3 Graphical representation of the surface corresponding to the equation of state of a material (pressure-specific volume-internal energy relation). This surface must be obtained using the Hugoniot line generated from shock compression experiments . . . 67

3–4 Comparison of the projectile velocity profile for a launcher simulation with reservoir expansion to an ideal simulation. The launcher dimensions are: $D_{LT} = 5$ mm, $D_D = \sqrt{5}D_{LT}$, $L_D = 37D_D$, $U_D = 7$ km/s, Gas = 4MPa He, $L_R = 0.10L_D$, $L_{\text{offset}} = 3D_{LT}$, Proj = $0.5(L/D)$ ZK60 . . . 77

3–5 Comparison of the projectile driving pressure variation for a launcher simulation with reservoir expansion to an ideal simulation. The launcher dimensions are: $D_{LT} = 5$ mm, $D_D = \sqrt{5}D_{LT}$, $L_D = 37D_D$, $U_D = 7$ km/s, Gas = 4MPa He, $L_R = 0.10L_D$, $L_{\text{offset}} = 3D_{LT}$, Proj = $0.5(L/D)$ ZK60 . . . 77

3–6 Schematic demonstrating the predicted reservoir radial expansion in a typical implosion launcher at the time when the projectile has reached 2, 4, and 6 km/s. The original reservoir profile is shown in the dashed line. A 5:1 scaling has been used to emphasize the radial dimension. . . . 78

3–7 Schematic of the X-t diagram of a non-ideal driver. The effect of the communication time between the piston and the shock wave on the analysis is shown. . . . 82

3–8 Linear curve fit of precursor shock wave velocity as a function of explosively driven piston position used for the non-ideal driver model. The data was obtained from a 1.27 cm diameter driver filled with 2 MPa of helium. . . . 84

3–9 Standoff between the precursor shock wave and the explosively driven piston as a function of piston position for the non-ideal driver model and the experimental data used to generate the model . . . 85

3–10 Precursor shock wave velocity as a function of piston position for the non-ideal driver model and the experimental data used to generate the model . . . 85

3–11 Comparison between the projectile velocity profile predicted by simulations using ideal and non-ideal drivers. The simulations include the reservoir expansion model. The launcher dimensions are: $D_{LT} = 5$ mm, $D_D = \sqrt{5}D_{LT}$, $U_D = 7$ km/s, Gas = 4MPa He, $L_R = 0.18L_D$, $L_{\text{offset}} = 3D_{LT}$, Proj = $0.5(L/D)$ ZK60 . . . 86

3–12 Picture of the cross section of an implosion-driven launcher reservoir after being fired. The sealing cone section was not able to completely seal the driver gas. . . . 88

3–13 Comparison of the projectile velocity profile for different reservoir openings. The simulations include the reservoir expansion model and non-ideal driver effects. The launcher dimensions are: $D_{LT} = 5$ mm, $D_D = \sqrt{5}D_{LT}$, $L_D = 20D_D$, $U_D = 7$ km/s, Gas = 4MPa He, $L_R = 0.18L_D$, $L_{\text{offset}} = 3D_{LT}$, Proj = $0.5(L/D)$ ZK60 . . . 89

3–14 Velocity deficit from cone leaking as a function of driver length and projectile thickness. The reservoir opening is set equal to the driver diameter, simulating a full opening. The simulations include the reservoir expansion model and non-ideal driver effects. The launcher dimensions are: $D_{LT} = 5$ mm, $D_D = \sqrt{5}D_{LT}$, $U_D = 7$ km/s, Gas = 4MPa He, $L_R = 0.18L_D$, $L_{\text{offset}} = 3D_{LT}$, Proj = $0.5(L/D)$ ZK60 . . . 90

3–15 Schematic of the modified SESAME matrix for pressure as a function of internal energy and density . . . 92

3–16 Comparison of the projectile velocity profile for real gas and ideal gas simulations of helium and hydrogen launchers. The simulations include the reservoir expansion model. The launcher dimensions are: $D_{LT} = 5$ mm, $D_D = \sqrt{5}D_{LT}$, $L_D = 37D_D$, $U_D = 7$ km/s, (Gas = 4MPa He, $L_R = 0.18L_D$) or (Gas = 5.8MPa H_2, $L_R = 0.12L_D$), $L_{\text{offset}} = 3D_{LT}$, Proj = $0.5(L/D)$ ZK60 . . . 93

3–17 Comparison of the projectile driving pressure as a function of velocity for real gas and ideal gas simulations of helium and hydrogen launchers. The simulations include the reservoir expansion model. The launcher dimensions are: $D_{LT} = 5$ mm, $D_D = \sqrt{5}D_{LT}$, $L_D = 37D_D$, $U_D = 7$ km/s, (Gas = 4MPa He, $L_R = 0.18L_D$) or (Gas = 5.8 MPa H_2, $L_R = 0.12L_D$), $L_{\text{offset}} = 3D_{LT}$, Proj = 0.5($L/D$) ZK60 94

3–18 Comparison of the temperature of the driver gas directly behind the projectile as a function of velocity for real gas and ideal gas simulations of helium and hydrogen launchers. The simulations include the reservoir expansion model. The launcher dimensions are: $D_{LT} = 5$ mm, $D_D = \sqrt{5}D_{LT}$, $L_D = 37D_D$, $U_D = 7$ km/s, (Gas = 4MPa He, $L_R = 0.18L_D$) or (Gas = 5.8 MPa H_2, $L_R = 0.12L_D$), $L_{\text{offset}} = 3D_{LT}$, Proj = 0.5($L/D$) ZK60 94

3–19 Comparison of the specific internal energy of the driver gas directly behind the projectile as a function of velocity for real gas and ideal gas simulations of helium and hydrogen launchers. The simulations include the reservoir expansion model. The launcher dimensions are: $D_{LT} = 5$ mm, $D_D = \sqrt{5}D_{LT}$, $L_D = 37D_D$, $U_D = 7$ km/s, (Gas = 4MPa He, $L_R = 0.18L_D$) or (Gas = 5.8 MPa H_2, $L_R = 0.12L_D$), $L_{\text{offset}} = 3D_{LT}$, Proj = 0.5($L/D$) ZK60 95

3–20 Comparison of the velocity profile for a launcher with and without heat transfer and gas friction losses. The simulations include the reservoir expansion model. The launcher dimensions are: $D_{LT} = 5$ mm, $D_D = \sqrt{5}D_{LT}$, $L_D = 37D_D$, $U_D = 7$ km/s, Gas = 4MPa He, $L_R = 0.18L_D$, $L_{\text{offset}} = 3D_{LT}$, Proj = 0.5($L/D$) 100

3–21 Effect of the three major losses on the velocity profile of the implosion launcher. The launcher dimensions are: $D_{LT} = 5$ mm, $D_D = \sqrt{5}D_{LT}$, $L_D = 37D_D$, $U_D = 7$ km/s, Gas = 4MPa He, $L_R = 0.10L_D$, $L_{\text{offset}} = 3D_{LT}$, Proj = 0.5($L/D$) 102

3–22 Detailed schematic of the sealing cone demonstrating the difficulty in determining the location where the explosively driven piston comes to a stop 105

4–1 Schematic of the implosion launcher showing the design parameters that will be considered in internal ballistics analysis 107

4–2 Comparison of the projectile driving pressure decay as a function of velocity for an ideal implosion launcher simulation and a PPIG simulation . . . 110

4–3 Schematic of the unsteady expansion process and the resulting gas velocity, pressure, and temperature profiles . . . 111

4–4 Graph showing the effect of the initial speed of sound of a gas on the change in pressure as a function of change in velocity for an unsteady expansion . . . 114

4–5 Graph showing the effect of the specific heat ratio (γ) of a gas on the change in pressure as a function of change in velocity for an unsteady expansion . . . 115

4–6 Comparison of the increase in speed of sound as a function of pressure ratio for an isentropic compression and a shock compression . . . 116

4–7 Comparison speed of sound divided by the specific heat ratio as a function of piston velocity for a reflected shock compression in helium and hydrogen. This provides an empirical comparative measure of the two gases as propellants in the implosion launcher. . 117

4–8 Non-dimensional projectile velocity as a function of its position in the launch tube showing the effect of driver gas mass to projectile mass on the performance of a PPIG . . . 118

4–9 Comparison of non-dimensional projectile velocity as a function of its position in the launch tube for helium and hydrogen PPIGs with finite driver gas mass . . . 120

4–10 Schematic of the wave dynamics in a chambered PPIG launcher . . . 122

4–11 Non-dimensional projectile velocity as a function of its position in the launch tube showing the effect of chambrage on the performance of a PPIG . . . 123

4–12 Schematic of the reflected shock wave criteria used to determine the length of the reservoir in an implosion launcher . . . 128

5–1 Comparison of the projectile velocity as a function of position for 5 and 25 mm for ideal implosion-driven launcher simulations . . . 136

5–2 Comparison of the projectile velocity as a function of position for 5 and 25 mm for implosion-driven launcher simulations with the reservoir expansion model . . . 138

5–3 Comparison of the projectile velocity as a function of position for 5 and 25 mm for implosion-driven launcher simulations with reservoir expansion, gas friction, and heat transfer 140

5–4 Effect of the effective density of a projectile on launcher efficiency. Lines indicating the corresponding effective density of 0.5 caliber magnesium, aluminum, and titanium projectiles have been included for reference. 142

5–5 Effect of the maximum projectile driving pressure of a projectile on launcher efficiency 144

5–6 Comparison of the projectile velocity profile for a helium and hydrogen launcher. The simulations include the reservoir expansion model, gas friction/heat transfer losses, and the SESAME equation of state model. The launcher dimensions are: $D_{LT} = 10$ mm, $D_D = \sqrt{5}D_{LT}$, $L_D = 30D_D$, $U_D = 7$ km/s, (Gas = 4MPa He, $L_R = 0.18L_D$) or (Gas = 5.4MPa H_2, $L_R = 0.12L_D$), $L_{\text{offset}} = 3D_{LT}$, Proj = $0.5(L/D)$ 149

5–7 Comparison of the projectile base pressure decay as a function of velocity for a helium and hydrogen launcher. The simulations include the reservoir expansion model, gas friction/heat transfer losses, and the SESAME equation of state model. The launcher dimensions are: $D_{LT} = 10$ mm, $D_D = \sqrt{5}D_{LT}$, $L_D = 30D_D$, $U_D = 7$ km/s, (Gas = 4MPa He, $L_R = 0.18L_D$) or (Gas = 5.4MPa H_2, $L_R = 0.12L_D$), $L_{\text{offset}} = 3D_{LT}$, Proj = $0.5(L/D)$ 150

5–8 Comparison of the projectile base pressure decay as a function of velocity for a hydrogen launcher with a SESAME equation of state and an ideal gas equation of state. The simulations include the reservoir expansion model and gas friction/heat transfer losses. The launcher dimensions are: $D_{LT} = 10$ mm, $D_D = \sqrt{5}D_{LT}$, $L_D = 30D_D$, $U_D = 7$ km/s, Gas = 5.4MPa H_2, $L_R = 0.12L_D$, $L_{\text{offset}} = 3D_{LT}$, Proj = $0.5(L/D)$ 151

5–9 Comparison of the projectile velocity profile for a helium and hydrogen launcher having the same G/M. The simulations include the reservoir expansion model, gas friction/heat transfer losses, and the SESAME equation of state model. The launcher dimensions are: $D_{LT} = 10$ mm, $D_D = \sqrt{5}D_{LT}$, $U_D = 7$ km/s, (Gas = 4MPa He, $L_R = 0.18L_D$, $L_D = 30D_D$) or (Gas = 5.4MPa H_2, $L_R = 0.12L_D$, $L_D = 44.4D_D$), $L_{\text{offset}} = 3D_{LT}$, Proj = $0.5(L/D)$ 152

5–10 Predicted projectile velocity as a function of explosively driven piston velocity. Launchers having two different driver lengths are compared. The simulations include the reservoir expansion model, gas friction/heat transfer losses, and the non-ideal pump tube model. The launcher dimensions are: $D_{LT} = 10$ mm, $D_D = \sqrt{5}D_{LT}$, Gas=He, $L_R = 0.2L_D$, $L_{\text{offset}} = 3D_{LT}$, Proj $= 0.5(L/D)$ 155

5–11 Comparison of the projectile driving pressure decay in launchers having different explosively driven piston velocities. The simulations include the reservoir expansion model, gas friction/heat transfer losses, and the non-ideal pump tube model. The launcher dimensions are: $D_{LT} = 10$ mm, $D_D = \sqrt{5}D_{LT}$, $L_D = 60D_D$, Gas=He, $L_R = 0.2L_D$, $L_{\text{offset}} = 3D_{LT}$, Proj $= 0.5(L/D)$ 156

5–12 Comparison of the precursor shock wave velocity and standoff between the precursor shock wave and the explosively driven piston for phased and non-phased drivers 158

5–13 Variation in the gas mass to projectile mass ratio of an implosion launcher as a function of the area ratio and length of the driver . . 160

5–14 Variation in the predicted projectile velocity of an implosion launcher as a function of the area ratio and length of the driver. The simulations include the reservoir expansion model, gas friction/heat transfer losses, and the non-ideal pump tube model. The launcher dimensions are: $D_{LT} = 10$ mm, $D_D = \sqrt{5}D_{LT}$, $L_D = 40D_D$, $U_D = 7$ km/s, Gas = 4MPa He, $L_R = 0.2L_D$, $L_{\text{offset}} = 3D_{LT}$, Proj $= 0.5(L/D)$161

5–15 Schematic of the definition of reservoir length in an implosion-driven launcher. 162

5–16 Variation in the predicted projectile velocity of an implosion launcher as a function of the offset between the area change section and the projectile. The simulations include the reservoir expansion model, gas friction/heat transfer losses, and the non-ideal pump tube model. The launcher dimensions are: $D_{LT} = 10$ mm, $D_D = \sqrt{5}D_{LT}$, $L_D = 40D_D$, $U_D = 7$ km/s, Gas = 4MPa He, $L_R = 0.2L_D$, Proj $= 0.5(L/D)$ 166

5–17 Comparison of the evolution of the projectile driving pressure in implosion launchers having significantly different reservoir lengths. The simulations include the reservoir expansion model, gas friction/heat transfer losses, and the non-ideal pump tube model. The launcher dimensions are: $D_{LT} = 10$ mm, $D_D = \sqrt{5}D_{LT}$, $L_D = 40D_D$, $U_D = 7$ km/s, Gas = 4MPa He, $L_{\text{offset}} = 3D_{LT}$, Proj = $0.5(L/D)$ 167

5–18 Variation in the predicted projectile velocity of an implosion launcher as a function of the reservoir length. The effect of the reservoir length on the maximum pressure against the explosively driven piston is also shown. The simulations include the reservoir expansion model, gas friction/heat transfer losses, and the non-ideal pump tube model. The launcher dimensions are: $D_{LT} = 10$ mm, $D_D = \sqrt{5}D_{LT}$, $L_D = 40D_D$, $U_D = 7$ km/s, Gas = 4MPa He, $L_{\text{offset}} = 3D_{LT}$, Proj = $0.5(L/D)$ 169

5–19 Summary of mechanical design recommendations for a typical single stage implosion driven launcher 172

6–1 Schematic of the dragged (phased) shock wave that results when a detonation wave travels over the reservoir at a velocity which is greater than the shock wave velocity. The resulting shock wave velocity along the projectile plane is equal to the detonation velocity. 178

6–2 Schematic of the phase velocity effect that results from initiating the auxiliary pump above the reservoir surface. The arrival velocity of the detonation wave along the reservoir surface will be higher than the detonation velocity. 180

6–3 Graph showing the effect of the auxiliary pump initiation height on the arrival velocity of the detonation wave along the reservoir surface. The position and velocity axis have been non-dimensionalized by the projectile diameter and the detonation velocity respectively. . . 181

6–4 Position-time diagram showing the profile of the projectile (obtained from simulations) and the arrival of the stress wave along the projectile plane. These diagrams are used to determine the optimal timing for the initiation of the auxiliary pump cycle. 181

6–5 Cross sectional view of the arrangement of the auxiliary pump experiment. A picture of the reservoir explosive arrangement is also shown. 184

6–6 Comparison of the predicted evolution of the projectile driving pressure in an accelerating driver piston launcher and a conventional implosion-driven launcher. The simulations include reservoir expansion and heat transfer and gas friction losses. 186

7–1 Detailed drawing of a self sealing projectile cross-section showing the main features of the design 193

7–2 Vector diagram showing the phase velocity as a function of wave velocity and phase angle 200

7–3 Schematic of a two component explosive lens 200

CHAPTER 1
Introduction

Launching large size projectiles (greater than 1 g) to the hypervelocity impact regime (typically defined as the velocity where the pressures generated during an impact are greater than the strength of the materials involved) is of interest for a number of scientific fields including orbital debris impact simulation, material characterization, geophysics of planetary impacts, and fundamental equation of state studies. Given that typical solid propellant (gunpowder) guns are limited to 2.5 km/s, accelerating projectiles to the velocities of interest (>6 km/s) requires devices known as hypervelocity launchers. While a number of different hypervelocity launching techniques have been devised, only a few have proven to be successful and none have been able to reach velocities well above 10 km/s with projectiles fit for orbital debris impact testing. This work will focus on the development of an implosion-driven launcher, based on a concept originally proposed by the Physics International Company in the 1960's [16]. As will be seen, this concept shows significant promise for being able to launch large size projectiles to velocities above 10 km/s.

1.1 Requirements for Simulating Orbital Debris Impacts

The international space community has identified orbital debris (term used for all non-functional human-made objects or fragments in earth orbit), as an important threat to all spacefaring objects in earth orbit [1]. The consequences of orbital debris impacts are potentially devastating due to the presence of humans in space, as well as the reliance on satellites in a number of sectors including telecommunications, scientific research, and defence. Spacecraft in low earth orbit (LEO), the region

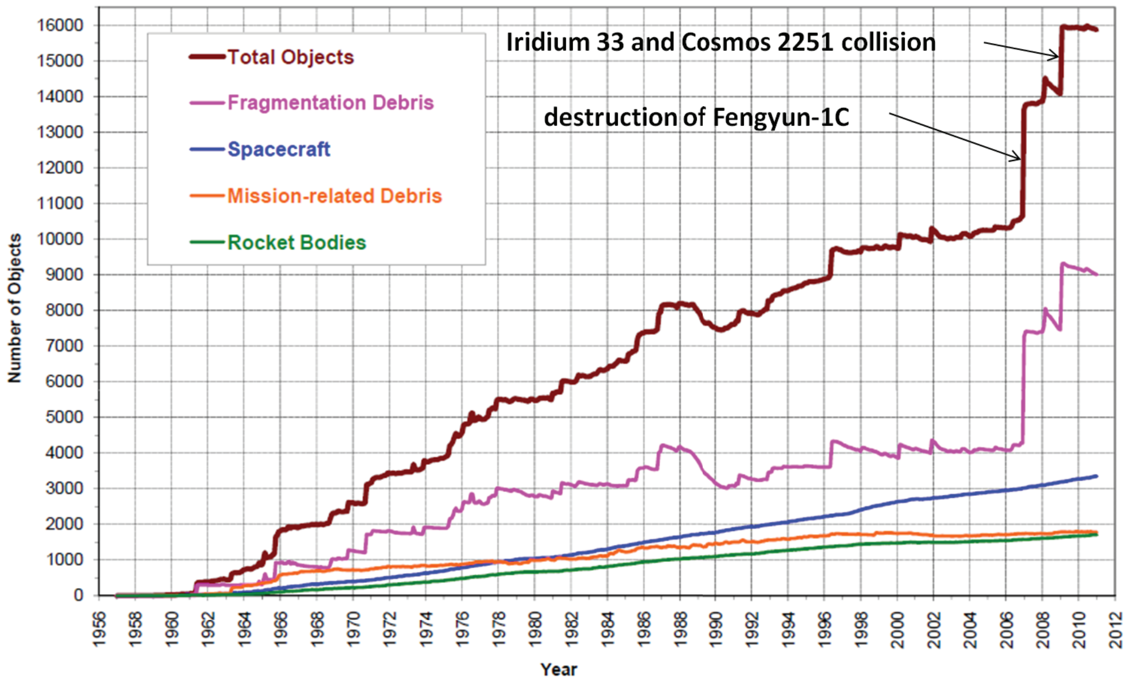

Figure 1–1: Growth of orbital debris population in recent decades (taken from NASA Orbital Debris Quarterly News [3])

that sees the highest amount of space traffic (including the majority of satellites and the International Space Station), are most at risk due to the relatively high concentration of debris in this region. It is believed that the population of debris may have already reached a point where the generation of new debris from collisions may cause an irreversible runaway effect in the debris population, a scenario known as the Kessler syndrome [22]. Figure 1–1 shows the alarming increase in the orbital debris population in recent decades. It should be noted that a large portion of the debris generated in recent years has come from two collision events: the intentional destruction of the Fenyun 1-C satellite, and the collision between the functional Iridium 33 satellite and defunct Kosmos 2251 satellite. This reinforces how quickly impact debris can be generated.

Objects in LEO typically have orbital velocities of 7 km/s, leading to relative collision velocities of 10 km/s on average, with collisions above 15 km/s being possible. [2] Large debris (larger than 10 cm) can be tracked and avoided, but smaller bodies in the 0.1 to 10-cm range are not tracked and pose a significant and unpredictable threat to spacecraft. Although small, these impactors carry an enormous amount of kinetic energy, and are capable of severely damaging spacecraft structures upon impact. For these reasons, the development of shielding for critical or vulnerable spacecraft components and manned spacecraft has become a priority for international space agencies.

Full scale laboratory testing is ultimately required, in order to fully assess the threat of orbital debris on spacecraft and design efficient (low weight and low volume) and effective shielding. The extreme physics of impacts in the hypervelocity regime leads to large uncertainties in the constitutive material models (strength models), as well as equation of state models, that are typically developed for much lower impact velocities. This means that computational approaches to hypervelocity impact modeling require extensive experimental calibration from laboratory generated impacts at the velocity of interest. Computational modeling efforts will need to be supported by physical testing.

Orbital debris impact testing is typically done with a 0.1 to 5-g aluminum sphere [14] which is fired from a launcher using a bore-sized cylindrical sabot that carries the sphere (see Figure 1–2). The need to launch a thick sabot (typically >0.5 launch tube diameters in order to be stable) and an aluminum sphere, means that the aerial density (g/cm^2) or resistance to acceleration of the projectile package is quite large. In order to ensure the tests are repeatable and representative of orbital debris impacts the maximum driving pressure which accelerates the projectile must

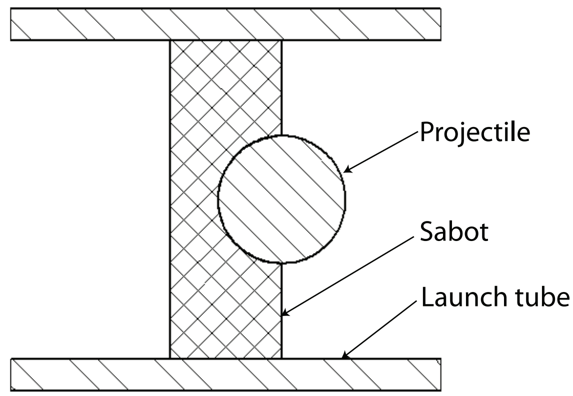

Figure 1–2: Cross sectional view of a typical projectile-sabot assembly travelling down a launch tube

be kept sufficiently low as to avoid erosion, hydrodynamic deformation, or melting of the projectile. This criterion, often referred to as soft launch, requires that the driving pressure be kept bellow approximately 5 GPa. Therefore, performing orbital debris impact testing requires a launcher that has the ability to apply modest driving pressures over relatively long timescales to gently accelerate the projectile to the velocities of interest.

Current state of the art orbital debris impact testing is performed with two-stage light gas guns (2SLGG). The 2SLGG is ideal for orbital debris impact testing because of its ability to soft launch high aerial density packages to high velocities. Although this technology has been instrumental in the development of orbital debris impact research, its performance reached a plateau of 8 km/s in the 1960's [32]. Despite decades of extensive development, the 2SLGG has been unable to reach typical orbital debris impact velocities.

In order to fully reproduce the threat of orbital debris impacts, a technology with the ability to launch intact projectiles with well characterized mass and orientation, at velocities above 10 km/s, needs to be developed. Figure 1–3 shows a mass-velocity map of current hypervelocity launcher technologies. As is indicated in the figure, the

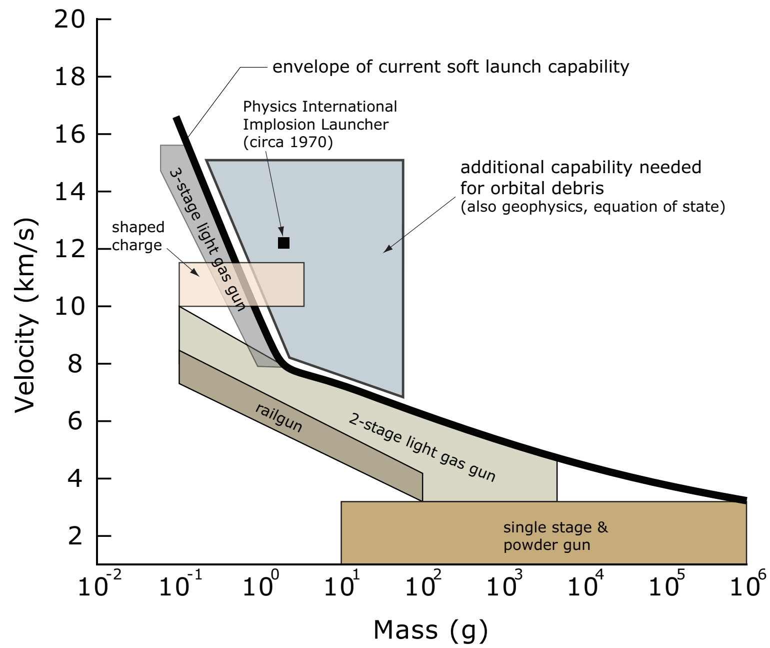

Figure 1–3: Overview of hypervelocity launching capabilities

capacity to launch well characterized projectiles with a 1 to 10-g mass (equivalent to $\approx$ 1 cm in size) to velocities above 10 km/s does not currently exist.

1.2 Limitations of Current Technologies

The challenge of launching large size projectiles at velocities above 10 km/s with modest driving pressures has proven difficult to overcome. A number of technologies have been developed to launch thin plates or very small particles at very high velocities (up to 40 km/s), often to perform equation of state testing: graded density flyers/pushers, multistage explosive cascades, fast shock tube, electromagnetic launchers, and laser-driven launchers. Although many of these technologies have played an important role in high pressure equation of state testing, they will not be discussed further for three main reasons:

1. The launch of very thin flyer plates cannot be extended to launching high aerial density projectile packages for full scale orbital debris impact testing.

2. The flyer plate driving pressures tend to be on the order of 50 to 100 GPa. Although the loading can be applied in such a way as to avoid melting, the non-ideal effects involved in accelerating flyers with such high pressures create significant scatter in the resulting data. The capacity to reach these velocities with a soft launch technique could resolve a number of uncertainties in the data.

3. The graded density flyer/pusher technique, often referred to as an impact driven three-stage light-gas gun, relies on a launcher (typically a 2SLGG) to fire a large relatively heavy projectile into a series of flyer plates of decreasing thickness and density, eventually launching a thin flyer plate to very high velocities (>15 km/s) [13]. This technique is not seen as a competing technology, but rather a velocity augmentation technique that could be applied to any launcher and could benefit from improved launcher mass-velocity capabilities.

This section will give a brief description of the most successful hypervelocity launcher technologies, as well as some insight to their limitations. The focus will be on technologies capable of launching large scale (>1 g) and high aspect ratio projectiles to hypervelocity (technologies that could be used for orbital debris impact testing). Figure 1–4 summarizes the capabilities of the launcher technologies which will be discussed in depth in this section.

1.2.1 Two-Stage Light Gas Guns

2SLGG are used extensively for orbital debris impact testing and equation of state research. Their prominence can be attributed to their ability to launch well characterized projectiles with a controlled orientation and at highly repeatable velocities. Although they require significant maintenance between shots, 2SLGG are completely reusable, allowing them to perform multiple tests per day.

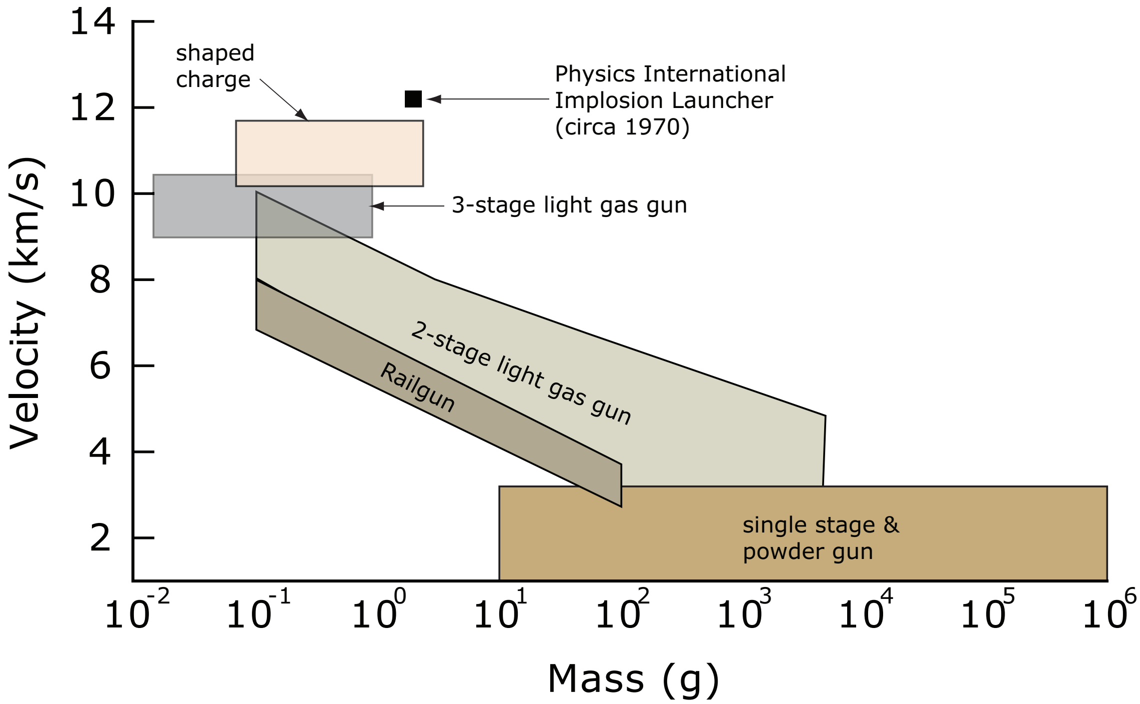

Figure 1–4: Overview of launcher technologies reviewed in this work

The launch cycle of a 2SLGG is illustrated in Figure 1–5. 2SLGG use a compressed gas or propellant charge to drive a large heavy piston, which in turn compresses a light driver gas (hydrogen or helium). The diaphragm, which initially separates the projectile from the pressurized driver gas, bursts under the increasingly high driver gas pressure, allowing the gas to propel the projectile [9]. The piston compresses the light driver gas quasi-adiabatically, allowing it to reach a very high pressure and temperature. Light gas guns replace the high molecular weight driver gas of a typical solid propellant gun with a low molecular weight gas, which greatly increases the theoretical limit of projectile velocity. This scheme has allowed the 2SLGG to hold the velocity record for projectiles in the 0.1 g to 1 kg range.

The projectile velocity can be tuned by varying the size of the nitrocellulose charge, the mass of the piston, the initial pressure of the light gas, the length of the driver gas section (pump tube), the diaphragm burst pressure, the projectile mass, and the area ratio between the pump tube and the launch tube. Because the projectile begins to accelerate before the piston has completed its compression stroke, 2SLGG can be designed to maintain a high base pressure on the projectile by gradually increasing the reservoir pressure during the early stage of the launch cycle. However, the piston eventually reaches the area change section, bringing it to a stop and allowing the driver gas to expand ahead of the stopped piston.

In order to improve performance, the launcher must be designed to provide either a longer impulse or a more intense impulse. The eventual expansion of the driver gas can be delayed by using a longer pump tube (known as increasing the compression ratio), which increases the length and intensity of the compression stroke. This tends to significantly increase the temperature and pressure of the driver gas at the end of the compression stroke, which is beneficial for performance but can lead to severe ablation and expansion damage to the launcher. Indeed, it can be shown analytically that maintaining a constant base pressure on the projectile would require an exponential increase in the reservoir pressure, which cannot be accomplished in a practical launcher [31]. Given that the length of the compression stroke will be limited, one can also increase the intensity of projectile loading, which is typically done by reducing the initial fill pressure of the light gas. Although this technique can readily increase the velocity capability of a launcher, it also significantly increases the maximum pressure in the reservoir. A number of techniques have attempted to increase the performance of the launcher by increasing the speed of sound of the propellant, which should in turn allow the base pressure behind the projectile to decay more slowly. Real gas considerations and losses (heat transfer and friction) have

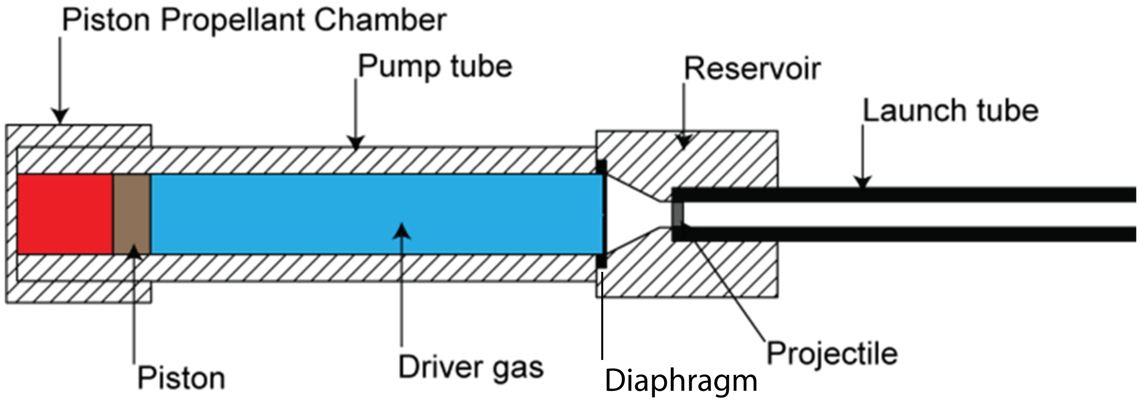

Figure 1–5: Operation of a two-stage light gas gun

prevented these techniques from offering significant improvements to the standard 2SLGG scheme [12].

The limitations of 2SLGG technology can be attributed to two main factors. First, in order to keep maintenance costs reasonable, the maximum launch cycle pressure and temperature must be kept low enough as to not severely damage the launcher. This prevents 2SLGG facilities, some of which have reached velocities well above 8 km/s to consistently operate at these velocities. Given the limit on driver gas pressure and temperature, there is a limit to the length and intensity of the compression stroke of the piston. This ultimately places a limit on the maximum projectile driving pressure and the length of time over which this pressure can be maintained. Once the compression stroke is complete, the projectile driving pressure decays quickly due to the expansion of the driver gas, as well as viscous and convective heat transfer losses as the gas flows through the launch tube. Although schemes to continue to compress the driver gas by injecting propellant into the launch tube have been proposed, none have been able to demonstrate actual velocity gain. Finally, an important limitation to the capabilities of the 2SLGG is the size of the facility required to accelerate a given projectile. Although one could theoretically scale up a facility launching 10 g to 8 km/s to a facility capable of launching 1 kg to this speed, the size and cost of the launcher, which is in the hundreds of thousands of dollars, would increase approximately 100 fold.

Attempts have also been made to further increase the velocities attainable with 2SLGG by adding a third acceleration stage (i.e., three-stage light gas gun). There are two main types of three-stage light gas guns: a gasdynamic third stage and an impact-driven third stage (i.e., graded density pusher/flyer technique discussed briefly in Section 1.2). In a gasdynamic third stage, the projectile of a 2SLGG dynamically compresses a light gas ahead of it, which propels an even smaller projectile [19]. The rapid shock compression provided by the second piston allows the third stage driver gas to reach very high pressures and temperatures. This technique has the potential to reach velocities well above 10 km/s, as long as the third stage section can be made expendable. However, actual implementations of this concept have not been able to reach velocities above 11 km/s [29]. The gasdynamic three-stage light gas gun technique is currently being used by the University of Dayton Research Institute to perform orbital debris testing in the 9-10 km/s range. The main drawback of this scheme is that it launches very small projectiles given the size of the launcher. For this reason, the largest facilities have only been able to launch projectiles on the order of 0.1 g. As will be seen, a compression cycle similar to this third stage is provided by the first stage of an implosion-driven launcher, allowing for an equally effective but much more compact design.

1.2.2 Railguns

Railgun technology is typically used to launch large projectiles (>100 g) to low velocities (<5 km/s). Railguns accelerate projectiles using the magnetic field that is generated when large currents (supplied by capacitor banks) are passed through parallel conducting rails in opposite directions. The rails are joined by a conductive armature which slides along the rails, thus allowing the current to flow across the rails. The armature is propelled by the Lorentz force which is generated by the current passing through it and the magnetic field of the rails. The armature acts like a sabot in a gasdynamic launcher, allowing the railgun to launch a variety of projectile packages. For hypervelocity applications, the solid armature can be replaced by a relatively light plasma which drives a projectile in a similar way to a gasdynamic launcher. Although plasma armature railguns were once thought to offer the promise to reach velocities greater than 10 km/s, difficulties related to ablation of the rails and arcing of current across the rails have prevented them from reaching velocities significantly above 6 km/s [28]. As was seen in Figure 1–4, railguns remain slower than 2SLGG over the entire range of projectile sizes. However, railguns are still widely used because of their ability to launch large packages from relatively compact launchers. In particular, they hold promise for a number of potential military applications, notably large navy guns that could benefit from the performance increase of a railgun over conventional powder guns [18].

1.2.3 Inhibited Shaped Charge

The energy and power density of explosives (higher than any other non-nuclear source) makes them an ideal driver for hypervelocity launchers. Furthermore, explosives deliver their energy in the form of high pressure and temperature detonation products that have a very high expansion velocity. For example, flyer plates can be launched to maximum velocities on the order of 6 km/s by simply applying explosives directly to the plate [4]. More importantly, a number of techniques have

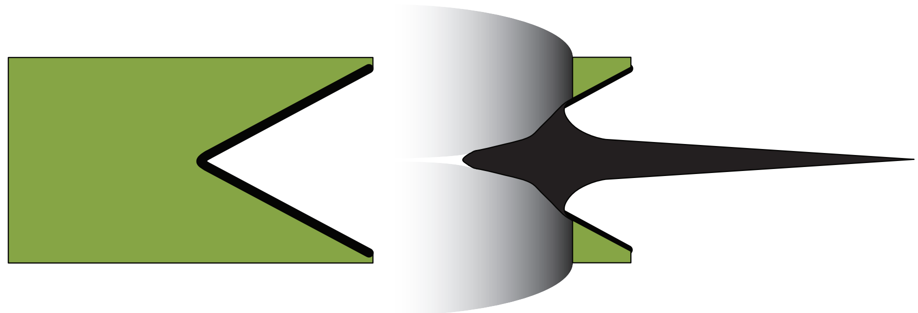

Figure 1–6: Operation of a shaped charge

been devised to cumulate or focus this explosive energy into accelerating objects to significantly higher velocities.

The most commonly used focusing scheme is the shaped charge, whose operation is shown in Figure 1–6. As can be seen, the shaped charge is composed of a hollow conical metal liner surrounded with explosives on its outside. As the explosives implode the conical cavity, their energy is focused into driving a thin hydrodynamic jet which can be made to travel significantly faster than the explosive detonation velocity (upward of 10 km/s). The penetration ability of this very fast, thin, and dense jet has found applications in many fields, including defence applications, perforation of oil wells, and demolition.

Of particular interest for orbital debris impact testing is the inhibited shaped charge concept, in which the long thin jet is interrupted to form a projectile with a much lower aspect ratio. Radiographs (X-ray pictures) are then used to estimate the mass of the projectile. This technique has successfully been used to perform orbital debris impact testing in the 10 to 11 km/s regime [37]. The inhibited shaped charge is capable of launching projectiles larger than 1 g to velocities well above the capabilities of current test facilities. Furthermore, shaped charges can be manufactured for a low cost and do not require the large infrastructure of a two-stage light gas gun. The operation of the inhibited shaped charge can be seen in Figure 1–7.

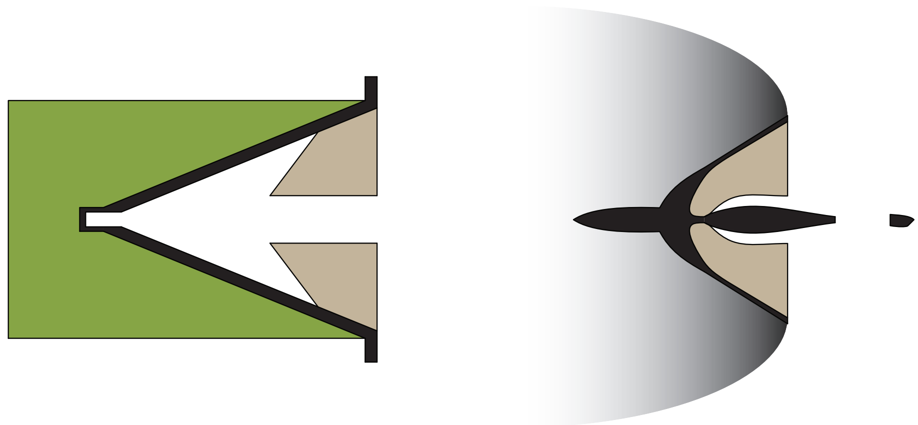

Figure 1–7: Operation of an inhibited shaped charge

The inhibited shaped charge has enabled orbital debris impact testing at mass-velocity regimes significantly above the capabilities of 2SLGG. However, it is not the ideal choice for performing orbital debris testing due to a number of limitations. First, the projectiles launched by the inhibited shaped charge technique have been hydrodynamically deformed and possibly partially melted by the direct action of the explosives. Therefore, the jet-like projectile is not representative of real orbital debris. Also, it is difficult to control the shape of the projectile. The penetration ability of the rough cylindrical projectile produced by the inhibited shaped charge may be significantly different to those used for typical orbital debris impact testing.

The shaped charge shows the potential for cumulating explosive energy to launch projectiles to hypervelocity. However, the undesired hydrodynamic deformation and heating, caused by the direct action of the explosive and intense focusing mean that shaped charges are not capable of launching intact and well characterized projectiles. However, it is possible that using a less intense focusing scheme could be used to soft-launch a projectile.

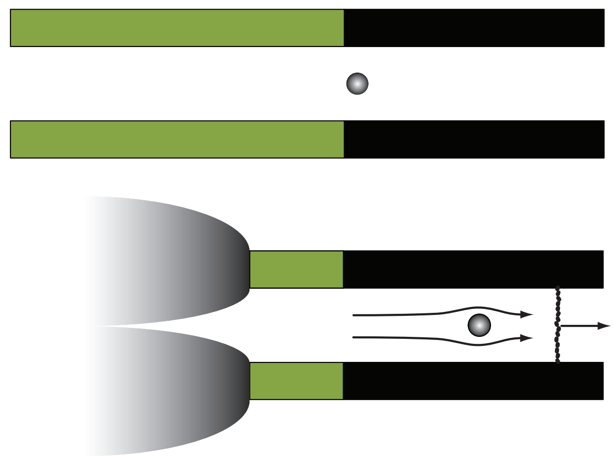

Figure 1–8: Operation of the Titov gascumulative launcher

1.2.4 Titov Launcher

The Titov launcher, pictured in Figure 1–8, is based on the gas-cumulative jet phenomenon, in which a cylindrical explosive charge with a hollow center drives a fast jet of detonation products ahead of the detonation front. The launcher consists of a hollow cylindrical explosive charge that is usually clad with metal to focus the detonation products inwards. The projectile is suspended in the explosive cavity at a given distance ahead of the point of initiation to allow the gas jet to form and grow. As the explosive is initiated and the detonation travels along the charge, the detonation products expand towards the centre of the charge. A portion of the impinging detonation products are jetted forward, forming a dense gas jet that travels ahead of the detonation wave at velocities of 10 to 15 km/s. The small spherical projectile is accelerated by the drag of the gas-cumulative jet. Velocities from 10 to 12 km/s have been demonstrated for very small projectiles (<1 mm), and 5 to 8 km/s for larger projectiles (1 to 10 mm) [17].

By using a linear focusing technique, the Titov launcher is capable of applying a long and relatively constant impulse on the projectile. Although the gas-cumulative jet is highly energetic, the loading on the projectile is gentle enough to ensure its survivability. The ability to launch small spheres to large velocities in a relatively simple and compact device has made the Titov launcher an attractive option for orbital debris impact testing.

The principle limitation of the Titov launcher hinges on the fact that it relies on drag to accelerate the projectile. As the projectile gets bigger, the proportional increase in projectile mass is much greater than its increase in drag. This means that the performance of the Titov launcher scales poorly and cannot launch projectiles much larger than 1 cm to hypervelocity. Another significant challenge in the design is launching the projectile accurately, given that it is not constrained by a launch tube and the flow field in the gas dynamic jet can be highly irregular. A final note should be made to the fact that the high energy flow over the projectile results in significant convective heat transfer which can cause severe projectile ablation. Although steel and titanium spheres have been shown to ablate very little, aluminum projectiles, which are typically desired for orbital debris testing, can be susceptible to ablation.

The explosive launchers presented above offer a number of advantages over a two-stage light-gas gun, including greater velocity capabilities, a lower cost (launcher and its facility), and a much simpler design. However, these techniques have not been able to match the ability of the two-stage light gas gun to consistently soft launch projectiles with a controlled shape and orientation. As will be seen, the implosion-driven launcher concept utilizes a linear explosive focusing scheme to compress a light driver gas, thus utilizing the benefits of explosive launchers in a robust gasdynamic launch cycle.

1.3 Implosion-Driven Launcher

The implosion-driven launcher concept, shown in Figure 1–9 is a light-gas gun in which the driver gas is explosively compressed by a device known as a linear explosive driver. The driver is composed of a layer of explosives placed around a thin-walled steel tube which has been pressurized with a light gas (helium or hydrogen). As the explosive is initiated, the detonation drives the tube walls inward and forms an explosively driven piston that travels into the gas at the speed of the detonation. This drives a strong shock wave which travels ahead of the pinch, forming an increasingly long column of compressed gas. The precursor shock wave eventually reflects off the projectile which is set in motion by the nearly instantaneous pressure rise. The reflected shock wave travels towards the back of the launcher and stagnates the gas in the reservoir, which further increases its pressure and temperature. When the detonation reaches the reservoir section, a large steel conical section is imploded in order to seal the driver gas. The projectile is propelled by the expansion of the stagnated driver gas. The high initial pressure and speed of sound of the gas allows it to maintain an elevated driving pressure on the projectile as the gas expands. By using a light gas to store the energy of the explosive and release it in a controlled manner, projectiles can be launched without the hydrodynamic deformation typically encountered in explosive launching techniques.

An explosively driven light-gas gun holds a number of advantages over a 2SLGG. First, being a single shot device, it can be allowed to generate driver gas pressures well above the strength of the launcher material and gas temperatures that would lead to unacceptable amounts of ablation in a reusable launcher. This allows the driver gas in an implosion-driven launcher to reach a much higher speed of sound and accelerate the projectile at a significantly faster rate than a 2SLGG. As a result, the propellant in an implosion-driven launcher holds a significant theoretical advantage over that of a 2SLGG [31]. Another important strength of the implosion-driven

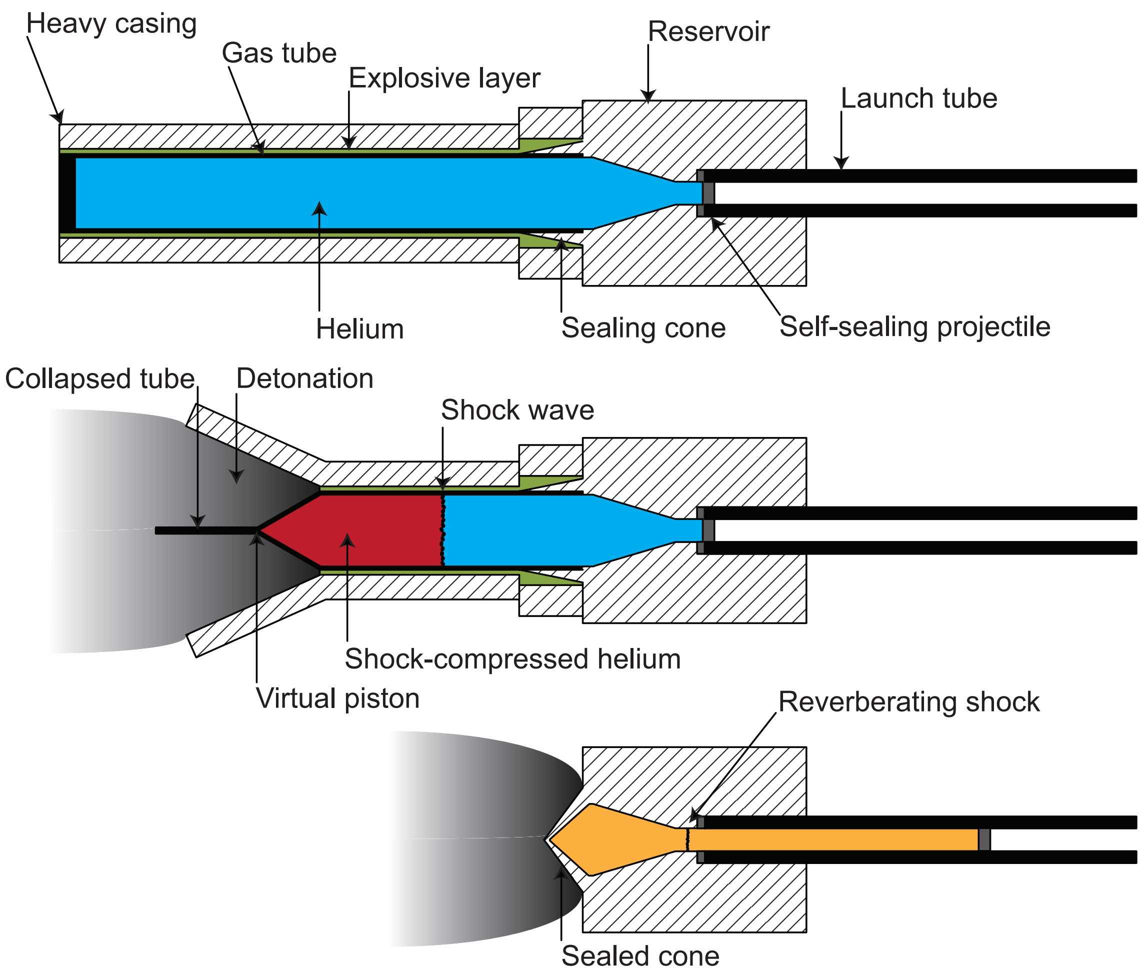

Figure 1–9: Schematic of the launch cycle of the implosion-driven launcher

launcher is that explosives allow for unique modes of operation where one can continue to compress the driver gas, even after the reservoir has been sealed. As will be seen, explosives offer the opportunity to deliver a large amount of energy to the driver gas during projectile acceleration, thereby maintaining a high driving pressure for much longer. Although the implosion-driven launcher is a single shot device, by using low-grade and low tolerance materials in the majority of the launcher fabrication, the cost can be kept well within the cost of a single 2SLGG shot. Furthermore, the implosion launcher typically has a much more compact design for a given projectile size, allowing it to launch large projectiles (>10 g) in a reasonably sized launcher.

The implosion driven launcher concept was first developed by the Physics International Company (PI) in the late 1960's [16, 26, 38, 39, 5, 6]. During its development, PI was able to launch a 2-g projectile to 12.2 km/s [38], a result that remains well outside the capacity of 2SLGG. Although the initial launcher development appears to have been successful, the project ended suddenly and very little information was published on its development. For this reason, much of the engineering know-how acquired during the development of the original launcher has been lost. Work at McGill University to re-develop and improve upon the PI design has been ongoing for the last several years. This section will give an overview of the major developments presented by the PI reports as well as work recently done at McGill, laying the foundation for the work presented in this study.

1.3.1 Linear Explosive Driver

Linear explosive drivers are devices which focus explosive energy into compressing a light-gas. The driver forms a column of gas with high internal and kinetic energy which can readily be used as propellant in a launcher. The driver is composed of a thin walled steel tube surrounded with a layer of explosive and a thick

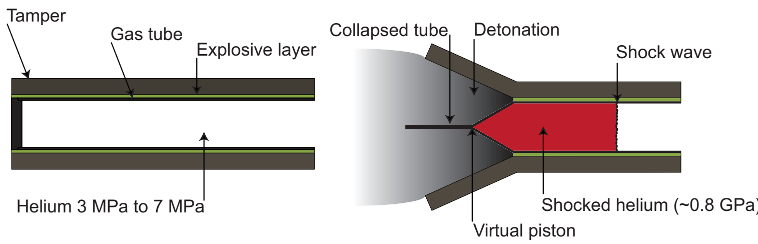

Figure 1–10: Ideal operation of the linear explosive driver

walled metal casing (tamper). The driver is pressurized with a light gas (usually helium), typically to pressures around 3.5 MPa for launcher applications.

The operation of the driver can be seen in Figure 1–10. The explosive is initiated on the end of the tube, imploding the steel walls and jetting the light-gas forwards. As the detonation progresses along the tube, the imploding walls act like a piston that travels forward at the detonation velocity of the explosive. This advancing piston dynamically compresses the light gas, driving a shock wave that travels faster than the explosive pinch, which in turn forms an increasingly long column of compressed gas behind the precursor shock wave. As mentioned previously, the shocked gas is highly energetic, having a velocity equal to that of the detonation (7 km/s), a high pressure (400 MPa), and high temperature (8300 K). The tamper which surrounds the explosive is used to focus the explosive energy inwards, as well as confine the thin walled steel tube exposed to the pressurized gas behind the shock wave.

As a first approximation, the pump tube can be modelled as a constant velocity planar piston travelling into a quiescent gas contained within rigid walls. Further, it can be assumed that the flow is one-dimensional (inviscid flow), and that the driver gas behaves as a perfect gas with a constant specific heat ratio (γ). By shifting the problem to the frame of reference of the shock wave, a quasi-steady analysis can be performed and the velocity of the precursor shock wave (U_{shock}), as well as the flow conditions behind the shock (particle velocity (U_1), pressure (p_1), temperature (T_1), speed of sound (a_1)) can readily be obtained:

$$U_{\text{piston}} = U_1; \tag{1.1}$$

$$M_{\text{shock}} = \frac{U_1}{a_o}\frac{\gamma+1}{4} + \frac{1}{2}\left[\left(\frac{U_1}{a_o}\frac{\gamma+1}{2}\right)^2 + 4\right]^{\frac{1}{2}} \tag{1.2}$$

$$U_{\text{shock}} = M_{\text{shock}} a_o \tag{1.3}$$

$$\frac{p_1}{p_o} = \frac{2\gamma M_{\text{shock}}^2 - (\gamma - 1)}{\gamma + 1} \tag{1.4}$$

$$\frac{T_1}{T_o} = \frac{(2\gamma M_{\text{shock}}^2 - (\gamma-1))(2 + (\gamma-1)M_{\text{shock}}^2)}{(\gamma+1)^2 M_{\text{shock}}^2} \tag{1.5}$$

$$\frac{a_1}{a_o} = \left(\frac{T_1}{T_o}\right)^{\frac{1}{2}} \tag{1.6}$$

$$\frac{\rho_1}{\rho_o} = \frac{P_1 T_1}{P_o T_o} \tag{1.7}$$

The description above did not include a number of non-ideal effects that need to be considered in order to understand the performance characteristics of real linear explosive drivers. A schematic of the three main non-ideal effects in the driver is shown in Figure 1–11, as well as a plot showing the progression of the shock velocity and standoff between the explosive-driven piston and the shock as the piston advances through the driver. As can be seen, the constant shock velocity predicted by the ideal model is not realized in experiments.

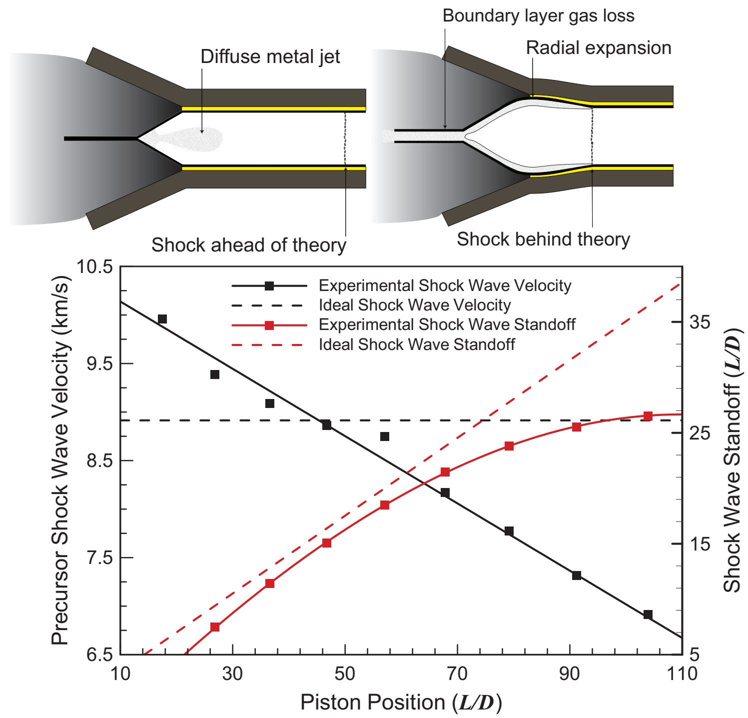

Figure 1–11: Non-ideal operation of the linear explosive driver

In the initial stages of the device, a diffuse metal jet is formed from the implosion of the thin walled steel tube. It is believed that this jet is an important factor in initially forming the precursor shock wave in the driver gas. Further, this jet is believed to be the reason that the precursor shock wave appears to be travelling faster than ideal theory would predict in the early stages of the device [35]. As the detonation progresses and the distance between the shock wave and the explosive-driven piston increases, the shock velocity begins to decay. This decay is related to two important effects: boundary layer formation in the shocked gas and expansion of the steel tube under the pressure of the shocked gas.

As the shock wave passes through the quiescent driver gas and sets it in motion, a velocity gradient is formed between the shocked gas and the driver tube. This forms a boundary layer that grows as the shocked gas flows through the driver tube.

The boundary layer will be thickest at the explosive-driven piston, where the gas has traveled along the tube the longest and has zero thickness at the shock front, where the gas has just been set in motion, thus having a shape similar to that pictured in Figure 1–11. The boundary layer, which is travelling significantly slower than the surrounding gas, must be jetted forward by the explosive-driven piston in order to remain in the driver. From the frame of reference of the piston, the boundary layer driver gas is approaching the piston at the detonation velocity (approximately 7 km/s). The explosive-driven piston must stagnate this relatively dense boundary layer gas in order for it to remain in the driver. As a result, large local pressures (on the order of gigapascals) are required to accelerate the boundary layer gas to the piston velocity. The pressure is sufficient to arrest the implosion of the steel tube and allow a portion of the gas in the boundary layer to leak through the pinch. Initially, this phenomenon arrests the jetting of tube wall material, and eventually leads to an increasingly large loss of driver gas. This gas loss attenuates the precursor shock wave, until a steady state is reached where the mass of gas entering the shock wave is equal to the mass of gas leaving the pinch. At this point the shock wave travels at the same velocity as the pinch and the length of the shocked gas column no longer increases.

Similar boundary layer effects have been observed in shock-tubes and explosively lined channels. In an analysis similar to the original shock-tube boundary layer treatment by Mirels [25], Moore showed that the decay in the velocity of the precursor shock wave along the driver correlated well to a model in which the shock velocity decays as a function of the length to diameter ratio (L/D) of the driver [26]. Indeed, experiments performed with drivers of different sizes (0.8 cm OD, 0.6 cm OD, 8 cm OD) showed that the decay in precursor shock wave velocity scales very well with its L/D, indicating that that boundary layer growth, which is a function of the L/D over which the shocked gas has travelled, may be the dominant non-ideal effect in linear explosive drivers.

As is demonstrated in Figure 1–11, the pressure in the shocked gas is sufficient to significantly expand and possibly rupture the pressurized steel tube ahead of the explosive pinch. As the distance between the precursor shock wave and the explosive pinch increases, the steel tube is exposed to the post shock pressure for increasingly long intervals of time. Szirti developed a model for the decay of the precursor shock wave velocity caused by the expansion of the pressurized tube [35]. The model and corresponding experiments showed that significant reductions in the decay of the precursor shock wave velocity are seen for drivers with thick walled tampers that provide confinement to the thin walled driver tube. Szirti also showed that the confinement provided by the tamper is more effective for small explosive thicknesses, which allow the inertial confinement of the tamper to be felt earlier in the driver tube expansion [35]. For this reason, care must be taken to select appropriate thicknesses for the explosive and the pressurized steel tube in order to provide adequate confinement and avoid rupture while ensuring complete implosion of the steel tube.

It is should be noted that expansion losses are also expected to be independent of driver size (diameter) as long as the L/D is held constant. For a fixed L/D, the amount of time the pump tube is exposed to the post shock pressure, which is a function of the distance between the shock and the pinch, is proportional to the diameter of the driver (for a fixed L/D). However, the change in driver volume as a function of time is inversely proportional to its diameter. As a result, expansion losses will be independent of driver size. A more thorough analysis of the scalability of expansion losses is presented in Section 5.1.

The non-ideal effects present in the linear explosive driver place practical limits on the design of the implosion driven launcher. First, the decay of the shock velocity due to the boundary layer phenomenon limits the length to diameter (L/D) of the driver. Indeed, for very long drivers, the shock velocity can decay to the point where the temperature, pressure and velocity of the shocked gas has dramatically decreased, thus significantly hindering the performance of a potential launcher. As can be seen from the shock velocity data in Figure 1–11, driver lengths should be kept below 60 diameters in order to maximize the performance of the driver. It should be mentioned at this point that excessively short drivers may also underperform given the fact that a finite time is needed for the precursor shock wave to emerge out of the explosive pinch. Experiments reported by Watson measured this shock formation distance to be 4.3 diameters [38], while experiments by Szirti placed it at 10.5 diameters [35]. This effect is only significant for short drivers given that the shock, which is initially overdriven by the diffuse metal jet, quickly recovers the ideal trajectory.

Another important limit to launcher design is the maximum fill pressure at which the driver can operate. Rupture of the driver tube, as well as difficulties in collapsing highly pressurized tubes limits the maximum fill pressure of standard linear explosive drivers to approximately 10 MPa [33]. Given that this fill pressure would correspond to a launcher driving pressure of over 10 GPa, it is not seen as a significant limitation in the design. As will be seen, launcher fill pressures are typically in the 2 to 8 MPa range.

The design of linear explosive drivers remains highly empirical. General guidelines on the dimensions of the pressure tube, explosive layer, and tamper are given in Table 1–1. These dimensions have been established using data from both the PI and McGill implosion launcher projects [26, 38, 35]. At moderate fill pressures ($<$ 7 MPa), the performance of the drivers is fairly insensitive to the parameters given in Table 1–1, as long as they are within the acceptable range. However, experiments reported by Moore and Watson showed that for very large fill pressures, it is desirable to operate at the upper range of pump tube thickness and explosive mass [26, 38]. It should be noted that the performance of the driver will be least sensitive to the thickness of the tamper. As a general rule the thickest readily available and affordable mechanical tubing should be used. The explosive thickness design guideline can also be expressed as a minimum Gurney velocity. Gurney developed a series of analytical solutions to estimate the final velocity of flyer plates, requiring only the mass of the explosive charge (C), the mass of the tamper (N), the mass of the flyer plate (M), and the explosive's Gurney energy ($\sqrt{2E}$), an empirical parameter [21]. The Gurney model, shown in Equations 1.8 and 1.9, is written for planar geometry and calculates the far-field velocity of the flyer [15]. Although the equation certainly does not predict the actual inward velocity of the driver tube (near field cylindrical implosion velocity), it can serve as a better empirical design parameter than M/C since it compensates for the fact that the impulse on the driver tube will be different depending on the explosive (Gurney energy will vary) and tamper thickness. Szirti found that a Gurney velocity above 1.3 km/s is generally desired [35].

$$U = \sqrt{2E}\left[\frac{1+A^3}{3+3A} + \frac{N}{C}A^2 + \frac{M}{C}\right]^{-\frac{1}{2}} \tag{1.8}$$

$$A = \frac{1+2M/C}{1+2N/C} \tag{1.9}$$

Table 1–1: Recommended design parameters for a linear explosive driver [38, 5]

Driver Tube t/D	Explosive Thickness (M/C)	Explosive Thickness (Gurney Velocity)	Tamper t/D
0.04 - 0.07	0.17 - 0.08	> 1.3 km/s	0.2 - 0.3

A final design note will be made on the choice of explosive in the driver. First, the explosive needs to have a small critical diameter, in order to ensure the detonation does not arrest itself along the thin annulus in the driver. Further, a dense explosive offers the advantage of requiring a thinner explosive layer, thus improving the confinement of the thin walled pressure tube. Explosive with a high detonation velocity (VOD) has the advantage of requiring less explosive due to its higher detonation pressure and providing a faster piston velocity, which theoretically improves the performance of the driver gas as a propellant (see Section 4.2.2). A faster piston velocity also makes the driver less prone to expansion and bursting, since the driver tube is exposed to the post shock pressure for a shorter amount of time. The majority of experiments reported by PI and McGill used either sensitized nitromethane (VOD 6 km/s, density 1.1 g/cc) or Detasheet/Primasheet1000 (VOD 7 km/s, density 1.5 g/cc). Although there are a number of explosives with equally small critical diameters, higher densities, and higher detonation velocities, these explosives have been used primarily for practical reasons of accessibility and ease of use in annular geometries. Furthermore, experiments performed by Moore compared the performance of a pump tube with C-4 (VOD 8 km/s, density 1.6 g/cc) to one with nitromethane diluted with 30% alcohol (VOD 5.5 km/s, density 1 g/cc) and found their performance to be nearly identical.

1.3.2 Single Stage Implosion Driven Launcher

As was shown in Figure 1–9, a single stage implosion-driven launcher is essentially composed of a linear explosive driver attached to a thick walled reservoir to

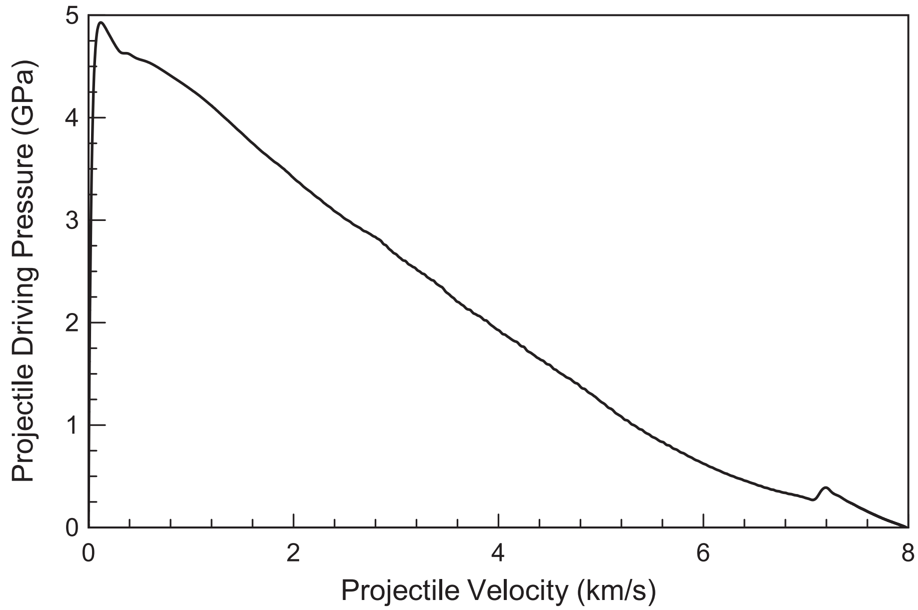

Figure 1–12: Typical decay of the projectile driving pressure as of function of velocity in an implosion-driven launcher

contain the high pressure gas, and a launch tube through which the projectile accelerates. Typically, the explosively driven piston reaches the end of the driver in the early stages of the launch cycle. A conical steel section surrounded with explosives is placed at the beginning of the reservoir section to seal the driver gas. Figure 1–12 shows the evolution of the pressure against the projectile as a function of its velocity for a typical launch cycle. As can be seen, the pressure against the projectile is highest at the beginning of the cycle, when the shock wave reflects off the projectile, and then decays as the driver gas expands to propel the projectile.

The two best single-stage launcher results from the Physics International program are given in Table 1–2, along with the known design details of the launcher. As can be seen, PI was able to reach velocities of 8 km/s with a single-stage launcher. It should be noted that this velocity was reached with two vastly different size launchers (0.17 g and 2 g), demonstrating the scalability of the launcher. The velocity

Table 1–2: Physics International single stage implosion driven launcher experiments [38, 5]

Projectile Mass (g)	Velocity (km/s)	Launch Tube Diameter (mm)	Projectile	Driver Fill Pressure (MPa)	Driver to Launch Tube Area Ratio	Driver Length (L/D)	Reservoir to Driver Length Ratio
2.0	7.8	15.9	0.5 cal. Mg-Li	7.5	4.8	28	0.18
2.0	8.0	15.9	0.5 cal. Mg-Li	3.8	4.8	28	0.18
0.17	8.8	6.35	0.5 cal. Mg-Li	3.8	4.8	28	0.14

potential of a single-stage implosion launcher appears to be comparable to that of a 2SLGG, which is surprising given that the peak projectile loading is almost an order of magnitude larger in the implosion-driven launcher. An important limitation to the performance of the single-stage implosion launcher is the extreme radial expansion that occurs in the reservoir due to the elevated driver gas pressures. Indeed, as the shock reflects off the projectile, the driver gas pressure reaches 3 to 7 GPa. This pressure is sufficient to expand the reservoir during the early stage of the launch cycle, thus significantly reducing the base pressure on the projectile.

Early launcher experiments reported by PI performed well below expectations, with velocities being more than 30 percent slower than those predicted by an ideal internal ballistics solver with rigid launcher walls. Upon recovering launchers and noticing the extreme radial expansion, efforts were made to incorporate the radial expansion of the launcher walls into the computational internal ballistics model. The modified internal ballistics solver confirmed that reservoir expansion was the primary source of loss in the implosion driven launcher, responsible for performance reductions of up to 30 percent. The modified internal ballistics solver was able to accurately reproduce experimental results and was used throughout the program as a design tool, notably in the development of two-stage launchers. Although details of the computational model were never published, the general scheme was presented by Watson [38]. A similar capability has been developed at McGill, using modern computational algorithms to simulate reservoir wall expansion as well as a number of other non-ideal effects. The computational model will be presented in detail in this study. The scheme will be used throughout this work as a design tool to guide the development of the implosion launcher.

Although the operation of the implosion launcher scheme may appear simple, its performance is strongly affected by a number of critical design decisions related to the driver, the reservoir, the driver gas, and the projectile. There exists very little literature on internal ballistic considerations of implosion driven launchers. The main focus of single-stage launcher design during the Physics International project was related to the development of the linear explosive driver. Few details were published on the internal geometry of the launcher. As a result, the justifications for a number of design decisions were never reported. Attempts by Szirti to perform a systematic experimental study of certain internal ballistics parameters [34] provided some insight into design considerations, but is of limited use given that the results are not directly transferable to typical implosion-driven launchers for a number of reasons, including unusually thick projectiles, unusually low gas fill pressure, and unusually long drivers. For these reasons, a major portion of this study will focus on establishing an understanding of the key internal ballistics parameters of the implosion-driven launcher and their effect on the launch cycle. Although some of this work will rely on past and present experimental results, a large portion of the results will be established with the use of the computational model of the launcher.

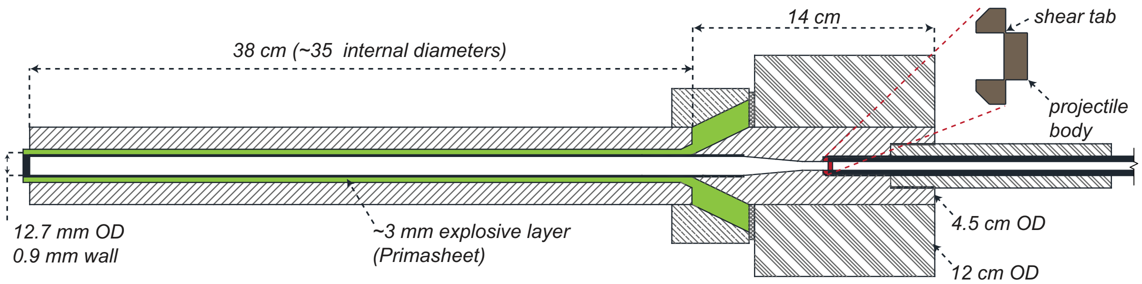

Figure 1–13: Drawing of a typical implosion driven launcher and self sealing projectile

Figure 1–13 shows a drawing of a typical implosion-driven launcher. Previous experiments at McGill have led to the refinement of the launcher mechanical design. The linear explosive driver tube and tamper are made of standard mechanical tubing. The driver tube is typically welded to the reservoir. The reservoir is made of a single piece that contains the sealing cone, the area change section and the threads which allow the launch tube and launch tube holder sleeve to connect to the reservoir. The reservoir is the only part of the launcher that requires extensive machining. The launch tube is made of stock tubing that has been honed and cleaned to improve the internal finish. A sleeve is added to the launch tube to provide additional confinement against the large driver gas pressure. Care must be taken to ensure that the components of the launcher are appropriately sized to be able to withstand the large pressure in the reservoir and launch tube. Although all components of the launcher are certain to yield, it is important to prevent fracture of the reservoir, damage to the sealing cone, and rupture of the barrel in the early stages of the launch. Changes in launcher geometry, fill pressure, and projectile mass have an important effect on the expansion history of the reservoir. As will be seen, the internal ballistics solver with reservoir expansion is an important tool in ensuring that components are properly sized.

Experiments at McGill have also provided valuable insight into projectile design. The large driving pressures in the implosion-driven launcher can lead to severe projectile damage. Furthermore, the velocity potential of the implosion-driven launcher is strongly influenced by the mass of the projectile, which favours thin projectiles made of low density materials. Designing a lightweight and relatively fragile projectile that is capable of surviving the launch cycle is an important aspect of the implosion launcher design. Experience from PI has shown that although plastics can be launched, the projectiles are often heavily deformed and ablated. However, PI found that lightweight magnesium alloys could be launched intact, despite the maximum driving pressure being almost an order of magnitude above their yield strength. The projectiles for the state of the art McGill launchers are made of ZK60, a widely available lightweight magnesium alloy with impressive strength properties. The effect of varying projectile thickness, mass, and material on launcher performance will be further explored in this work.

A fast acting valve must be used in order to isolate the projectile from the pressurized driver gas before the start of the launch cycle. This can be done using a standalone diaphragm, which is typically composed of a thin Mylar or brass disc that ruptures when the shock wave from the driver reaches it. However, the ruptured diaphragm has the potential to damage the projectile. Seifert presented the design of a self sealing projectile which includes tabs that extend from the projectile to a larger diameter and seal against an o-ring [30]. The tabs are connected to the projectile by a very thin web (typically < 0.3 mm) which simply shears off when the projectile is exposed to the reflected shock pressure. The McGill self-sealing projectile design can be seen in Figure 1–13, and is described in detail in Appendix B.

Although the performance of the single stage implosion launcher is comparable to state of the art 2SLGG, significant improvements can be made by further compressing the driver gas during the launch cycle. As was seen in Figure 1–12, the projectile driving pressure in an implosion launcher decays quickly, which means that the average projectile acceleration is far less than it could be in a launcher where the driving pressure is maintained at a nearly constant value. By compressing the driver gas in the reservoir, it is possible to reverse the decay of the driving pressure, and provide a significantly higher average acceleration to the projectile.

1.3.3 Auxiliary Pump Cycle

The auxiliary pump cycle, pictured in Figure 1–14, uses explosives to drive the reservoir walls inwards in order to compress the driver gas. This allows the launcher to maintain a high base pressure for much longer, significantly improving performance. Although the design of the auxiliary pump geometry is quite simple, its implementation is complicated by timing considerations. The reservoir implosion must occur early enough to meaningfully increase the projectile driving pressure. However, the detonating explosive drives a stress wave in the reservoir which could damage the projectile. Therefore, the timing must be late enough that the projectile does not interact with the stress wave, which is travelling in the steel at approximately 5.5 km/s. The stress wave requirement means that the auxiliary pump technique is much more effective for light projectiles that are accelerated to velocities greater than 5.5 km/s very quickly. Indeed, the lighter the projectile the faster the auxiliary pump can be initiated and the greater the potential increase in projectile driving pressure. For this reason, the technique is not very effective for projectiles being accelerated to velocities around and below 5.5 km/s. It should also be noted that when using an explosive with a detonation velocity above 5.5 km/s, the stress wave

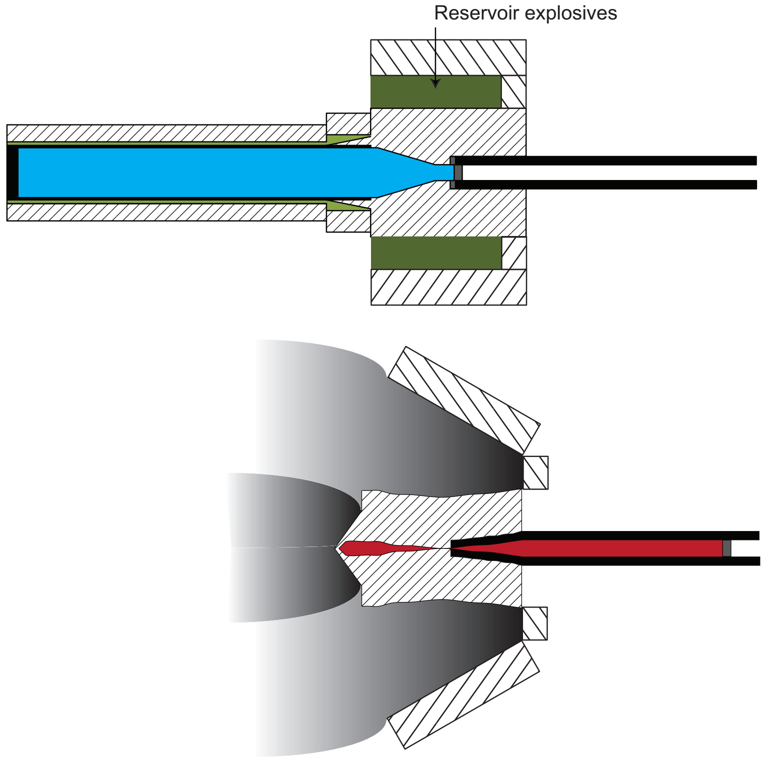

Figure 1–14: Operation of an implosion-driven launcher with an auxiliary pump cycle

will be dragged into the steel at the explosive detonation velocity until the end of the explosive section. Therefore, using an explosive with a detonation velocity similar to that of the wave propagation speed in the steel is favourable, as it makes it possible to initiate the auxiliary pump cycle earlier, allowing the back of the reservoir to be imploded faster.

During the Physics International project, a single stage launcher with a simple auxiliary pump cycle demonstrated the capability to accelerate a 2-g projectile to 10.6 km/s, which represents a 2.6 km/s improvement over the single stage launcher [38]. PI was able to further improve the performance of the launcher by adding a section of fast explosive (Astrolite) that extended another 12.5 launch tube diameters beyond the standard auxiliary pump. This launcher reached a velocity of 12 km/s [38]. Table 1–3 summarizes three of their most successful auxiliary pump

Table 1–3: Physics International experimental results for auxiliary pump launcher experiments [38]

Projectile Mass (g)	Velocity (km/s)	Projectile Diameter D_p (mm)	Driver Fill Pressure (MPa)	Reservoir Diameter (D_r/D_p)	Reservoir Mass to Explosive Mass (M/C)	Projectile to End of Explosives (L/D_p)
2.0	10.2	15.9	3.7	6.4	3.4	12.5
2.0	10.6	15.9	7.5	6.4	3.4	12.5
2.0	12.0	15.9	7.5	6.4	3.4	25

shots, including the size of the reservoir and explosive charge that was used. All launchers have the same internal geometry as the 2-g single-stage launchers in Table 1–2. It should be noted that once again, there is very little difference between the performance of the high pressure and low pressure launchers.

Although the data given in Table 1–3 offers a good starting point for the design of an auxiliary pump cycle, a number of details regarding the geometry and timing of the explosive charge cannot be taken directly from the PI design. Particularly, changes in fill pressure, projectile material, launcher geometry, and length of explosive charge, mean that the timing used by PI is not directly transferable. The internal ballistics solver developed for the project will be used to determine the most appropriate initiation time for the reservoir explosives.

1.4 Scope of Study

As was seen in this review of the concept, the implosion-driven launcher has the potential to reach velocities well above the capacity of current hypervelocity launcher facilities. This work will present the development of a computational gasdynamics scheme capable of simulating the launch cycle of the implosion launcher. The scheme will be coupled to a dynamic structural mechanics model to simulate the radial expansion of the launcher walls under the high driver gas pressures. Further, a number of non-ideal effects having an important influence on the launcher performance will be integrated to form a complete computational model of the implosion-driven launcher. The model will be used in conjunction with classical internal ballistics theory to gain valuable understanding of the key design parameters of the launcher and eventually optimize the geometry of the single stage implosion-driven launcher. The model will then be used in conjunction with experimental data to design the auxiliary pump cycle in order to maintain a high driving pressure on the projectile and maximize the performance of an eventual two-stage launcher.

CHAPTER 2
Development of a Quasi 1-D Lagrangian Gasdynamics Internal Ballistics Model

A quasi-one-dimensional Lagrangian gasdynamics solver has been developed in order to model the internal ballistics of the implosion-driven launcher. The solver uses a second-order accurate (in space and time) numerical scheme developed by von Neumann and Richtmyer [36], with a modified energy formulation developed by Noh [27]. The von Neumann artificial viscosity allows the numerical solver to capture shock waves, which is necessary due to the dynamic compression of the gas in the implosion-driven launcher. This section will present the Lagrangian formulation of the conservation equations and their corresponding finite difference equations. Particular attention will be placed on the artificial viscosity formulation and the corresponding stability criterion. The gasdynamics solver will then be validated against a number of analytical gasdynamics solutions, as well as analytical and computational internal ballistics solutions.

In developing a one-dimensional ballistics solver, there is a significant advantage to using a Lagrangian formulation, wherein the cells move with the flow, versus an Eulerian formulation, where the flow moves across fixed cells. As the driver compresses the gas and the projectile accelerates forward, the boundaries of the ballistics solver are constantly moving; an Eulerian formulation requires the cells to be remapped at every iteration, while a Lagrangian formulation simply allows the cells to move with the boundaries. Although the numerical scheme presented in this chapter is far from being state of the art (first published in 1950), it continues to be widely used in large part for its simplicity in modeling one-dimensional problems with moving boundaries [41]. There exists more elegant formulations for resolving numerical shock waves (notably Godunov's method), which do not require the use of non-physical artificial viscosity terms to stabilize the solution. However, the von Neumann artificial viscosity formulation can deliver adequate results in an internal ballistics solver, where the user is ultimately interested in the projectile velocity, which is not particularly sensitive to the level of resolution of shock waves and other features in the flow. Before beginning to develop the numerical scheme, the function of the solver as well as its inherent assumptions and limitations should be clearly outlined:

1. The solver determines the properties of a gas (velocity, pressure, specific volume, internal energy) in a one-dimensional planar geometry with a circular cross-section for time dependent (i.e., unsteady) problems.
2. It is a purely hydrodynamic solver, which means that the only force acting on the fluid is pressure. The model does not take into account a number of other phenomena that may be present in the flow, including heat transfer, viscosity, chemical reactions, magnetic forces, and strength effects. However, it should be noted that the solver can be extended to simulate these effects.
3. It is a quasi-one-dimensional solver, which means that although the flow cross section can change, the flow is always uniform at a given cross section and only has one component of velocity.
4. The solver will use a perfect gas equation of state, meaning that the gas is assumed to behave according to the ideal gas law and have constant specific heats (c_p, c_v and γ are constant). However, it should be noted that slight

modifications to the pressure formulation allow the solver to use a variety of other equations of state.

5. The fluid flow is treated as isentropic outside regions of strong compression (shock waves). In shock waves, where the flow is non-isentropic, an artificial viscosity term (q) is used to generate a continuous (smoothed) solution that satisfies the conservation equations.

2.1 Introduction to the von Neumann Richtmyer Scheme

The first step in deriving the numerical scheme is to define the artificial viscosity term (q). There are two main problems in treating shock waves with a numerical model. First, a shock wave is a nearly discontinuous phenomenon that occurs over a distance that is much smaller than the cell size of the numerical model. Furthermore, a shock wave is a viscous process in which strong dissipative forces (due to the large gradients in the fluid properties) generate entropy. This is a highly irreversible process (large entropy rise), which means that the isentropic equations generally used in the solver do not directly apply. Artificial viscosity is a way of artificially increasing the fluid viscosity around large velocity gradients such that the shock wave is smeared out over a number of cells, allowing it to be resolved by the computational model. This viscous loss term does work against the pressure in regions of strong compression, which allows the shock wave to be a non-isentropic process. The formulation of the artificial viscosity must allow the numerical scheme to satisfy the conservation of mass, momentum, and energy across the shock wave (Rankine-Hugoniot relations).

The expression for the artificial viscosity used in this work is given by Equation 2.1. As can be seen, the formulation is such that the q term is only large in regions of strong gradients (large dU/dx). The inequality ensures that the dissipative term only exists in compression, which allows strong expansion gradients to remain isentropic. C_0 and C_1 are constants, typically set to 1.2 and 0.5, respectively. l determines the length scale over which the shock wave is spread out. This formulation results in a shock thickness of approximately $3l$. Finally, it should be noted that if a Lagrangian formulation is used for the velocity gradient ($dU/dx = \Delta U/L_{\text{cell}}$, where L_{cell} is the cell size) and the length scale l is also taken as the cell size, L_{cell} will cancel out of the equation. This is very convenient because the shock thickness will be of approximately 3 cells for any cell size and shock strength. A thorough review of the intricacies of artificial viscosity formulations can be found in the paper by Noh [27]. It should be noted that the original artificial viscosity scheme [36] did not include the linear component of artificial viscosity (C_1 term), which is not strictly necessary to conserve momentum and energy. However, this linear component helps to reduce oscillations around large gradients.

$$q = C_0 \rho l^2 \left(\frac{dU}{dx}\right)^2 - C_1 \rho a l \left(\frac{dU}{dx}\right) \qquad \text{for} \frac{dU}{dx} < 0 \tag{2.1}$$

$$q = 0 \qquad for \frac{dU}{dx} > 0 \tag{2.2}$$

Now that the artificial viscosity has been properly defined, the equations for the conservation of mass, momentum, and energy of a fluid particle can be written with the addition of the viscous loss q. As will be seen, q is essentially a viscous pressure that opposes the fluid pressure. Defining x as the Lagrangian space coordinate (position of the fluid particle relative to the flow), and $X(x,t)$ as the Eulerian space coordinate (actual position of the particle), we can write the following equations for the specific volume (v) and velocity (u) of the fluid particle:

$$v(x,t) = v_o(x) \left(\frac{\partial X(x,t)}{\partial x}\right) \tag{2.3}$$

$$u(x,t) = \frac{\partial X(x,t)}{\partial t} \tag{2.4}$$

We can now write an expression for conservation of mass, momentum, and energy in a Lagrangian frame of reference:

$$\frac{\partial v(x,t)}{\partial t} = v_o(x)\frac{\partial U(x,t)}{\partial x} \tag{2.5}$$

$$\frac{\partial U(x,t)}{\partial t} = -v_o(x)\frac{\partial}{\partial x}(P(x,t) + q(x,t)) \tag{2.6}$$

$$\frac{\partial e(x,t)}{\partial t} = (P(x,t) + q(x,t))\frac{\partial v(x,t)}{\partial t} \tag{2.7}$$

An equation of state, relating the specific volume, pressure, and internal energy of the fluid is also needed. Using the ideal gas equation of state, and applying the assumption of constant specific heats (perfect gas), an expression for pressure (p) as a function of the internal energy (e) and the specific heat ratio (γ) can be obtained:

$$P = \frac{RT}{v} \tag{2.8}$$

$$R = c_v(\gamma - 1) \tag{2.9}$$

$$T = \frac{e}{c_v} \tag{2.10}$$

$$P = \frac{e(\gamma - 1)}{v} \tag{2.11}$$

Although the system of equations is complete, the non-linear partial differential equations cannot be solved directly. However, a finite difference scheme, in which the exact differentials are approximated by differences over a finite cell size, can be used to solve these equations.

2.2 Finite Difference Equations for the von Neumann Richtmyer Scheme

In order to write the finite difference equations, one must define the numerical scheme which will be used to solve the finite difference equations. The von

Neumann-Richtmyer scheme uses a "leap frog" predictor-corrector technique, which is illustrated by the $x - t$ schematic in Figure 2–1. Being a Lagrangian scheme, each cell is composed of a fixed mass of fluid with boundaries that move with the flow. The specific volume, internal energy, and pressure are defined at the centre of the cell at the beginning of a timestep. By applying the conservation of momentum to the cell boundaries, the velocity of the cell boundary at the half-timestep ($t^{n+1/2}$) can be found. This cell boundary velocity is used to determine the change in the boundary position within the timestep (t^n to t^{n+1}). The cell boundary position can then be used, in conjunction with the conservation of energy and the equation of state, to obtain the thermodynamic properties of the cell at the next timestep (specific volume, specific internal energy, pressure, and artificial viscosity). As can be seen, the scheme uses the cell boundary velocity at the half-timestep to "leap" forward in time. This is best demonstrated by writing the complete set of finite difference equations.

The equations will be written for one timestep of a simple two cell system. As can be seen in Figure 2–1, the three cell boundaries are denoted as $j - 1$, j, and $j + 1$. At time n, the specific volume (v), pressure (p), internal energy (e), and artificial viscosity (q) of the cells ($j - 1/2$ and $j + 1/2$) is known. The position (X) of the cell boundaries at time n and the velocity (U) of the cell boundaries at time $n - 1/2$ are also known. The size of the next timestep (dt) is also known, as is the cell mass (m) which remains constant. For a quasi-one-dimensional solver, where the cross-sectional area of the flow is changing, the radius (r) of the cross-section at the cell boundaries and time n will also be known. It should be noted that the scheme will assume a linear variation in the radius within a cell.

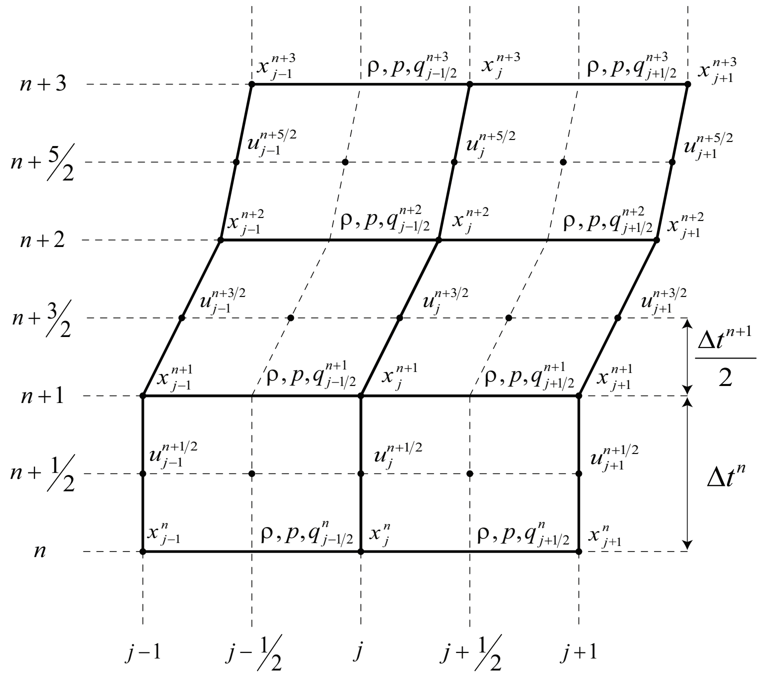

Figure 2–1: Diagram of the von Neumann Richtmyer numerical scheme for a two cell system

The first step is to apply the conservation of momentum to find the velocity of the cell boundary (U_j) at the half timestep. As can be seen, the equation finds the impulse (Newton's second law) on the cell boundary from the pressure forces. The mass of the cell boundary is calculated as the average of the two neighboring cells.

$$\Delta U = \frac{F}{m}\Delta t \tag{2.12}$$

$$U_j^{n+1/2} = U_j^{n-1/2} - \frac{\Delta t^{n-1} + \Delta t^n}{m_{j-1/2} + m_{j+1/2}}[(p_{j+1/2}^n + q_{j+1/2}^{n-1/2}) - (p_{j-1/2}^n + q_{j-1/2}^{n-1/2})]\pi(r_j^n)^2 \tag{2.13}$$

At this point, the boundary conditions for the two extremities of the domain are required (U_{j-1} and U_{j+1}). The five most common boundary conditions are given below: Infinite boundary:

$$U_{j+1}^{n+1/2} = U_j^{n+1/2} \tag{2.14}$$

Wall:

$$U_{j+1}^{n+1/2} = 0 \tag{2.15}$$

Piston:

$$U_{j+1}^{n+1/2} = \text{constant} \tag{2.16}$$

Projectile:

$$U_{j+1}^{n+1/2} = U_{j+1}^{n-1/2} + 0.5(\Delta t^{n-1} + \Delta t^{n}) \frac{p_{j+1/2}^{n} \pi (r_{j+1}^{n})^2}{m_{\text{proj}}} \tag{2.17}$$

Free surface:

$$U_{j+1}^{n+1/2} = U_{j+1}^{n-1/2} + \frac{\Delta t^{n-1} + \Delta t^{n}}{m_{j+1/2}} (p_{j+1/2}^{n} + q_{j+1/2}^{n}) \pi (r_{j+1}^{n})^2 \tag{2.18}$$

Constant Pressure:

$$U_{j+1}^{n+1/2} = U_{j+1}^{n-1/2} + \frac{\Delta t^{n-1} + \Delta t^{n}}{m_{j+1/2}} (p_{j+1/2}^{n} + q_{j+1/2}^{n} - p_{\text{boundary}}) \pi (r_{j+1}^{n})^2 \tag{2.19}$$

Now that the boundary velocities have been determined, the position of each cell boundary can be determined using the following equation:

$$X_j^{n+1} = X_j^{n} + U_j^{n+1/2} \Delta t^{n} \tag{2.20}$$

Using the new cell positions, the radius of the cross-section at the new cell boundaries can be determined. The radius will be a function of the position $r(X)$, where X is the location of the cell boundary, found in the previous step. Given that the mass of the cell is constant, the cell boundary position and the radius at this location can readily be used to find the specific volume of the cell. This formulation will assume a linear variation in the radius of the cross-section, although it should be noted that any formulation could be used by changing the calculation for the volume of the cell:

$$v_{j-1/2}^{n+1} = \frac{\pi}{3}\frac{(X_j^{n+1} - X_{j-1}^{n+1})}{m_{j-1/2}}[(r_j^{n+1})^2 + (r_{j-1}^{n+1})^2 + (r_j^{n+1})(r_{j-1}^{n+1})] \tag{2.21}$$

Next, the artificial viscosity of the cell can be determined using the form that was presented in Equation 2.1. The IF statement ensures that artificial viscosity is only applied to cells in compression:

IF $U_{j-1}^{n+1/2} > U_j^{n+1/2}$

$$q_{j-1/2}^{n+1/2} = C_0\frac{(U_{j-1}^{n+1/2} - U_j^{n+1/2})^2}{\frac{1}{2}(v_{j-1/2}^{n+1} + v_{j-1/2}^{n})} + C_1\sqrt{\gamma p_{j-1/2}^{n} v_{j-1/2}^{n}}\frac{(U_{j-1}^{n+1/2} - U_j^{n+1/2})}{\frac{1}{2}(v_{j-1/2}^{n+1} + v_{j-1/2}^{n})} \tag{2.22}$$

ELSE

$$q_{j-1/2}^{n+1/2} = 0 \tag{2.23}$$

The energy equation and the equation of state can now be used to determine the pressure and specific internal energy of the cell. This cannot be done directly since the pressure and internal energy appear in both equations. Noh proposed the following semi-iterative process using a temporary internal energy term (e_{temp}), which has been shown to conserve total energy:

$$\Delta e = P\Delta v \tag{2.24}$$

$$(e_{\text{temp}})_{j-1/2}^{n+1} = e_{j-1/2}^{n} - (p_{j-1/2}^{n} + q_{j-1/2}^{n-1/2})(v_{j-1/2}^{n+1} - v_{j-1/2}^{n}) \tag{2.25}$$

$$p_{j-1/2}^{n+1} = \frac{(e_{\text{temp}})_{j-1/2}^{n+1}(\gamma - 1)}{v_{j-1/2}^{n+1}} \tag{2.26}$$

$$e_{j-1/2}^{n+1} = e_{j-1/2}^{n} - \frac{1}{2}(p_{j-1/2}^{n} + q_{j-1/2}^{n-1/2} + p_{j-1/2}^{n+1} + q_{j-1/2}^{n+1/2})(v_{j-1/2}^{n+1} - v_{j-1/2}^{n}) \tag{2.27}$$

Finally, the proper timestep size must be chosen for the next step in the calculation. The timestep size is typically made as large as possible, while ensuring

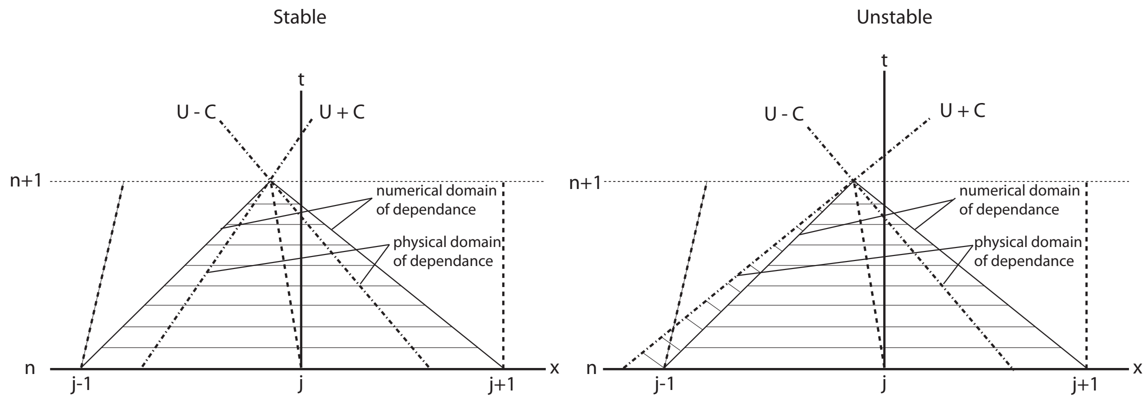

Figure 2–2: Schematic of CFL condition in a Lagrangian frame of reference

the stability of the scheme. An unstable scheme will result in overshoots and oscillations growing uncontrollably, leading to unphysical solutions. The first criterion which is necessary for stability is that the timestep must be small enough such that the numerical domain of dependence encompasses the entire physical domain of dependence. This is known as the Courant-Friedrichs-Lewy (CFL) condition, and its meaning is illustrated in Figure 2–2. As can be seen, signals propagate in the fluid at the flow velocity (U) plus the speed of sound ($\pm a$). The numerical scheme being used is explicit and uses a stencil that encompasses the two adjacent cells. This means that the state of a cell at the next timestep is only dependent on its two neighboring cells. If a signal has time to propagate across more than an entire cell during a timestep, some of the information will be lost, and the result will be unphysical. The CFL condition for a Lagrangian scheme is given in Equation 2.29:

$$\Delta t = \frac{\Delta X}{\Delta U + a} \tag{2.28}$$

$$\Delta t^{n+1}_{j-1/2} = \frac{X^{n+1}_j - X^{n+1}_{j-1}}{U^{n+1/2}_{j-1} - U^{n+1/2}_j + \sqrt{\gamma p^{n+1}_{j-1/2} v^{n+1}_{j-1/2}}} \tag{2.29}$$

Although the CFL condition is necessary for stability, it is not sufficient. It is possible that the numerical errors introduced by representing the partial differential equations with a finite difference scheme may grow unboundedly. The von Neumann stability analysis can be used to determine the size of the timestep necessary for the scheme to be stable by observing how small oscillations grow with time in the linear finite difference scheme. The end result of the analysis performed by von Neumann is given in Equation 2.30, which can be used to determine the proper timestep size for the next iteration. It should be noted that since the timestep size must be the same for all cells, it is necessary to perform this calculation for all cells in the solver, in order to determine the timestep size for which all cell calculations will be stable.

$$\Delta t_{j-1/2}^{n+1} = \frac{\gamma^{1/2}}{2C_0} \frac{X_j^{n+1} - X_{j-1}^{n+1}}{U_{j-1}^{n+1/2} - U_j^{n+1/2} + \sqrt{\gamma p_{j-1/2}^{n+1} v_{j-1/2}^{n+1}}} \tag{2.30}$$

Using the new time interval, the calculation can be continued to the next timestep. The calculation can then be repeated until the end of the simulation.

2.3 Validation of the Numerical Scheme

Validation of the numerical scheme will be performed in two steps. First, the numerical scheme will be verified against exact analytical gasdynamic solutions, including a study of the global order of accuracy of the scheme. Next, specific launcher validation tests will be performed, including comparison to analytical internal ballistics solutions and published computational data.

2.3.1 Gasdynamics Validation Tests

In order to verify the numerical scheme, a number of tests were performed to ensure the solver could reproduce analytical gasdynamic problems. Riemann problems, in which there is an initial discontinuity in the density, velocity, and/or pressure of the gas, are often used to validate computational gasdynamic schemes.

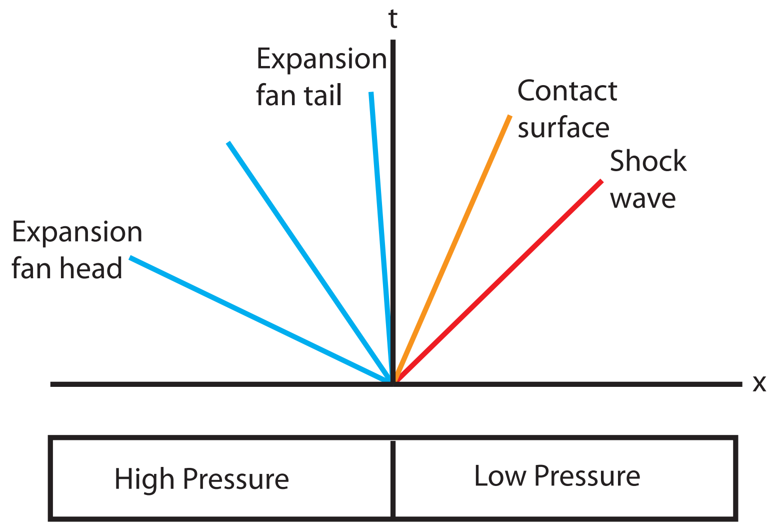

Figure 2–3: Wave diagram for the shock tube validation problem

Using an analytical Riemann solver, the exact density, velocity, and pressure profiles for a number of test cases can be compared to the results from the Lagrangian solver. Two particular test cases will be presented. The first test case is the shock tube problem (Sod's problem), in which a gas with a high pressure and density expands into a low pressure gas. The gas on both sides of the discontinuity is initially at rest. Figure 2–3 shows a wave diagram of the problem. Figure 2–4 shows the density, velocity, and pressure profiles in the flow. As can be seen, the Lagrangian solver properly captures the rarefaction wave, the contact surface, and the shock wave. The shock thickness is approximately four elements.

The shock tube problem can also be used to verify the true order of accuracy of the numerical scheme. By gradually decreasing the mesh interval size and measuring the change in the error between the exact solution and the Lagrangian solver results, one can obtain an order of accuracy for the scheme. In this case the residual was calculated by taking the sum of the square of the errors for each cell and dividing by the total number of cells (L^2 norm). The log of the residual as a function of

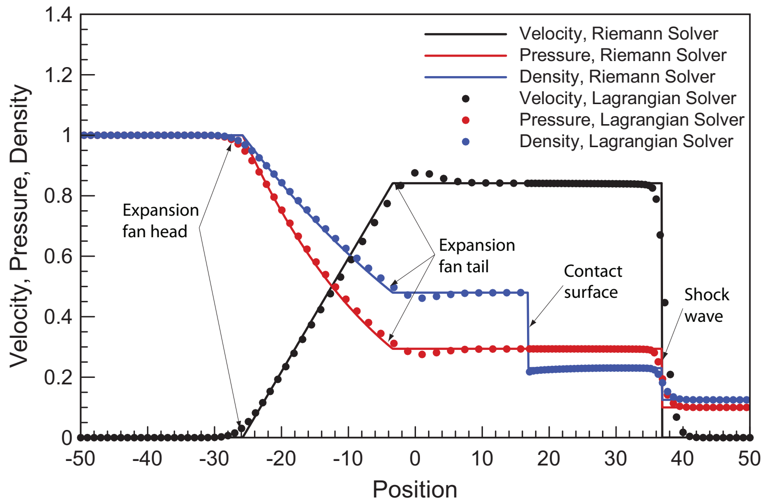

Figure 2–4: Comparison of velocity, density, and pressure profiles between the Lagrangian solver and an analytical Riemann solver for the shock tube validation case

the log of the number of cells is plotted in Figure 2–5 for the density, velocity and pressure residuals. The order of accuracy can be obtained by the slope of the curves. As can be seen, the global order of accuracy is measured to be approximately 1.1. As expected, the presence of discontinuities in the flow results in a lower order of accuracy than the theoretical order of accuracy of the scheme.

The second Riemann problem verifies the ability of the solver to capture strong shocks. Although the initial profile of density and pressure are uniform, the velocity of the gas on both sides of the discontinuity is opposite. This drives a strong shock on both sides of the discontinuity, as can be seen in Figure 2–6. The initial velocity of the gas has been set to produce a pressure and density ratio similar to that in the driver of the implosion-driven launcher. Figure 2–7 shows the density, velocity, and pressure profiles of the flow. Once again, the solver reproduces the analytical profiles quite well, and captures the strong shocks in approximately four elements. It should be noted that the erroneously low density in the center of the grid is caused by the q wall heating effect observed by Noh [27]. Although this error cannot be eliminated, its

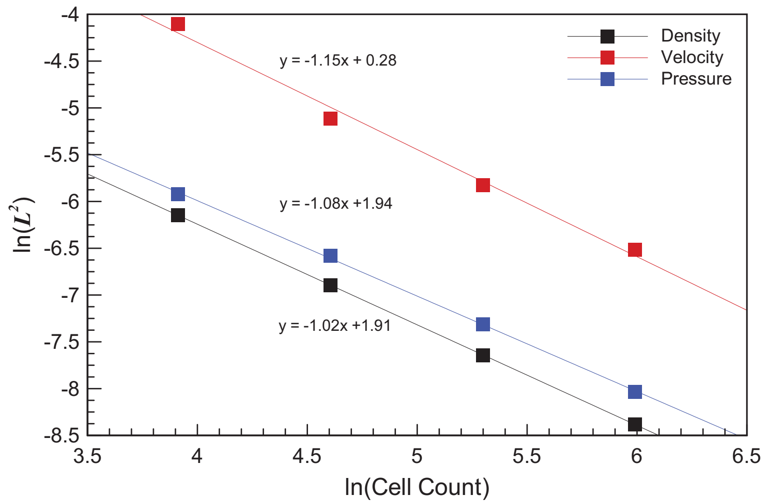

Figure 2–5: Sensitivity of the L^2 norm error to the number of cells used in the simulation

magnitude can be reduced by decreasing the size of the artificial viscosity constants. In particular, decreasing the linear component of artificial viscosity (C_1) can almost eliminate the error, although the resulting solution is much more oscillatory. For the current study, the numerical viscosity constants have been selected to be as small as possible while eliminating spurious oscillations. As a result, the wall heating error is not expected to affect launcher simulation results.

The final one-dimensional gasdynamic validation test that will be presented is that of a shock wave driven by a planar piston. This test simulates the behaviour of the gas being compressed by the explosive-driven piston in the linear explosive driver. The simulation results can be compared to the analytical solutions presented in Section 1.3.1. The initial conditions of the gas and the velocity of the piston have been chosen to match the conditions of a typical implosion-driven launcher driver. Figure 2–8 shows the density, velocity, and pressure profiles of the flow. Again, the Lagrangian solver results agree with the analytical solution. The wall heating error can again be seen in the density profile at the piston face.

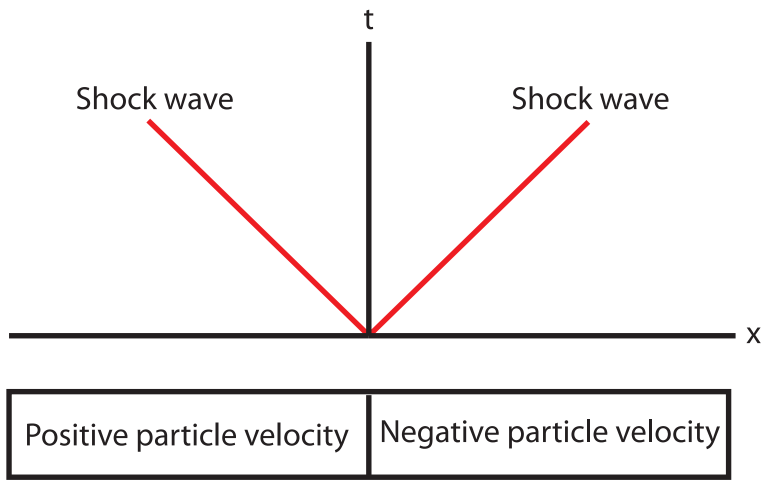

Figure 2–6: Wave diagram of the strong shock validation problem

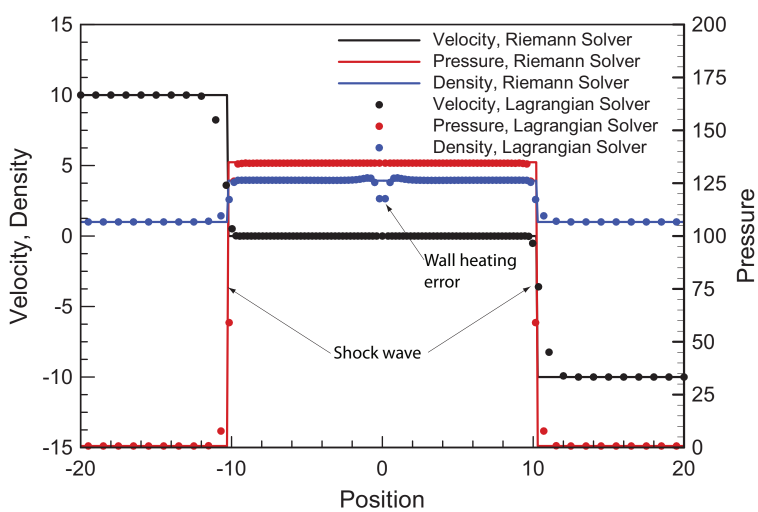

Figure 2–7: Comparison of velocity, density, and pressure profiles between the Lagrangian solver and an analytical Riemann solver for the strong shock validation case

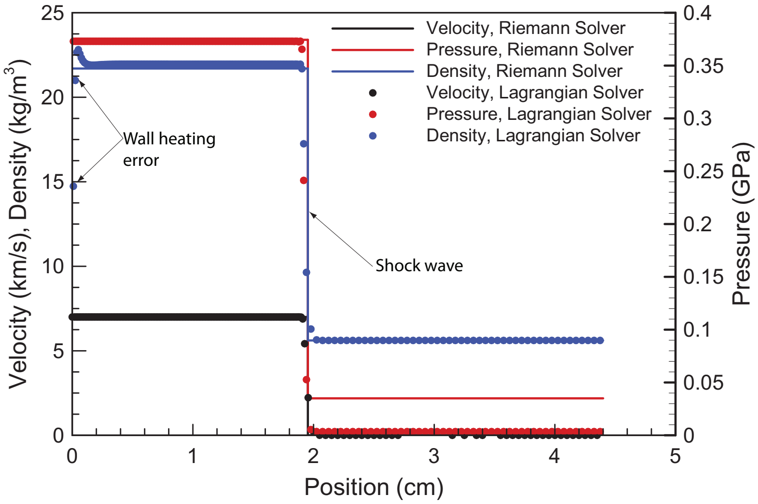

Figure 2–8: Comparison of velocity, density, and pressure profiles between the Lagrangian solver and the analytical solution for the planar piston problem

The ability of the solver to resolve quasi-one-dimensional gasdynamic effects also needs to be verified. This will be accomplished using a leaky piston test, in which a conical piston moves into a quiescent gas at a fixed velocity. As can be seen in Figure 2–9, the end of the conical piston has a hole through which gas can escape. Initially, from the frame of reference of the conical piston, the driver gas is travelling through the conical section at the piston velocity. If the size of the hole is sufficiently small as to choke the flow, a precursor shock wave will form at the throat and eventually travel ahead of the conical piston. Once the precursor shock wave is ahead of the area change, the system reaches a quasi-steady-state, where the precursor shock velocity and the flow properties behind the shock and through the area change section remain constant. In order to find an analytical solution for the particle velocity behind the shock wave and past the area change section, it is convenient to begin with a piston velocity (U_{piston}), a target particle velocity behind the shock wave (U_1), the initial speed of sound of the quiescent gas (a_o), and the specific heat ratio of the gas (γ). From Equation 1.6, the speed of sound behind the

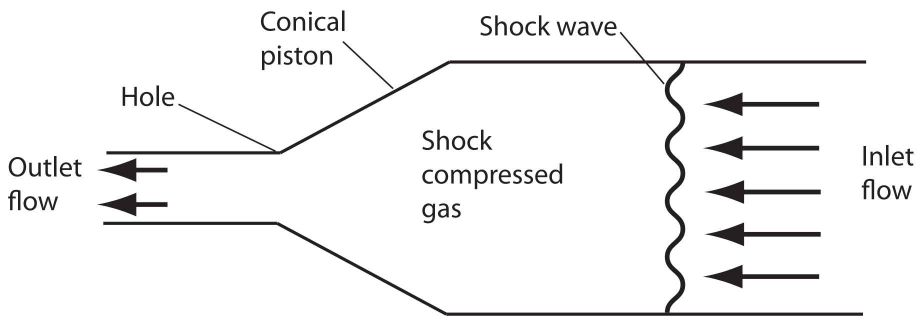

Figure 2–9: Schematic of the leaky piston validation problem

shockwave can be obtained. The following equations can then be used to determine the cross sectional area of the leak (A^*) and the particle velocity (U^*) past the leaky piston:

$$M_{\text{approach}} = \frac{U_{\text{piston}} - U_1}{a_1} \tag{2.31}$$

$$\frac{A}{A^*} = \frac{1}{M_{\text{approach}}} \left[\frac{2}{\gamma+1} \left(1 + \frac{\gamma-1}{2} M^2_{\text{approach}} \right) \right]^{\frac{\gamma+1}{2(\gamma-1)}} \tag{2.32}$$

$$U^* = \frac{a_1 \left(1 + \frac{\gamma-1}{2} M_{\text{appraoch}}\right)^{1/2}}{\left(1 + \frac{\gamma-1}{2}\right)^{1/2}} \tag{2.33}$$

Figure 2–10 shows the computational and analytical velocity profile for the test case. As can be seen, the solver matches the analytical solution. From this simple test it is possible to conclude that the code is capable of modeling choking in subsonic and supersonic flows. Furthermore, the choked mass flow rate through the throat matches theoretical predictions, which confirms that the variation in flow properties through the area change section is also correct.

2.3.2 Launcher Validation Tests

By applying the proper boundary conditions to the numerical scheme, the solver can be used to model the internal ballistics of a launcher. The ability of the solver to properly simulate the internal ballistics of a launcher is readily verified using

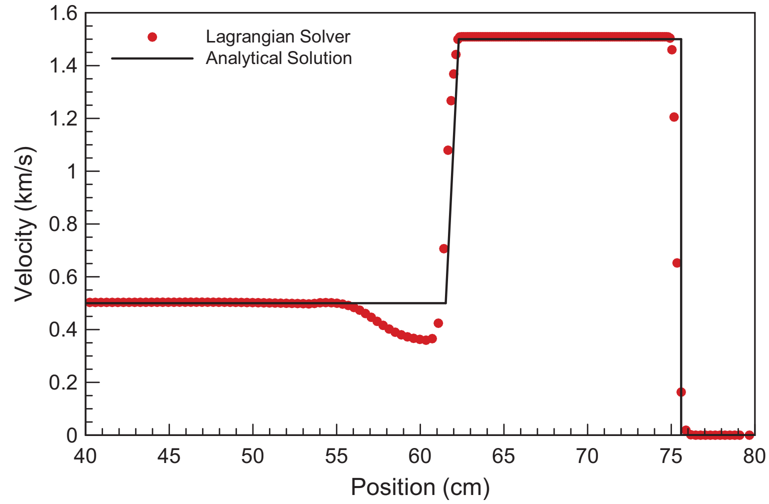

Figure 2–10: Comparison of the velocity profile between the Lagrangian solver and the analytical solution to the leaky piston problem

pre-burnt propellant ideal gas gun (PPIG) simulations. In a PPIG simulation, the launcher is modeled as a pressurized reservoir filled with an ideal gas that to propels a projectile. This simplified version of the internal ballistics of a launcher can be used to easily compare simulation results to analytical solutions and published computational results. This section will present a series of validation tests using analytical and computational solutions presented by Seigel [31].

Figure 2–11 shows a wave diagram for a constant area PPIG (chamber area is the same as the launch tube area). As the projectile begins to accelerate, an expansion wave travels towards to the back of the chamber, communicating the fact that the driver gas must accelerate forwards to propel the projectile. This expansion wave eventually reflects off the back of the chamber and catches back up to the projectile, communicating the fact that there is a finite quantity of gas available to accelerate the projectile. Before the first expansion wave catches up to the projectile, the launcher essentially operates as if it has an infinitely long chamber length, since the projectile has not been made aware that there is a finite quantity of gas in the

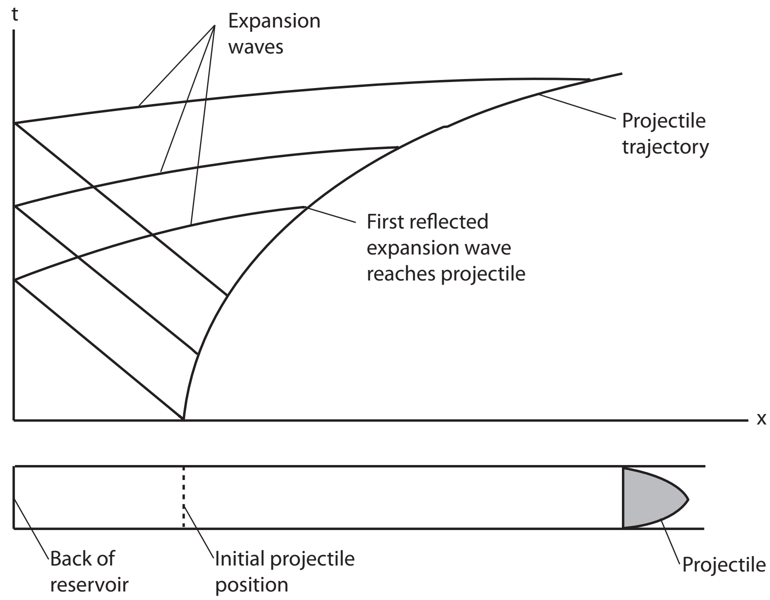

Figure 2–11: $x - t$ wave diagram showing the interaction of expansion waves with the projectile in a constant area PPIG

chamber. When the launcher operates as if it has an infinitely long chamber length, the properties of the flow behind the projectile can be solved analytically. This allows the projectile velocity as a function of its position to be solved analytically. Figure 2–12 compares the projectile velocity as a function of position in the solver to the analytical formulation for an infinite chamber length constant area PPIG. As can be seen, the solver matches the analytical results.

The velocity profile of the projectile can no longer be determined analytically if the launch tube length of a PPIG is extended to the point where the first expansion wave catches up to the projectile. The performance of a finite chamber length PPIG must be determined computationally. Nonetheless, by non-dimensionalising the position and velocity of the projectile, it is possible to readily compare simulation results from different internal ballistics solvers. Seigel presents a number of computational simulation results for constant area finite chamber length PPIG simulations using a method of characteristics solver [31]. Figure 2–13 shows a comparison between the

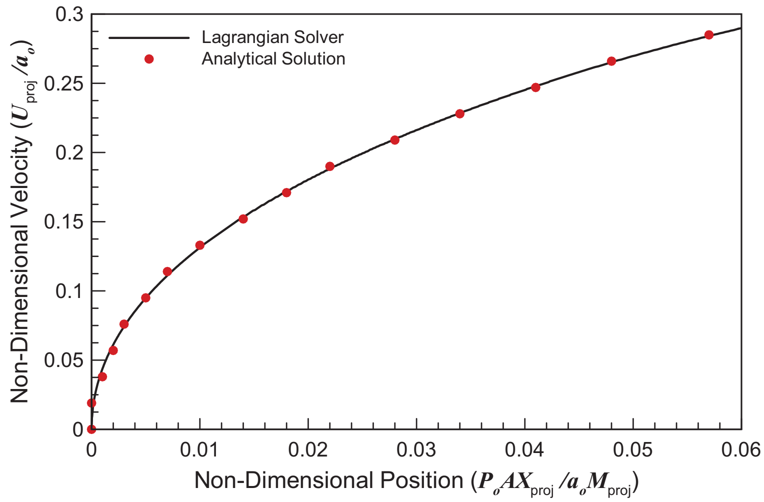

Figure 2–12: Comparison of the Lagrangian solver to the analytical solution for an infinite chamber PPIG

results obtained from the solver presented in this work to numerical data presented in Seigel for a constant area PPIG. The Lagrangian gasdynamics solver shows good agreement with the published results.

Often, the diameter of the launcher chamber is greater than its launch tube diameter. Such launchers are referred to as chambered. Chambered launchers cannot be modeled analytically because of the interaction of the expansion waves in the flow with the area change section of the launcher. However, Seigel presents a number of computational simulation results for chambered PPIG simulations [31] which can be used as a validation tool for the solver presented in this work. Chambered launcher simulations are particularly interesting because they also validate the quasi-one-dimensional formulation of the solver. Figure 2–14 shows a comparison between the results obtained from the solver presented in this work to numerical data presented in Seigel for a chambered PPIG. Again, the Lagrangian gasdynamics solver shows good agreement with the published results. It should be noted that the shape of the area change section (sharp or tapered), which is often overlooked when presenting

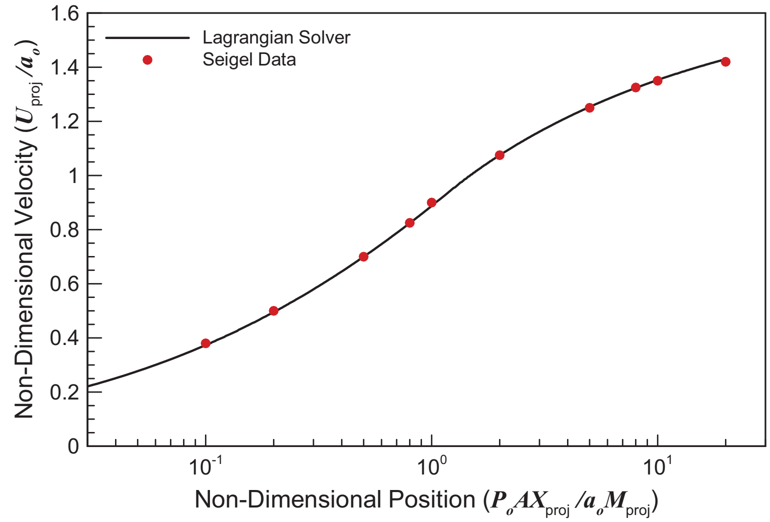

Figure 2–13: Comparison of the Lagrangian solver to published computational solutions for a constant area PPIG

chambered PPIG simulation results, was found to have a negligible effect on the results.

The final step in the validation of the internal ballistics model was to compare the solver presented in this work to another computational gasdynamics solver for a full implosion-driven launcher simulation. An Eulerian gasdynamics solver which was developed by N. F. Ponchaut and adapted to perform implosion launcher simulations [34] was used for this purpose. The results of the comparison can be seen in Figure 2–15, which shows that both simulations match quite closely.

It is good practice to perform a convergence study on the problem being studied by a computational simulation to ensure that the solver is functioning as expected and that sufficient cell resolution is used such that the results are not affected by the mesh resolution. Figure 2–16 and 2–17 show a convergence study performed on a typical launcher. The total number of cells in the domain was varied from 50 cells to 3200 cells. Figure 2–16 presents the final projectile velocity as a function of the log of cell count. A converging problem should show an increasingly small change is

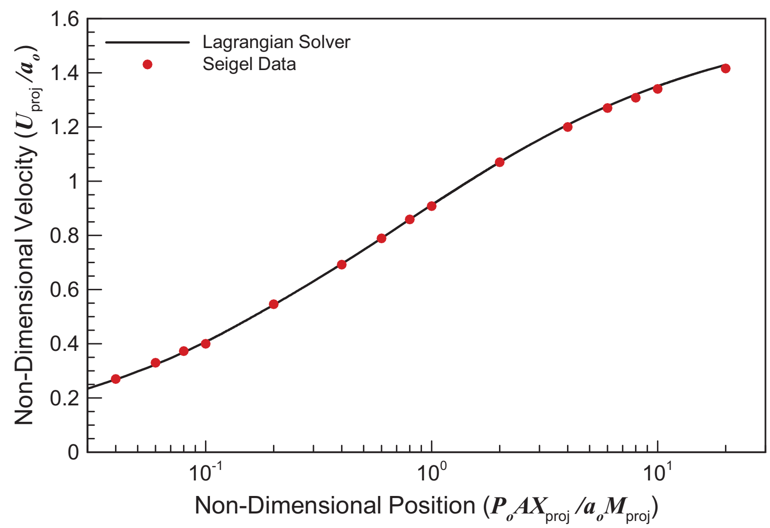

Figure 2–14: Comparison of the Lagrangian solver to published computational solutions for a chambered PPIG

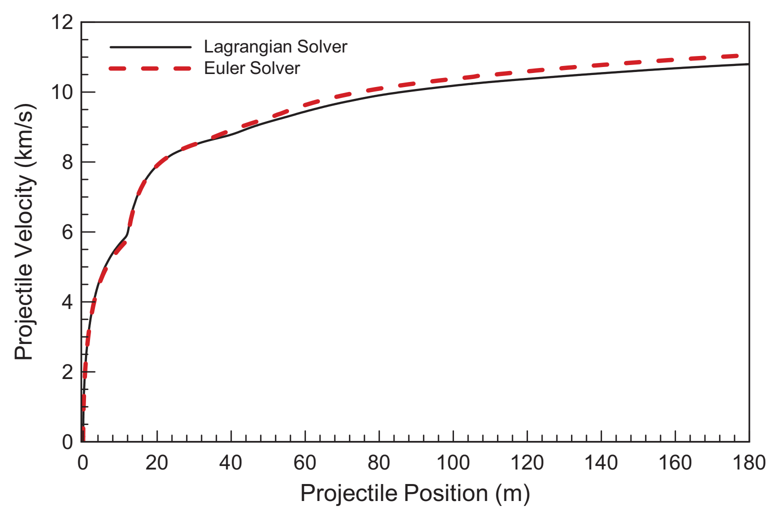

Figure 2–15: Comparison of the Lagrangian solver to an Eulerian gasdynamics solver for a complete implosion-driven launcher simulation

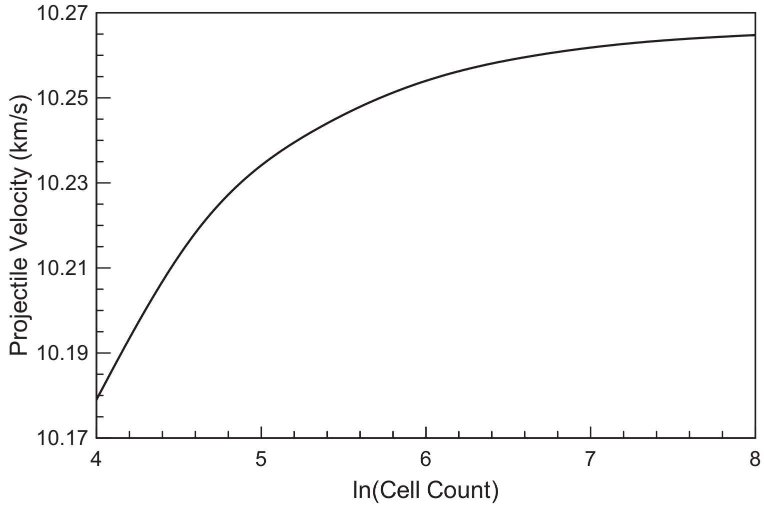

Figure 2–16: Convergence study performed on a typical implosion-driven launcher simulation

velocity as cell count is doubled, which is the case. Figure 2–17 shows the difference in projectile velocity between simulations at the current cell count versus that at the maximum cell count. As can be seen, even at 200 cells the velocity difference between the final projectile velocities is less than 40 m/s (<0.4%). For this reason, simulations in this study use a cell count of 300.

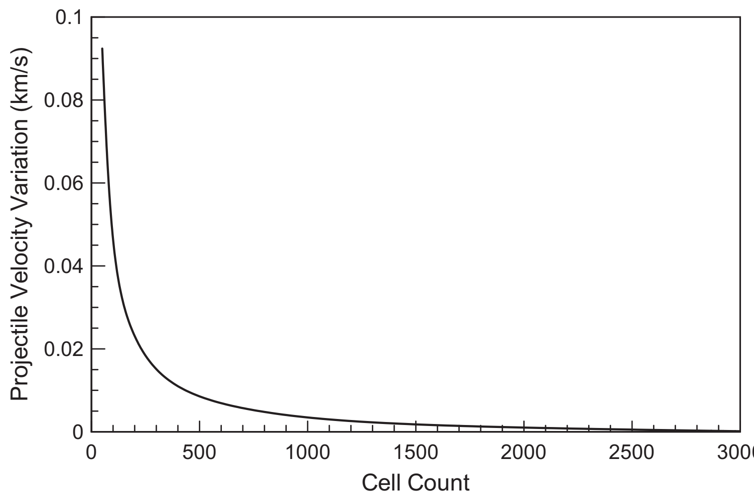

Figure 2–17: Convergence study performed on a typical implosion-driven launcher simulation

CHAPTER 3
Modeling of Non-Ideal Effect in an Implosion-Driven Launcher

The gasdynamics solver presented in Chapter 2 can easily be adapted to modeling an ideal implosion-driven launcher by implementing the appropriate boundary conditions. A typical profile of the predicted projectile velocity as a function of position as it is accelerated down the launch tube is shown in Figure 3–1, along with the corresponding experimental velocity (measured by a high speed camera after the projectile exits the launch tube). As can be seen, the predicted velocity is approximately 60 percent of that predicted by the ideal solver. The cause of this discrepancy is related to non-ideal effects in the launch cycle due to the high temperature and pressure of the driver gas. Experimental velocities are typically anywhere between 45 to 70 percent of the velocity predicted by the ideal solver, depending on the design of the launcher. As a result, the non-ideal effects in the launcher operation will need to be incorporated into the computational model in order to develop a predictive design tool that is capable of properly modeling the effect of varying the design parameters of the launcher.

It is important to keep in mind the goals of the internal ballistics model in order to focus development efforts on the aspects of the model that are most relevant. The internal ballistics solver is being developed first and foremost as an engineering design tool, which can help in the development of implosion driven launchers. Admittedly, in order to completely simulate the implosion driven launcher, one would at the very least need a two-dimensional axisymmetric solver capable of modeling fluid-structure interaction, high strain rate materials behavior, gasdynamic behavior, heat transfer,

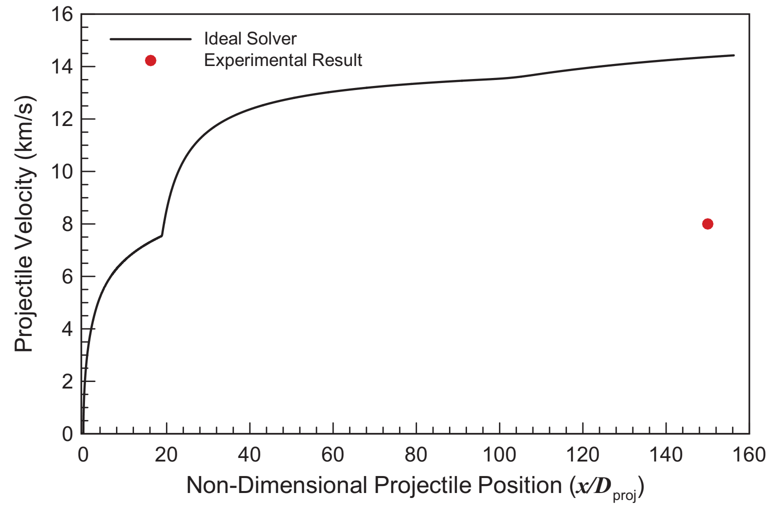

Figure 3–1: Comparison of the predicted velocity for an ideal implosion launcher simulation and the corresponding experimental result. The launcher dimensions are: $D_{LT} = 5$ mm, $D_D = \sqrt{5}D_{LT}$, $L_D = 37D_D$, $U_D = 7$ km/s, Gas = 4MPa He, $L_R = 0.10L_D$, $L_{\text{offset}} = 3D_{LT}$, Proj = $0.5(L/D)$ ZK60

as well as the detonation of condensed phase explosive. Although such solvers do exist, they are not transparent in revealing the modeling assumptions they are built upon. As a result, a user must be familiar with the inner working of the solver in order to have confidence in the validity of the results. The difficulties involved in using these solvers combined with the long simulation run times mean that they are not the best option for an engineering design tool.

The goal of the current modeling effort is to capture the essential behavior of the implosion launcher in a simple quasi-one-dimensional gasdynamics solver that is capable of running multiple simulations per hour on a desktop computer. This will be done by adapting the ideal internal ballistic solver developed in Chapter 2 to simulate the key non-ideal effects in the implosion launcher, resulting in a simple computational model that will help the user understand the impact of the dominant non-ideal effects on the launch cycle. Furthermore, this model will be instrumental in understanding the internal ballistics design considerations of the launcher and in timing velocity augmentation techniques which rely on knowledge of the projectile acceleration profile.

This section will outline the main non-ideal effects in the implosion-driven launcher and present strategies for adapting the internal ballistics model to simulate these effects. Particular attention will be given to phenomenon affecting launcher performance early in the launch cycle, where the majority of the projectile acceleration occurs. Care will be taken to outline the current shortcomings of the model and recommend the path to be taken for future modeling work.

3.1 Reservoir Expansion

The pressure and temperature losses caused by the expansion of the reservoir and launch tube of the implosion driven launcher have an important effect on its performance. The pressure of the stagnated driver gas in the reservoir is more than an order of magnitude greater than the yield strength of the reservoir material. The magnitude and speed of reservoir expansion is sufficient to drastically lower the projectile driving pressure early in the launch cycle and limit the maximum attainable velocity of a single-stage implosion-driven launcher. The driver gas pressures are strong enough that the reservoir material cannot be assumed to be a single incompressible mass that moves uniformly. A dynamic structural model that is capable of simulating the stress wave dynamics is needed to determine the radial velocity and position history of the reservoir walls. These computational models are known as hydrocodes, a term that stems from the fact that early solvers treated materials purely hydrodynamically (only pressure forces, no strength). Although modern solvers do model material strength effects, the term hydrocode remains synonymous with high strain rate structural dynamics solvers.

In order to completely capture radial expansion along the entire axial length of the launcher, one would need to develop a two-dimensional axisymmetric hydrocode. However, the modeling effort can be greatly simplified by dissecting the launcher reservoir into a series of axial slices and computing the radial expansion of each slice independently. This way, a series of one-dimensional radial hydrocodes can be used to model the reservoir expansion. This approach is much less computationally intensive than a complete two-dimensional axisymmetric simulation. Admittedly, the assumption that there is no axial coupling to the slices may not allow the model to accurately predict the internal reservoir profile. However, it is important to remember that the goal of the model is to capture the effect of radial expansion on projectile acceleration, which should be accomplished as long as the timescale of the reservoir expansion is properly simulated.

3.1.1 Modeling Approach

Figure 3–2 shows a schematic of the numerical model. As can be seen, the internal profile of the reservoir is made up of a series of axial locations where radial hydrocode simulations are performed. The driver and the end of the launch tube are assumed to operate rigidly. As can be seen, the radial profile (wall thickness) of each hydrocode location depends on the dimensions of the launcher. The launcher internal wall profile for the quasi-one dimensional internal ballistics solver is obtained by interpolating between the inner radii of the radial hydrocodes. Before calculating the specific volume (v^{n+1}) of the cells in the internal ballistics solver (depends on the radius of the cell), the hydrocode solver is used to determine the expansion of each cell over the current timestep. The resulting internal radii of the axial slices are then used to calculate the radius and specific volume of each cell in the internal ballistics solver.

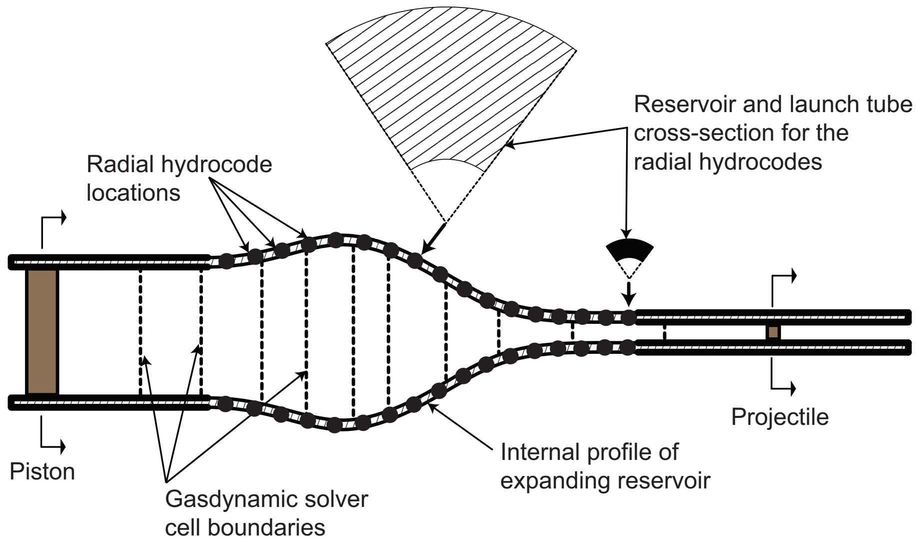

Figure 3–2: Schematic of the approach used to simulate the expansion of the launcher walls in the internal ballistics solver

The driver gas pressure from the internal ballistics solver is used as the boundary condition for the numerical cell at the inner wall of the radial hydrocodes. There are typically a number of gasdynamic cells between each axial location. The pressure on the inner wall is determined by taking the average from all the gasdynamic cells acting within the boundaries of each axial location using the cell positions (X^n) and pressures (p^n) at the beginning of the current timestep.

3.1.2 One-Dimensional Radial Hydrocode

This section will describe the development of the one-dimensional radial hydrocode needed to simulate reservoir expansion, including the implementation of the solid equation of state, the material strength model, as well as the effect of strength and the cylindrical geometry on the finite difference equations. The hydrocode uses the same numerical scheme as the gasdynamics solver presented in Chapter 2. For the sake of brevity, this section will only present a brief overview of hydrocode concepts. In order to gain a more complete understanding of the fundamental concepts, the reader is directed to the textbook by Wilkins [40].

3.1.2.1 Cylindrical Geometry

In order to model the radial expansion of a reservoir slice, the slice must be divided into a number of cylindrical cells. Therefore, the numerical scheme in Section 2.2, which is written for a quasi-one dimensional planar geometry, must be adapted to a one-dimensional cylindrical geometry. This requires slight modifications to the equation for the cell boundary velocity (conservation of momentum) and the equation for the specific volume of the cell. Since the axial length (thickness) of the radial slice is constant, the cell mass will be defined using the radius of the cell to obtain a linear density (kg/m). The cell boundaries will be written in terms of their radius (r).

$$m_{j-1/2} = \frac{\pi}{v_{j-1/2}^{n=1}}((r_j^{n=1})^2 - (r_{j-1}^{n=1})^2) \tag{3.1}$$

The conservation of momentum is defined below. As can be seen, the cross sectional area over which the pressure force acts is defined by the radius of the cell:

$$U_j^{n+1/2} = U_j^{n-1/2} - \frac{\Delta t^{n-1} + \Delta t^n}{m_{j-1/2} + m_{j+1/2}}[(p_{j+1/2}^n + q_{j+1/2}^n) - (p_{j-1/2}^n + q_{j-1/2}^n)]2\pi r_j^n \tag{3.2}$$

The specific volume of the cell can be written as:

$$v_{j-1/2}^{n+1} = \frac{\pi((r_j^{n+1})^2 - (r_{j-1}^{n+1})^2)}{m_{j-1/2}} \tag{3.3}$$

The calculations for the cell position, artificial viscosity, internal energy, and pressure are not affected by the cylindrical geometry.

3.1.2.2 Equation of State

The relatively large pressures applied to the launcher walls are sufficient to compress the reservoir material and appreciably increase its internal energy. The hydrocode requires an equation of state to determine the relation between the pressure, the internal energy, and the specific volume of the material being studied. High pressure solid equation of state formulations are typically empirical, relying on data obtained from flyer plate experiments, in which large pressures are generated by the high speed impact of dense materials. Planar flyer impacts generate a shock wave in the material, behind which the material is in a relatively constant high pressure state. Using diagnostic techniques, one can obtain the particle velocity and shock velocity in the impacted material, which can be used to determine the pressure and specific volume of the material. By varying the velocity of the flyer plate, this experiment can be repeated for a number of pressures, resulting in a curve for the pressure-specific volume relation of the material under shock compression, known as the Hugoniot. The Hugoniot is a single curve in the pressure, specific volume, internal energy space that corresponds to the equilibrium values for a shock compression from room temperature and zero pressure. In general, the loading on the material in the hydrocode will be more complex than a quasi-steady shock compression. Therefore, the equation of state needs to be capable of determining the pressure of the material for any value of specific volume and internal energy. This will require a formulation that extrapolates the Hugoniot to form a surface in the pressure-specific volume-internal energy space. This is shown graphically in Figure 3–3.

The Mie-Gruneisen equation of state formulation is a widely used scheme for obtaining the pressure, specific volume, internal energy relation of a material with a known Hugoniot. The general form of the Mie-Gruneisen equation of state is shown below:

$$p = p_H(v) + (e - e_H(v))\frac{\gamma}{v} \tag{3.4}$$

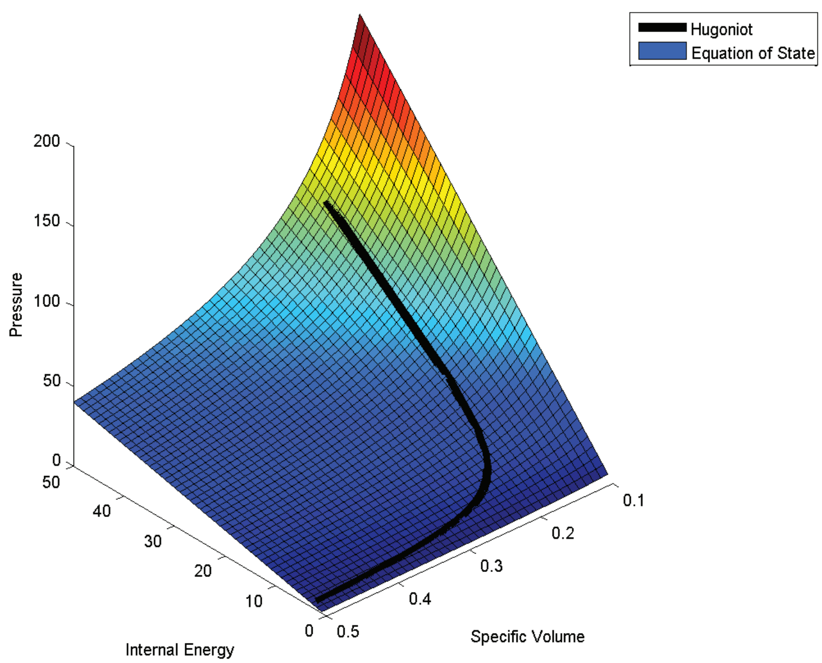

Figure 3–3: Graphical representation of the surface corresponding to the equation of state of a material (pressure-specific volume-internal energy relation). This surface must be obtained using the Hugoniot line generated from shock compression experiments

To find the pressure, one begins with the Hugoniot pressure for the current specific volume ($p_H(v)$). An internal energy correction term is added to compensate for the fact that the specific internal energy of the material (e) is not necessarily equal to the Hugoniot specific internal energy at the current specific volume ($e_H(v)$). The Gruneisen parameter (γ/v) is used to relate this variation in the internal energy to a difference in pressure. The Gruneisen parameter is assumed to be constant, and can be seen as a way to extrapolate the Hugoniot data to the entire internal energy space. In order to obtain the final form of the equation of state, the Hugoniot pressure and internal energy terms are typically replaced by a curve fit obtained from the experimental data. The details of this derivation are given by Wilkins [40]. The final form of the equation of state and the material constants for steel are given below. As can be seen, the equation of state still resembles the original form presented in Equation 3.4, with a specific volume term and a correction term for internal energy. It should be noted that the equation of state given below uses the relative specific volume of the material, which is equal to the current specific volume divided by the specific volume at zero pressure (v/v_o). The equation also requires that the internal energy in the form of energy per original volume (Mbar).

$$p = k_1(1 - v/v_o) + k_2(1 - v/v_o)^2 + k_3(1 - v/v_o)^3 + \gamma_o e \tag{3.5}$$

$k_1 = 1.648$ Mbar

for $(1 - v/v_o) \geq 0$

$k_2 = 3.124$ Mbar

for $(1 - v/v_o) < 0$

$k_2 = 0$

$k_3 = 5.649$ Mbar

$\gamma_o = 2.17$

The equation of state can also be used to obtain the speed of sound of the material, by taking the derivative of pressure with respect to density and internal energy, as shown below:

$$a^2 = \left(\frac{\partial p}{\partial \rho}\right)_{s=\text{const}} \tag{3.6}$$

$$a^2 = \left(\frac{\partial p}{\partial \rho}\right)_{e=\text{const}} + \frac{p}{\rho^2}\left(\frac{\partial p}{\partial e}\right)_{\rho=\text{const}} \tag{3.7}$$

$$\left(\frac{\partial p}{\partial \rho}\right)_{e=\text{const}} = k_1\frac{\rho_o}{\rho^2} + 2k_2\left(1 - \frac{\rho_o}{\rho}\right)\left(\frac{\rho_o}{\rho^2}\right) + 3k_3\left(1 - \frac{\rho_o}{\rho}\right)^2\left(\frac{\rho_o}{\rho^2}\right) \tag{3.8}$$

$$\left(\frac{\partial p}{\partial e}\right)_{\rho=\text{const}} = \gamma_o \tag{3.9}$$

The speed of sound of the material is needed in order to determine the next timestep size (see Section 2.2). It should be noted that when the pressures are relatively small (< 10 GPa), there is little variation in the speed of sound of steel, and one can simply use the bulk speed of sound (4.6 km/s) to determine the timestep size.

3.1.2.3 Material Strength Effects

In order to properly model the dynamic behavior of materials, the hydrocode must be able to take into account the effect of material strength. The large pressures encountered in dynamic materials modeling lead to significant plastic deformation. Therefore, the model will need to properly simulate the elastic-plastic behavior of the material. This section will outline the basic procedure for modeling the resistance of a material to deformation in a hydrocode. The material will be assumed to be isotropic (uniform strength and stiffness properties). The axis will be defined as 1 being the radial direction, 2 the circumferential direction, and 3 the axial direction.

A basic elastic-plastic model will be used, in which the stress-strain behavior of a material is determined by Hooke's law (elastic deformation) until the yield stress is reached, at which point it will flow plastically. During plastic flow, the stress in the material is determined by the local yield stress of the material. As will be seen, constitutive models can be used to determine the local variation in yield stress as a function of strain, strain rate, pressure, and temperature. Plastic flow is a dissipative process that results in permanent material deformation. As the material is unloaded, only the elastic deformation is recovered. In general the material model needs to calculate the stress as a function of strain (Hooke's law), the onset of yielding (von Mises yield criterion), and the variation in yield stress due to strain, strain rate, pressure, and temperature (constitutive model).

In a hydrocode, the stress state in the numerical cell must be calculated from the strain at the cell boundaries. The stress state in the cell is initially calculated using Hooke's law, thus assuming the deformation is entirely elastic. If the resulting stress state is beyond the yield strength, it is corrected to correspond to the yield strength, allowing the material to flow plastically. Hooke's law can be written for the rate of change in the principal stresses (σ) as a function of the rate of change in the strain (ϵ) and volume (V) using the shear modulus (G) and the bulk modulus (K) of the material.

$$\dot{\sigma_1} = \left(K - \frac{2}{3}G\right)\frac{\dot{V}}{V} + 2G\dot{\epsilon_1} \tag{3.10}$$

$$\dot{\sigma_2} = \left(K - \frac{2}{3}G\right)\frac{\dot{V}}{V} + 2G\dot{\epsilon_2} \tag{3.11}$$

$$\dot{\sigma_3} = \left(K - \frac{2}{3}G\right)\frac{\dot{V}}{V} + 2G\dot{\epsilon_3} \tag{3.12}$$

The principal stresses can be written as a combination of the hydrostatic pressure (P) (leads to volume distortion) and the deviatoric stress (s) (leads to shape (shear) distortion):

$$\dot{\sigma_1} = \dot{P} + \dot{s_1} \tag{3.13}$$

$$\dot{\sigma_2} = \dot{P} + \dot{s_2} \tag{3.14}$$

$$\dot{\sigma_3} = \dot{P} + \dot{s_3} \tag{3.15}$$

As will be seen, the yield criterion depends on the magnitude of the deviatoric stresses. Combining the previous equations and using the definitions of the bulk modulus, hydrostatic stress, and deviatoric stress, an expression for the rate of change in the principle deviatoric stresses can be written as a function of the rate of change of strain and volume:

$$\dot{P} = \frac{-\dot{V}}{V}K \tag{3.16}$$

$$\dot{P} = \frac{-1}{3}(\dot{\sigma_1} + \dot{\sigma_2} + \dot{\sigma_3}) \tag{3.17}$$

$$\dot{s_1} + \dot{s_2} + \dot{s_3} = 0 \tag{3.18}$$

$$\dot{s_1} = 2G\left(\dot{\epsilon_1} - \frac{1}{3}\frac{\dot{V}}{V}\right) \tag{3.19}$$

$$\dot{s_2} = 2G\left(\dot{\epsilon_2} - \frac{1}{3}\frac{\dot{V}}{V}\right) \tag{3.20}$$

$$\dot{s_3} = -(\dot{s_1} + \dot{s_2}) \tag{3.21}$$

The rate of change of the principal strains within a cell can be obtained directly from the cell boundary position and velocity:

$$(\dot{\epsilon_1})^{n+1/2}_{j-1/2} = \frac{U^{n+1/2}_j - U^{n+1/2}_{j-1}}{r^{n+1/2}_j - r^{n+1/2}_{j-1}} \tag{3.22}$$

$$(\dot{\epsilon_2})^{n+1/2}_{j-1/2} = \frac{U^{n+1/2}_j + U^{n+1/2}_{j-1}}{r^{n+1/2}_j + r^{n+1/2}_{j-1}} \tag{3.23}$$

The rate of change of cell volume can be obtained from the change in the specific volume:

$$(\dot{V})^{n+1/2}_{j-1/2} = \frac{V^{n+1}_{j-1/2} - V^{n}_{j-1/2}}{\Delta t^{n+1/2}} \tag{3.24}$$

Using these expressions, the principal deviatoric stresses can be obtained:

$$(s_1)^{n+1}_{j-1/2} = (s_1)^{n}_{j-1/2} + 2G\left[(\dot{\epsilon_1})^{n+1/2}_{j-1/2}\Delta t^n - \frac{2}{3}\left(\frac{V^{n+1}_{j-1/2} - V^{n}_{j-1/2}}{V^{n+1}_{j-1/2} + V^{n}_{j-1/2}}\right)\right] \tag{3.25}$$

$$(s_2)^{n+1}_{j-1/2} = (s_2)^{n}_{j-1/2} + 2G\left[(\dot{\epsilon_2})^{n+1/2}_{j-1/2}\Delta t^n - \frac{2}{3}\left(\frac{V^{n+1}_{j-1/2} - V^{n}_{j-1/2}}{V^{n+1}_{j-1/2} + V^{n}_{j-1/2}}\right)\right] \tag{3.26}$$

$$(s_3)^{n+1}_{j-1/2} = -\left[(s_1)^{n}_{j-1/2} + (s_2)^{n}_{j-1/2}\right] \tag{3.27}$$

As can be seen, Hook's law can be used to find the principal deviatoric stresses as a function of the velocity and radius of the cell boundary, as well as the specific volume of the cell. Only the shear modulus (G=0.77 Mbar for mild steel) of the material is required. It is important to remember that the expressions for the principal deviatoric stresses assume that the material is within the elastic deformation region. The von Mises yield criterion can be used to verify whether the equivalent stress in the material is greater than its yield stress (Y_o). If this is the case, the values of deviatoric stress must be corrected to correspond to the local yield stress, allowing the material to deform plastically.

IF

$$\sqrt{\frac{3}{2}(s_1^2 + s_2^2 + s_3^2)} = \sigma_{eq}^* \geq Y_o \tag{3.28}$$

THEN

$$s_1 = s_1 \frac{Y_o}{\sigma_{eq}^*} \tag{3.29}$$

$$s_2 = s_2 \frac{Y_o}{\sigma_{eq}^*} \tag{3.30}$$

$$s_3 = s_3 \frac{Y_o}{\sigma_{eq}^*} \tag{3.31}$$

A number of different constitutive models can be used to determine the value of the local yield stress. The elastic plastic model is the most basic. It relies on the assumption that the yield stress remains constant at the tensile yield strength of the material. In a real material, the yield stress will not be constant and its variation must be determined using a constitutive model. Two commonly used constitutive models are given below. The first is the Johnson-Cook model [20], which takes into account the effect of strain hardening, strain rate strengthening, as well as weakening from an increase in material temperature (T). The second expression is the Steinberg-Guinan model, which takes into account strain hardening, pressure (p) and specific volume (v) effects, as well as weakening from an increase in temperature. Although both constitutive models are equally appropriate for studying reservoir expansion, the hydrocode simulations in this work use the Steinberg-Guinan constitutive model. The constitutive models and the material constants for mild steel are given below:

Johnson-Cook

$$Y_o = [A + B(\sigma_{eq}^p)^N][1 + C \ln \frac{\dot{\epsilon}_2}{\dot{\epsilon}_o}][1 - \left(\frac{T - 300}{T_m - 300}\right)^M] \tag{3.32}$$

A=286 MPa

B=500 MPa

C=0.017

N=0.228

M=0.917

Tm=1930

$\dot{\epsilon}_o$=1 s^{-1}

Steinberg-Guinan

$$Y_o = [A(1 + B(\sigma_{eq}^p)^N][1 + Cp\left(\frac{v}{v_o}\right)^{1/3} - h(T - 300)] \tag{3.33}$$

IF $T > Tm$, $Y_o = 0$

IF $[A(1 + B(\sigma_{eq}^p)^N] > 0.02$ Mbar, $Y_o = 0.02[1 + Cp\left(\frac{v}{v_o}\right)^{1/3} - h(T - 300)]$

A=0.00340 Mbar

B=40

C=3 Mbar^{-1}

N=0.35

Tm=1930

h=0.00045

Expressions are required to obtain the plastic strain and the temperature of the material for the constitutive model. The temperature of the material is found using the internal energy and the Mie-Gruneisen equation of state. The total plastic strain (ϵ^p_{eq}) cannot be calculated directly. For this reason, the incremental increase in plastic strain must be calculated at every timestep. This can be done using the difference between the equivalent stress predicted by Hooke's law and the corrected equivalent stress. The material constants required for the temperature and plastic strain calculations have been included for mild steel.

Temperature

$$T_{j-1/2} = \frac{e_{j-1/2}v_o - \epsilon_o}{3R} \tag{3.34}$$

$$\epsilon_o = \epsilon_{oo} + \epsilon_{o1}(1 - v/v_o) + \epsilon_{o2}(1 - v/v_o)^2 + +\epsilon_{o3}(1 - v/v_o)^3 + +\epsilon_{o4}(1 - v/v_o)^4 \tag{3.35}$$

ϵ_{oo}=-0.00134 (10^8m^2/s^2)

ϵ_{o1}=-0.002908 (10^8m^2/s^2)

ϵ_{o2}=0.1012 (10^8m^2/s^2)

ϵ_{o3}=0.2051 (10^8m^2/s^2)

ϵ_{o4}=0.2901 (10^8m^2/s^2)

R=1.489(10^{-6}) (10^8m^2/s^2)

Plastic Strain

IF $\sigma^*_{eq} > Y_o$

$$\Delta\epsilon^p_{eq} = \left(\frac{\sigma^*_{eq}}{Y_o} - 1\right)\frac{1}{3G}Y_o \tag{3.36}$$

It should be noted that Wilkins provides a far more detailed description of strength models for hydrocodes, including detailed descriptions of the solid mechanics, a detailed overview of the Steinberg-Guinan constitutive model, and the derivation of the plasticity model used to find the equivalent plastic strain [40]. Now that all the necessary elements to the hydrocode model have been discussed, the original finite difference equations presented in Section 2.2 can be rewritten to incorporate the cylindrical geometry, the Mie-Gruneisen equation of state, and the material strength model. The complete set of finite difference equations for the one-dimensional radial hydrocode can be found in Appendix C.

3.1.2.4 Launcher Simulations with Reservoir Expansion

Figures 3–4 and 3–5 compare the projectile velocity and pressure profiles for an implosion launcher simulation with and without the expansion model. The projectile velocity from the corresponding experiment is also shown in the velocity figure. As can be seen, the base pressure on the projectile is significantly lower in the expanding reservoir simulation, leading to a final velocity that is 34 percent less than the ideal velocity. The difference between the final projectile velocity and the experiment is of 6.4 km/s with the ideal simulation, but has been reduced to 1.5 km/s in the expanding reservoir simulation. The operation of the reservoir expansion model can be seen in Figure 3–6, which shows the progressive swelling of the reservoir. As can be seen, significant radial expansion of the reservoir occurs very early in the launch cycle.

3.2 Non-Ideal Driver Effects

The non-ideal behavior of the linear explosive driver was described in detail in the Introduction (Section 1.3.1). Four main non-ideal effects were noted to cause significant differences between ideal predictions and the real performance of drivers:

1. The finite time required for the shock wave to emerge ahead of the detonation wave, referred to as the shock formation (or breakout) distance and measured to be 10.5 diameters.
2. The initial overdriving of the precursor shock wave due to the jetting of driver tube material.

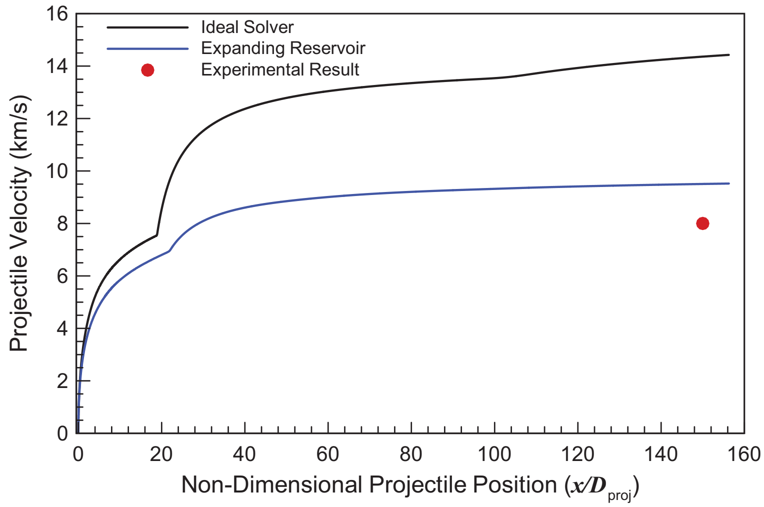

Figure 3–4: Comparison of the projectile velocity profile for a launcher simulation with reservoir expansion to an ideal simulation. The launcher dimensions are: $D_{LT} =$ 5 mm, $D_D = \sqrt{5}D_{LT}$, $L_D = 37D_D$, $U_D = 7$ km/s, Gas = 4MPa He, $L_R = 0.10L_D$, $L_{\text{offset}} = 3D_{LT}$, Proj = 0.5$(L/D)$ ZK60

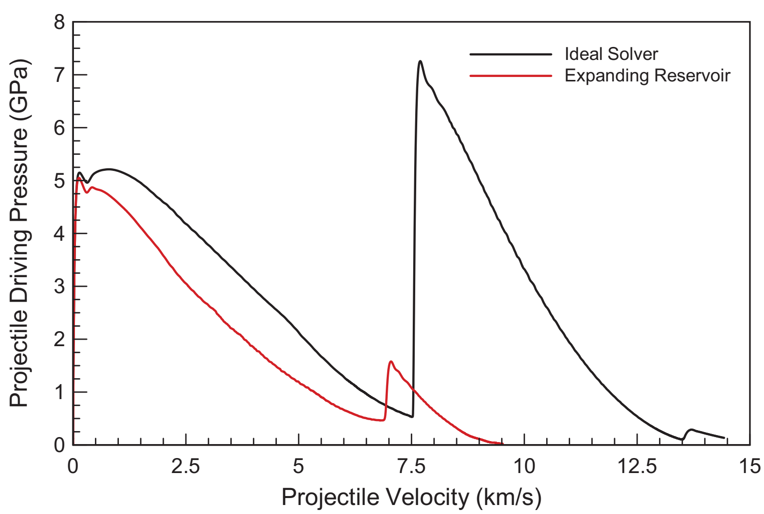

Figure 3–5: Comparison of the projectile driving pressure variation for a launcher simulation with reservoir expansion to an ideal simulation. The launcher dimensions are: $D_{LT} = 5$ mm, $D_D = \sqrt{5}D_{LT}$, $L_D = 37D_D$, $U_D = 7$ km/s, Gas = 4MPa He, $L_R = 0.10L_D$, $L_{\text{offset}} = 3D_{LT}$, Proj = 0.5$(L/D)$ ZK60

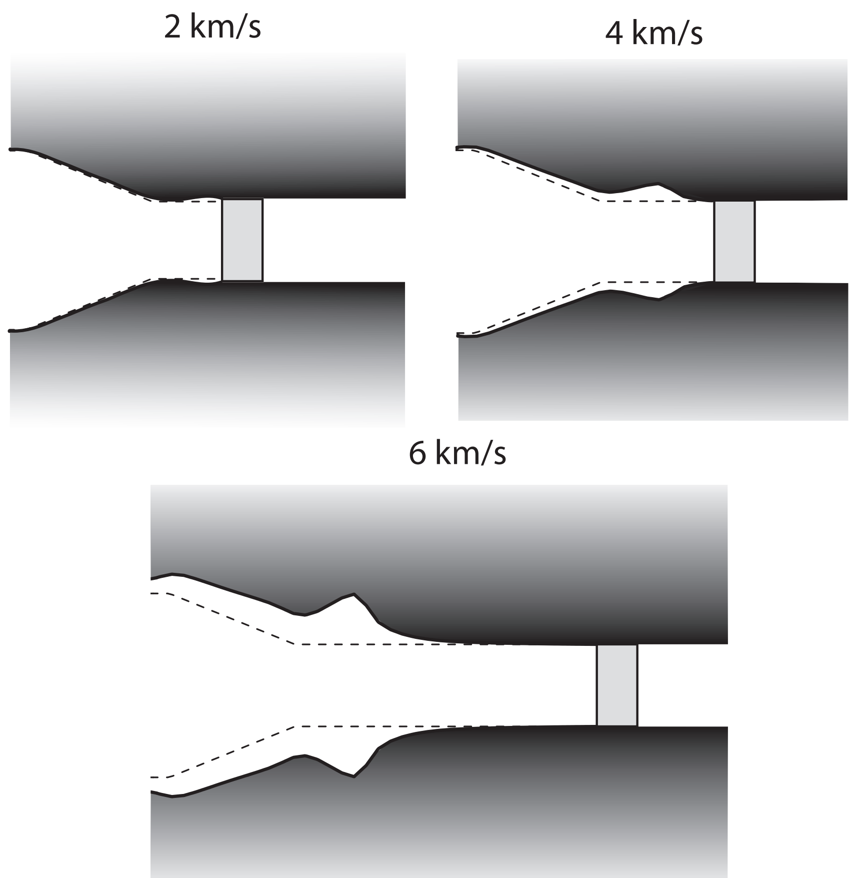

Figure 3–6: Schematic demonstrating the predicted reservoir radial expansion in a typical implosion launcher at the time when the projectile has reached 2, 4, and 6 km/s. The original reservoir profile is shown in the dashed line. A 5:1 scaling has been used to emphasize the radial dimension.

3. The loss of driver gas through the explosively driven piston due to the growth of a boundary layer in the shocked driver gas.
4. The radial expansion of the driver tube between the precursor shock wave and the explosive pinch due to the elevated driver gas pressures.

Boundary layer and expansion effects cause a decay in the precursor shock wave velocity. As a result, the pressure, speed of sound, and particle velocity in longer drivers will be significantly lower than the values predicted by ideal calculations. Furthermore, the shock wave formation distance and the loss of driver gas through the explosively driven pinch reduce the mass of driver gas available to accelerate the projectile. It is important that these effects be modeled by the internal ballistics solver in order to understand the effect of varying the driver length on the performance of the launcher.

The one-dimensional internal ballistics solver is not capable of directly simulating the driver non-ideal effects (simulating boundary layer growth, jetting, and shock wave formation would require a 2-D solver). However, it is possible to use an empirical model based on experimental driver data to simulate the loss of driver gas through the explosively driven piston and the decay of the precursor shock wave velocity. This section will describe the model which has been formulated to simulate non-ideal driver effects in the internal ballistics solver.

The non-ideal driver model will simulate the driver gas loss through the explosively driven pinch and the resulting precursor shock wave velocity decay by applying a mass loss term to the cell adjacent to the piston of the internal ballistics solver. The rate of mass loss at the piston will be chosen such that the computational precursor shock wave trajectory matches the experimental results. This will allow the model to simulate the combined effects of precursor shock wave formation distance, overdriving from the diffuse metal jet, boundary layer gas loss, and driver tube expansion.

During driver experiments, the trajectory (position versus time) of the detonation front (piston location) and the precursor shock wave is recorded at a number of locations along the driver. As was shown in Figure 1–11, this data can be used to generate a plot of non-dimensional shock wave velocity, and non-dimensional standoff (distance between the shock wave and the piston), as a function of non-dimensional piston position. By non-dimensionalizing the shock velocity by the ideal shock velocity, and the position and standoff by the diameter of the driver, the analysis can be made to apply to drivers of having different sizes and explosive velocities.

In order to implement the non-ideal driver model, the data for the precursor shock wave velocity decay as a function of piston position must be used to determine the mass loss that must be applied to the numerical cell at the piston face as a function of the position of the piston. The first step is to find an expression which relates the rate of mass loss to the non-dimensional precursor shock wave velocity. This can be accomplished using a quasi-steady system, where a leaky piston with a constant rate of driver gas loss ($\dot{m}_{\text{out}}$) is travelling at a constant velocity (U_{piston}) into a quiescent gas. In this system, the particle velocity (U_1) between the piston and the precursor shock wave will be constant. As a result of the mass loss, the particle velocity and the precursor shock wave velocity will be lower than in an ideal system. A closed form solution relating the mass flow rate of gas loss, the piston velocity, and the particle velocity can readily be obtained using the conservation of mass:

$$\dot{m}_{\text{out}} = \frac{\pi D^2}{4}\rho_1(U_{\text{piston}} - U_1) \tag{3.37}$$

A series of simplifying assumptions can be made to this expression. First, for strong shock waves, the density ratio is insensitive to small variations in the shock strength. Therefore, we will take the density of the shocked gas (ρ_1) to be constant, and held at the ideal shocked gas density. Second, in the strong shock limit, the ratio of particle velocity over piston velocity is equal to the ratio of shock velocity (U_s) to ideal shock velocity. Using these simplifications, an expression directly relating the mass flow rate of driver gas loss and the non-dimensional precursor shock wave velocity can be obtained:

$$\dot{m}_{\text{out}} = \frac{\pi D^2}{4} \rho_{1_{\text{ideal}}} U_{\text{piston}} \left(1 - \frac{U_s}{U_{s_{\text{ideal}}}}\right) \tag{3.38}$$

In order to determine the mass flow rate of gas loss as a function of piston position that will reproduce the experimental shock trajectory, the communication time (t_{com}) between the piston and the shock wave must be taken into account. The communication time is determined by the standoff between the precursor shock wave and the piston ($X_s - X_{\text{piston}}$), as well as the wave propagation velocity (particle velocity plus speed of sound a_1) in the driver gas, as is illustrated by Figure (3–7).

$$(a_1 + U_1)t_{\text{com}} - U_{\text{piston}} t_{\text{com}} = X_s - X_{\text{piston}} \tag{3.39}$$

$$t_{\text{com}} = \frac{X_s - X_{\text{piston}}}{a_1 + U_1 - U_{\text{piston}}} \tag{3.40}$$

The communication time is not easily obtained since the particle velocity and speed of sound decay as the shock wave decays (U_1 and a_1 are not constant). In order to simplify the calculation, it will be assumed that the speed of sound and particle velocity remain constant and correspond to those behind a shock wave of ideal strength. The expression for the communication time becomes:

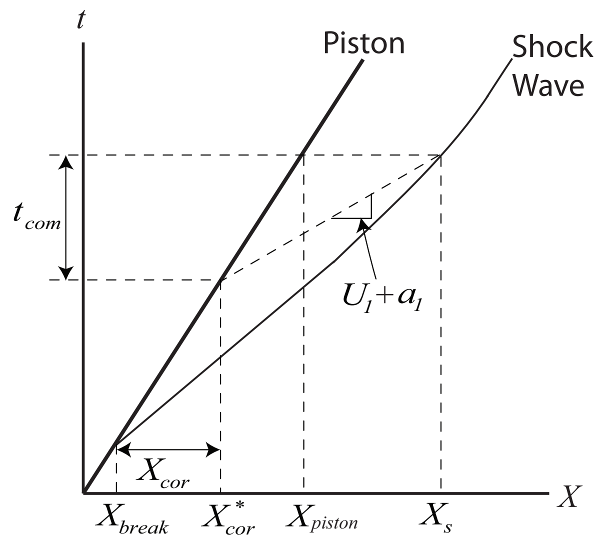

Figure 3–7: Schematic of the X-t diagram of a non-ideal driver. The effect of the communication time between the piston and the shock wave on the analysis is shown.

$$t_{\text{com}} = \frac{X_s - X_{\text{piston}}}{a_{1_{\text{ideal}}}} \tag{3.41}$$

Using the communication time, we can now determine the piston position (X^*_{cor}) along the driver where the mass flow rate corresponding to the precursor shock wave velocity at X_s (see Figure (3–7)):

$$X^*_{\text{cor}} = X_{\text{piston}} - U_{\text{piston}} t_{\text{com}} \tag{3.42}$$

A final correction must be made for the fact that the shock only emerges from the explosive-driven piston after a number of driver tube diameters. In order to compensate for this shock breakout distance, the first experimental data point is used to estimate the location where the shock wave first emerged past the detonation. Knowing the position of the shock wave (X_{s_1})and the explosive-driven piston (X_{piston_1}) at the first data point, and assuming that the initial shock wave velocity is equal to the ideal shock velocity, the following expression for shock breakout distance (X_{break}) can be obtained:

$$X_{\text{break}} = X_{s_1} - U_{s_{\text{ideal}}} \left(\frac{X_{s_1} - X_{piston_1}}{U_{s_{\text{ideal}}} - U_{\text{piston}}} \right) \tag{3.43}$$

When simulating a driver using the internal ballistics model, the breakout distance will need to be subtracted from the length of the driver. In order to adjust the correlation between the piston position and the mass flow rate of gas loss, the breakout distance is subtracted from the corrected piston position determined above (see Figure (3–7)):

$$X_{\text{cor}} = X_{\text{piston}} - U_{\text{piston}} t_{\text{com}} - X_{\text{break}} \tag{3.44}$$

In order to implement the non-ideal driver model in the internal ballistic simulation, the experimental data can be plotted in the form shown in Figure 3–8, relating the non-dimensional shock velocity ($\frac{U_s}{U_{s_{\text{ideal}}}}$) and the non-dimensional explosive-driven piston position where the corresponding mass flow rate must be applied ($\frac{X_{\text{cor}}}{D}$). The data plotted in this non-dimensional form can be used for drivers having different diameters and piston velocities. The data was obtained from a 1.27 cm diameter, 0.09 cm wall thickness driver filled with 2 MPa of helium. The driver tube was surrounded by 0.3 cm of nitromethane explosive and a 4.45 cm diameter tamper.

Using the linear curve fit from Figure 3–8, the mass flow rate as a function of the piston position along the driver can be determined using Equation 3.38. In the internal ballistics model, the loss of driver gas during each timestep is calculated using the corresponding mass flow rate and the size of the timestep. This mass loss is applied to the cell adjacent to the piston.

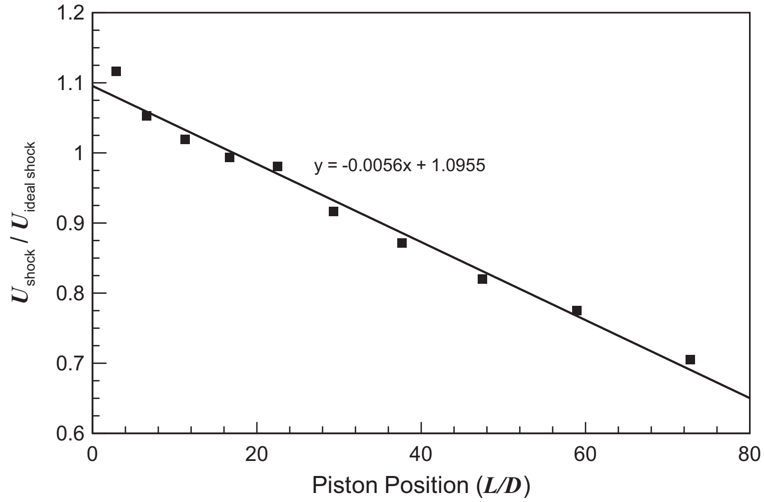

Figure 3–8: Linear curve fit of precursor shock wave velocity as a function of explosively driven piston position used for the non-ideal driver model. The data was obtained from a 1.27 cm diameter driver filled with 2 MPa of helium.

The simulation results for the standoff between the piston and the shock and the shock velocity as a function of shock position along the driver can now be compared to the data used to generate the model. As can be seen in Figure 3–9 and 3–10, the results agree quite nicely, despite a number of simplifying assumptions. As a result, the non-ideal driver model should offer a good representation of real driver operation in launcher simulations.

Projectile velocity profiles from simulations for launchers with ideal and non-ideal drivers with lengths of 40 diameters and 80 diameters are shown in Figure 3–11. It is important to remember that in order to simulate a 40 diameter driver, the length of the driver in the simulation will be 40 diameters minus the shock breakout distance (10.5 diameters), which results in an effective driver length of 29.5 diameters. Both simulations include reservoir expansion. As can be seen, driver losses have a notable effect on performance. Launchers with long drivers are strongly affected by the decay of the shock strength, which results in a much lower initial base pressure. This explains why the initial acceleration of the launcher with an 80 diameter driver is

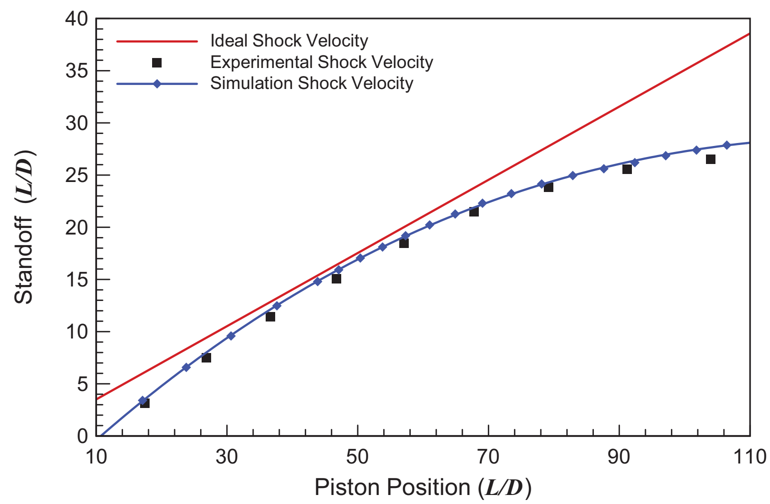

Figure 3–9: Standoff between the precursor shock wave and the explosively driven piston as a function of piston position for the non-ideal driver model and the experimental data used to generate the model

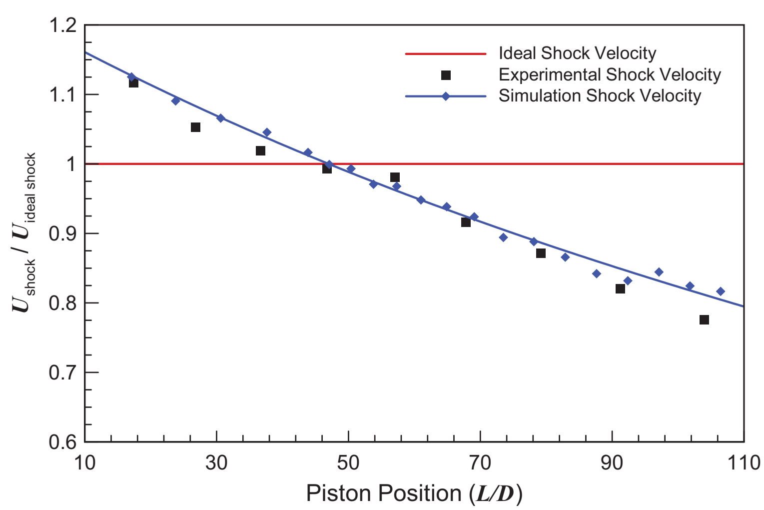

Figure 3–10: Precursor shock wave velocity as a function of piston position for the non-ideal driver model and the experimental data used to generate the model

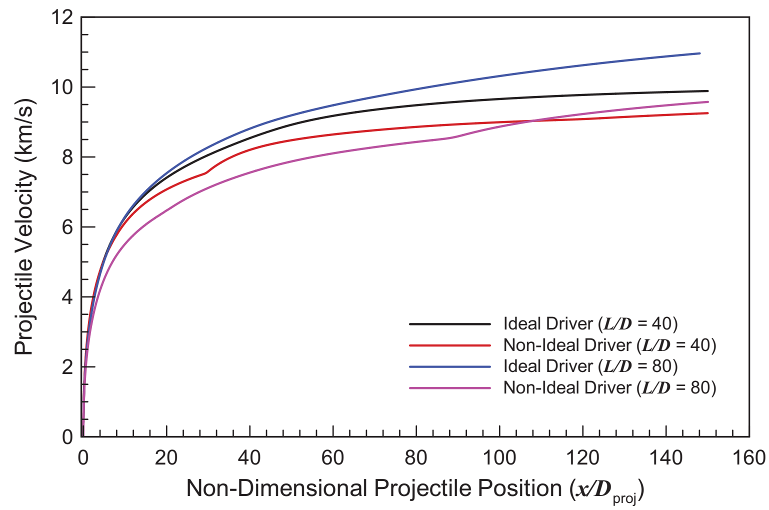

Figure 3–11: Comparison between the projectile velocity profile predicted by simulations using ideal and non-ideal drivers. The simulations include the reservoir expansion model. The launcher dimensions are: $D_{LT} = 5$ mm, $D_D = \sqrt{5}D_{LT}$, $U_D = 7$ km/s, Gas = 4MPa He, $L_R = 0.18L_D$, $L_{\text{offset}} = 3D_{LT}$, Proj = $0.5(L/D)$ ZK60

significantly lower for the non-ideal driver simulation. Although shorter drivers are less affected by shock velocity decay, there is a notable loss of performance when the shock breakout distance is taken into account. The shock breakout distance essentially shortens the volume of the driver by 10.5 diameters, which means that there is less gas available to accelerate the projectile.

It is important to make a final note on the limitations of this model. As with any empirical model, it is only as good as the data from which it is derived. Further, one must be careful when applying the model to drivers having different design parameters to those used to generate the data. Experience has shown that the performance of drivers is relatively constant, despite changes in the geometry of the driver, the explosive-driven piston velocity, and the driver gas fill pressure. Nonetheless, when making significant changes to the driver fill pressure or the detonation velocity of the explosive, or when changing the driver gas, it is recommended that new experiments be performed beforehand, in order to properly model driver non-ideal effects.

3.3 Loss of Driver Gas through Sealing Cone

As the explosive-driven piston reaches the launcher reservoir, a large steel conical section is imploded in an attempt to seal the driver gas in the reservoir. Typically, the explosive seal is not completely effective and leaves a hole through which the driver gas can escape. This can be seen in Figure 3–12, which shows a cross section of the reservoir an implosion-driven launcher after being fired, including a partially imploded sealing cone section. The resulting loss of driver gas through the sealing cone can drastically lower the pressure in the reservoir and significantly degrade the performance of the launcher. This non-ideal effect can readily be modeled by modifying the boundary condition in the simulation from a piston to a free surface as the explosively driven piston reaches the reservoir. Since the internal ballistics solver is quasi-one dimensional, the size of the hole through which gas can escape can also be varied. However, it is difficult to predict to what degree the reservoir will be sealed. Experience during the McGill project has shown that a reservoir seal can vary from nearly complete, to completely ineffective. The design of the sealing cone, as well as internal ballistics parameters such as the propellant fill pressure and the ratio of the reservoir length to the driver length (L_R/L_D) have an important effect on the ability of the sealing cone to contain the driver gas pressures. For this reason, the degree of reservoir sealing cannot be predicted by the quasi-one-dimensional solver.

It remains of interest to use the solver to study the effect of varying the sealing cone opening on the performance of the launcher. Figure 3–13 shows the projectile velocity profile of an implosion driven launcher with three different sealing cone openings. It is important to note that the launcher used in these simulations has

Figure 3–12: Picture of the cross section of an implosion-driven launcher reservoir after being fired. The sealing cone section was not able to completely seal the driver gas.

a relatively short driver (20 diameters). This length was chosen to highlight the influence of gas leakage through the sealing cone. The expanding reservoir and non-ideal driver models were used in the simulation. As can be seen from the figure, the effect of sealing cone leakage is only noticeable very late in the launch cycle. For this reason, it appears to have little effect on performance. As will be seen, the effect becomes even less important for launchers with longer drivers. As expected, the magnitude of the performance loss has a significant dependence on the size of the hole through which gas can escape.

Figure 3–14 compares the velocity deficit for a completely unsealed reservoir as a function of driver length for three different projectile thicknesses. The simulations include reservoir expansion and non-ideal driver effects. As can be seen, decreasing the projectile thickness (or mass) and increasing the driver length both significantly decrease the effect of driver gas leakage. Increasing the mass of a projectile lowers its acceleration and increases the time taken to launch the projectile. This gives more time for expansion waves caused by reservoir gas leakage to affect the projectile base pressure. As a result, heavier projectiles are more influenced by driver gas leakage

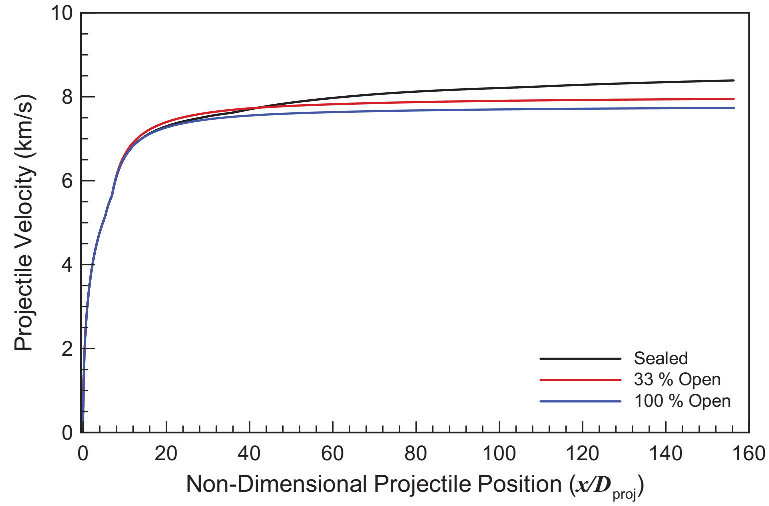

Figure 3–13: Comparison of the projectile velocity profile for different reservoir openings. The simulations include the reservoir expansion model and non-ideal driver effects. The launcher dimensions are: $D_{LT} = 5$ mm, $D_D = \sqrt{5}D_{LT}$, $L_D = 20D_D$, $U_D = 7$ km/s, Gas = 4MPa He, $L_R = 0.18L_D$, $L_{\text{offset}} = 3D_{LT}$, Proj = $0.5(L/D)$ ZK60

through the sealing cone. Conversely, for longer drivers, the offset between the precursor shock wave and the explosively driven piston is larger, which increases the time between when the projectile is set in motion and when the driver gas leakage through the sealing cone begins. A longer driver also provides more driver gas to propel the projectile. For these two reasons, launchers with shorter driver lengths are more influenced by sealing cone losses. For a typical projectile thickness of 0.5 calibers and driver length of 40 diameters, reservoir sealing has very little effect on launcher performance. Given its small effect on launcher performance and the difficulty involved in predicting the size of the hole through which gas can escape, simulations in this work will not include the sealing cone loss model, unless otherwise stated.

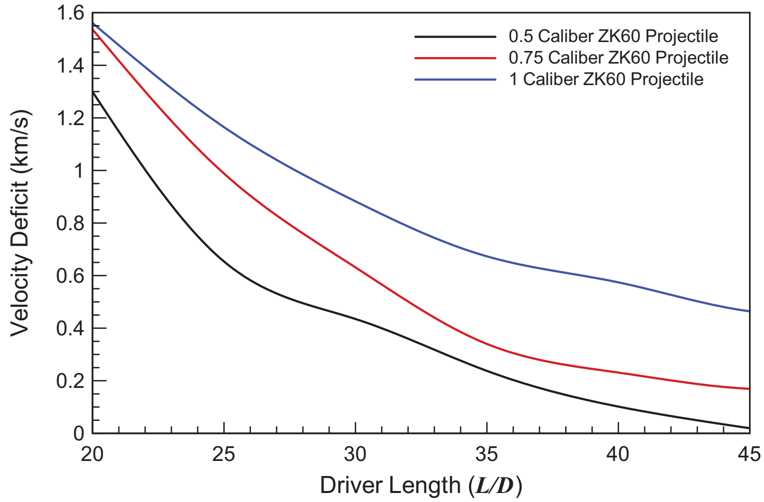

Figure 3–14: Velocity deficit from cone leaking as a function of driver length and projectile thickness. The reservoir opening is set equal to the driver diameter, simulating a full opening. The simulations include the reservoir expansion model and non-ideal driver effects. The launcher dimensions are: $D_{LT} = 5$ mm, $D_D = \sqrt{5}D_{LT}$, $U_D = 7$ km/s, Gas = 4MPa He, $L_R = 0.18L_D$, $L_{\text{offset}} = 3D_{LT}$, Proj = $0.5(L/D)$ ZK60

3.4 Propellant Equation of State

Up to this point, computational simulations have assumed that the propellant behaves as an ideal gas. This inherently assumes that the spacing between driver gas molecules is sufficiently large, such that molecular covolume forces can be neglected. In reality, the propellant density will be sufficiently large as to cause intermolecular repulsive forces. This effect has the potential to significantly increase the propellant pressure. The intermolecular forces also reduce the density of the gas, which can significantly increase the speed of sound of the propellant [8]. The simulations have also assumed that the specific heat ratio of the gas remains constant. However, the propellant temperatures in the implosion launcher are large enough to lead to dissociation of the hydrogen molecules (H_2 to 2H) and partially ionize the helium and hydrogen atoms (He to $He^+ + e^-$). These endothermic reactions lead to drastic deviations from the perfect gas model used in the original model. They result in significantly lower temperatures, which may reduce the speed of sound of the gas. In order to capture these effects, the solver will need to use a more appropriate equation of state.

Equation of state models that capture the intermolecular and covolume forces in real gases are quite common, notably the Abel and the van der Waals models. However, developing an equation of state for a gas which is dense and ionized or dissociated is significantly more difficult. It was felt that a tabular equation of state would be the easiest path to properly modeling the behavior of the driver gas. SESAME tables, developed by Los Alamos National Laboratories [7], are often used as a substitute to an equation of state in computational models. The tables can be used to determine the relationship between pressure, specific volume, and internal energy in a material. There are tables for both helium and hydrogen which span the range of temperatures and pressures in the implosion driven launcher. The data in the tables are based on analytical equations of state, empirical equations of state, and experimental data. As a result, these tables will allow the internal ballistics solver to capture the effect of covolume forces and dissociation/ionization reactions on the compression and subsequent expansion of the driver gas.

The main drawback of a tabular equation of state is that searching through the table and interpolating between the values can be computationally intensive. Another drawback is that the data in the table tends to be quite sparse, typically containing 5 to 7 points per order of magnitude. Nonetheless, by using high order interpolation between values, a good representation of real driver gas behavior can be obtained. The standard SESAME tables are presented in the form of pressure and internal energy matrices, where the each row and column of the matrix corresponds to a temperature and density respectively. The hydrocode requires pressure as a

$$\begin{bmatrix} p(e_1,\rho_1) & p(e_1,\rho_2) & p(e_1,\rho_3) \\ p(e_2,\rho_1) & p(e_2,\rho_2) & p(e_2,\rho_3) \\ p(e_3,\rho_1) & p(e_3,\rho_2) & p(e_3,\rho_3) \end{bmatrix}$$

Figure 3–15: Schematic of the modified SESAME matrix for pressure as a function of internal energy and density

function of density and internal energy. For this reason, the tables were modified to form a single matrix which gives the pressure as a function of internal energy and density. This is shown schematically in Figure 3–15. A Matlab two-dimensional spline interpolator is used to obtain the pressure at a given internal energy and density.

Using the SESAME database, it is possible to observe the effect of non-ideal gas behavior on the performance of hydrogen and helium launchers. Figure 3–16 shows a comparison of the projectile velocity profile for helium and hydrogen launchers to their corresponding ideal gas simulation. Figures 3–17, 3–18 and 3–19 show the evolution of the driver gas pressure, temperature, and internal energy behind the projectile as a function of its velocity. The reservoir expansion model was used during the simulations. As can be seen by the velocity profiles, the SESAME equation of state appears to have almost no effect on the performance of the launcher. The real gas pressure profiles show slight deviations from the ideal gas model. In the helium launcher, the initial real gas pressure is slightly lower due to ionization effects which lower the temperature of the propellant. In the hydrogen launcher, intermolecular repulsive forces caused by the high initial propellant density lead to a slightly higher initial propellant pressure. The initial differences between the projectile driving pressures in the ideal and real gas simulations appear to have a negligible effect on performance. The effects of driver gas dissociation and ionization are apparent

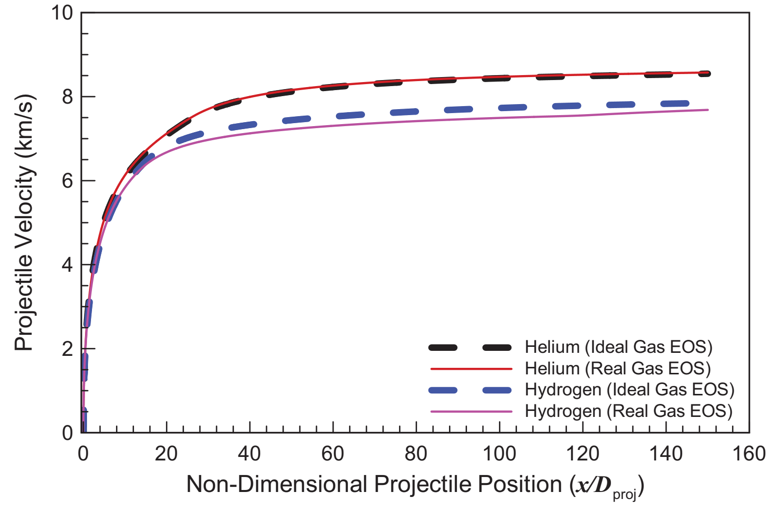

Figure 3–16: Comparison of the projectile velocity profile for real gas and ideal gas simulations of helium and hydrogen launchers. The simulations include the reservoir expansion model. The launcher dimensions are: $D_{LT} = 5$ mm, $D_D = \sqrt{5}D_{LT}$, $L_D = 37D_D$, $U_D = 7$ km/s, (Gas = 4MPa He, $L_R = 0.18L_D$) or (Gas = 5.8MPa H_2, $L_R = 0.12L_D$), $L_{\text{offset}} = 3D_{LT}$, Proj = $0.5(L/D)$ ZK60

in the temperature profiles shown in Figure 3–18. These reactions are highly endothermic, and thus severely limit the temperature of the gas. However, the nearly twofold decrease in propellant temperature appears to have little effect on launcher performance.

It is not readily apparent why the perfect gas equation of state results in nearly the same launcher performance as the SESAME equation of state despite the significant differences in the predicted propellant pressure and temperature. As will be seen in later chapters, the performance of the implosion-driven launcher is essentially determined by rate at which the pressure decays as the driver gas expands to propel the projectile. In the expansion process, the driver gas internal energy is converted into the kinetic energy of the gas and projectile. The rate at which the internal energy decays as a function of projectile velocity is a function of the speed of sound of the propellant. As can be seen in Figure 3–19, the initial internal energy of the

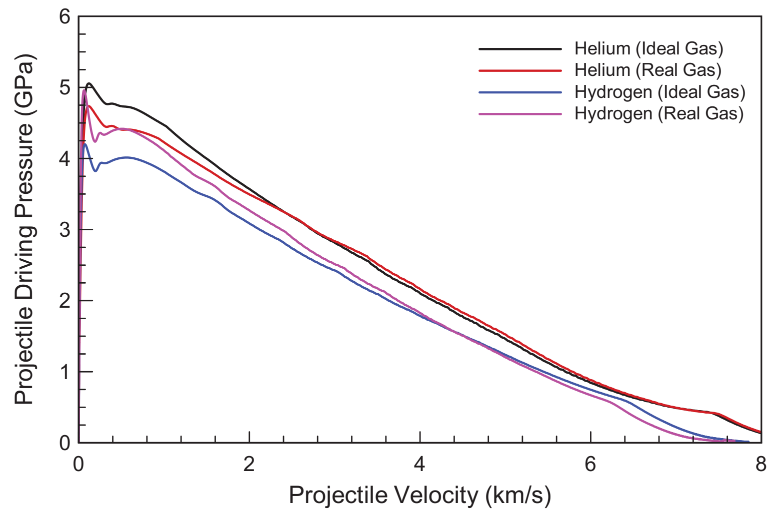

Figure 3–17: Comparison of the projectile driving pressure as a function of velocity for real gas and ideal gas simulations of helium and hydrogen launchers. The simulations include the reservoir expansion model. The launcher dimensions are: $D_{LT} = 5$ mm, $D_D = \sqrt{5}D_{LT}$, $L_D = 37D_D$, $U_D = 7$ km/s, (Gas = 4MPa He, $L_R = 0.18L_D$) or (Gas = 5.8 MPa H_2, $L_R = 0.12L_D$), $L_{\text{offset}} = 3D_{LT}$, Proj = 0.5($L/D$) ZK60

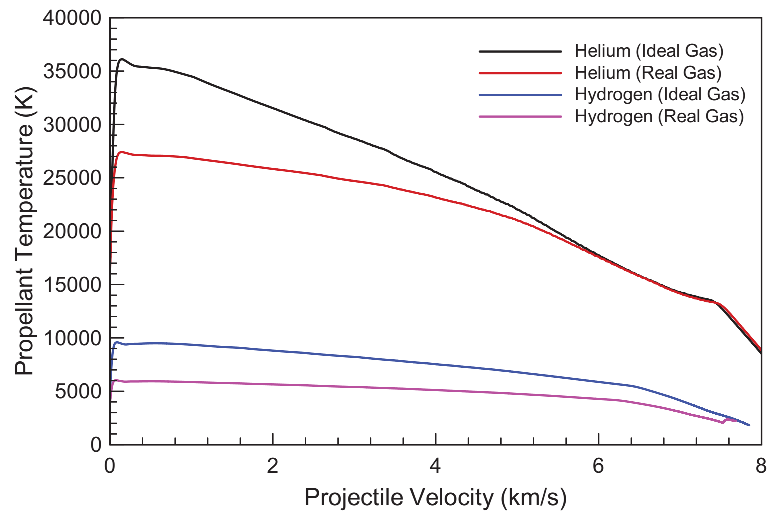

Figure 3–18: Comparison of the temperature of the driver gas directly behind the projectile as a function of velocity for real gas and ideal gas simulations of helium and hydrogen launchers. The simulations include the reservoir expansion model. The launcher dimensions are: $D_{LT} = 5$ mm, $D_D = \sqrt{5}D_{LT}$, $L_D = 37D_D$, $U_D = 7$ km/s, (Gas = 4MPa He, $L_R = 0.18L_D$) or (Gas = 5.8 MPa H_2, $L_R = 0.12L_D$), $L_{\text{offset}} = 3D_{LT}$, Proj = 0.5($L/D$) ZK60

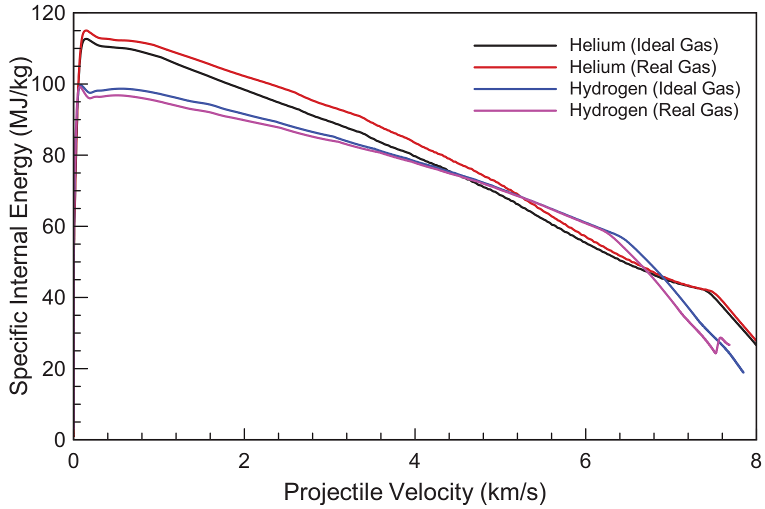

Figure 3–19: Comparison of the specific internal energy of the driver gas directly behind the projectile as a function of velocity for real gas and ideal gas simulations of helium and hydrogen launchers. The simulations include the reservoir expansion model. The launcher dimensions are: $D_{LT} = 5$ mm, $D_D = \sqrt{5}D_{LT}$, $L_D = 37D_D$, $U_D = 7\,\text{km/s}$, (Gas $=$ 4MPa He, $L_R = 0.18L_D$) or (Gas $=$ 5.8 MPa H_2, $L_R = 0.12L_D$), $L_{\text{offset}} = 3D_{LT}$, Proj $= 0.5(L/D)$ ZK60

gas and its decay as a function of velocity is nearly unaffected by the equation of state used for the simulation. This indicates that the energy required to accelerate the gas is not affected by the equation of state, which explains the nearly identical performance of both launchers. It appears that the actual speed of sound of the propellants is nearly equal to the ideal gas predictions. This is likely due to the fact that the decrease in speed of sound brought about by dissociation and ionization effects (lower temperature) is offset by the increase in speed of sound from real gas effects (higher density).

Although the projectile driving pressure is somewhat affected by intermolectular covolume forces (hydrogen launcher) and ionization effects (helium launcher) early in the launch cycle, these effects are short lived due to the rapid expansion of the driver gas, which quickly lowers the density and temperature to the point where these effects are negligible. As a result, the driving pressure in the ideal gas and real gas simulations quickly equalize and the small initial variations have little effect on launcher performance. Given the insensitivity of launcher performance to the equation of state, unless otherwise stated, simulations in this work will use the perfect gas formulation.

3.5 Gas Friction and Heat Transfer Effects

As the high temperature propellant flows through the launcher, there is a large temperature and velocity gradient between the flow and the launcher walls. As a result, momentum in the flow is lost due to the viscous shear stresses, and energy in the flow is lost due to convective heat transfer to the launcher walls. These phenomena can have a considerable effect on hypervelocity launchers, where hot gas must rapidly flow through long launch tube lengths to accelerate the projectile. A simple model was developed to consider the effect of heat transfer and friction within the internal ballistics solver. As will be seen, the friction and heat transfer equations are obtained using an internal pipe flow analysis based on friction factor correlations. The semi-analytical expressions for heat transfer and gas friction can then be applied directly to the numerical cells in the gasdynamics solver to evaluate the loss of momentum and energy over the timestep. The analysis is based on a model reported by Bogdanoff [11] which was used to simulate gas friction and heat transfer losses in a two-stage light gas gun internal ballistics solver.

The viscous friction force on a numerical cell (F_{wall}) can be calculated from the shear stress at the wall (τ_{wall}) as a function of the friction factor (f), and the density (ρ), velocity (U), diameter(D), and length (L) of the cell. The resulting wall friction term can be directly added to the momentum equation.

$$\tau_{\text{wall}} = \frac{1}{2} f \rho_{\text{cell}} (U_{\text{cell}})^2 \tag{3.45}$$

$$F_{\text{wall}} = \frac{\pi D_{\text{cell}} L_{\text{cell}}}{2} f \rho_{\text{cell}} (U_{\text{cell}})^2 \tag{3.46}$$

The Reynolds analogy can be used to obtain the heat transfer ($\dot{q}_{\text{wall}}$) as a function of the friction force and the difference between the flow total enthalpy (H_{cell}) and the boundary layer enthalpy (h_{wall}). The resulting expression gives the heat transfer per unit mass (m_{cell}) and can be directly subtracted from the energy equation.

$$\dot{q}_{\text{wall}} = \frac{F_{\text{wall}}(H_{\text{cell}} - h_{\text{wall}})}{m_{\text{cell}} U_{\text{cell}}} \tag{3.47}$$

The flow total enthalpy can readily be obtained from the internal energy (e), pressure (p), specific volume (v), and velocity of the cell. The boundary layer enthalpy is more difficult to determine, because the internal energy and specific volume of the gas is not known. Furthermore, the temperature (T) of the boundary layer (equal to the temperature of the launcher wall) is also not known due to heat transfer effects. However, the boundary layer enthalpy will be nearly negligible compared to the total flow enthalpy. For this reason, a number of simplifications can be made without any appreciable loss of accuracy:

1. Using a perfect gas model (constant c_p), the ratio of the wall enthalpy and the flow enthalpy is equal to the ratio of the temperatures
2. An ideal gas model (specific ideal gas constant R) can be used to obtain the temperature of the flow
3. A constant wall (or boundary layer) temperature of 300 K can be assumed

The following expression for the boundary layer enthalpy can be derived from these considerations:

$$h_{\text{wall}} = h_{\text{cell}} \frac{T_{\text{wall}}}{T_{\text{cell}}} \tag{3.48}$$

$$h_{\text{wall}} = h_{\text{cell}}(300\text{K})\frac{R}{p_{\text{cell}}v_{\text{cell}}} \tag{3.49}$$

Using this relation, the final form of the heat transfer equation can be written:

$$\dot{q}_{\text{wall}} = \frac{\pi D_{\text{cell}} L_{\text{cell}} f \rho_{\text{cell}} U_{\text{cell}}}{2m_{\text{cell}}}\left[\left(e_{\text{cell}} + \frac{p_{\text{cell}}}{\rho_{\text{cell}}}\right)\left(1 - \frac{T_{\text{wall}}}{T_{\text{cell}}}\right) + \frac{(U_{\text{cell}})^2}{2}\right] \tag{3.50}$$

The friction factor needed for the gas friction and heat transfer expressions is obtained from the Reynolds number of the flow, using the following relations for laminar, transitional, and turbulent flow:

$$\text{Re} = \frac{\rho_{\text{cell}} U_{\text{cell}} D_{\text{cell}}}{\mu_{\text{cell}}} \tag{3.51}$$

IF Re $\leq$ 1828

$$f = \frac{16}{\text{Re}} \tag{3.52}$$

IF 1828 $<$ Re $\leq$ 5507

$$f = 0.00875 \tag{3.53}$$

IF 5507 $<$Re

$$f = 0.049(\text{Re})^{-0.2} \tag{3.54}$$

In order to determine the Reynolds number of the flow, one needs the viscosity of the gas (μ_{cell}) at its current temperature and density. This data is difficult to obtain for the high temperatures and pressures encountered in implosion-driven launchers. However, if it is assumed that the driver gas behaves as an ideal gas, the viscosity will only vary with the temperature of the gas. The relationship between viscosity and temperature can be obtained using Sutherland's law:

$$\mu_{\text{cell}} = \mu_o \frac{T_o + C}{T_{\text{cell}} + C}\left(\frac{T_{\text{cell}}}{T_o}\right)^{3/2} \tag{3.55}$$

Helium:

μ_o=1.9×10^{-5} Pa s

T_o=273 K

C=79.4 K

Hydrogen:

μ_o=8.76×10^{-6} Pa s

T_o=293.85 K

C=72 K

Using ideal gas relations, the temperature of the gas can be obtained from its pressure and density. The viscosity of the gas can then be determined, which allows the Reynolds number and finally the friction factor of the flow to be obtained. This calculation is performed for each numerical cell before the calculations of wall friction and heat transfer, as each cell will have a different velocity, temperature, density, and radius. It should be noted that although the propellant of the IDL is affected by real gas and ionization effects, the expressions for gas friction and heat transfer are not particularly sensitive to the gas viscosity. As a result, it is expected that Sutherland's law will provide sufficiently good estimate of viscosity.

It is important to note that this simple model applies the classic steady state analysis of internal pipe flow to an unsteady problem where there are large temporal variations in the velocity and the thermodynamic properties of the gas. A more thorough method of determining the friction factor in an unsteady flow is presented by Bogdanoff [11]. It was reported that taking into account non-equilibrium effects

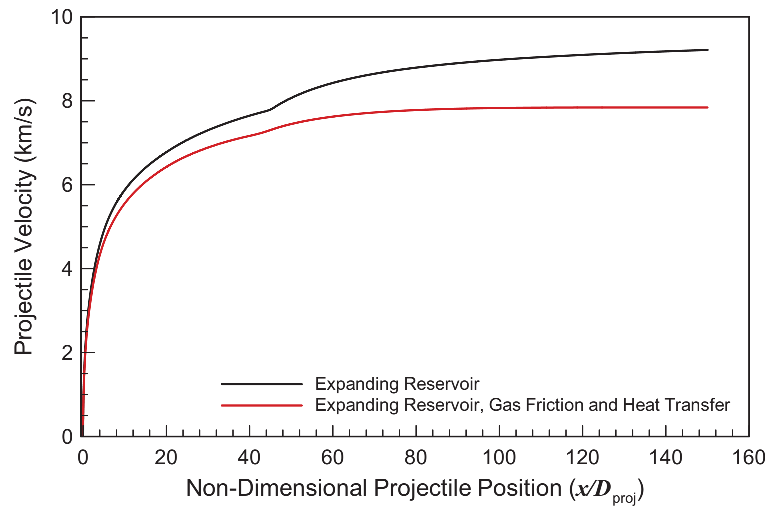

Figure 3–20: Comparison of the velocity profile for a launcher with and without heat transfer and gas friction losses. The simulations include the reservoir expansion model. The launcher dimensions are: $D_{LT} = 5$ mm, $D_D = \sqrt{5}D_{LT}$, $L_D = 37D_D$, $U_D = 7$ km/s, Gas = 4MPa He, $L_R = 0.18L_D$, $L_{\text{offset}} = 3D_{LT}$, Proj = $0.5(L/D)$

on the heat transfer and gas friction model resulted in a variation of 1 to 3 percent in the projectile velocity.

Figure 3–20 compares the projectile velocity profile of a typical helium implosion driven launcher with and without gas friction and heat transfer. The simulations include the expansion model. As can be seen, gas friction and heat transfer result in a performance loss of approximately 1.4 km/s. It is interesting to note that as a result of heat transfer and gas friction losses, the projectile appears to see almost no acceleration beyond launch tube lengths of 125 diameters.

In analyzing the effect of heat transfer losses on the performance of the launcher, it is also important to consider that the flow of driver gas can cause a significant quantity of ablation (i.e., erosion) of launch tube and reservoir wall material. The mixing of melted steel with the light gas has the potential to degrade the performance of the launcher by increasing the average molecular weight of the gas. Implosion launchers recovered after an experiment show signs of severe ablation of wall material. Determining the severity of the ablation early in the launch cycle and its resulting effect on launcher performance is of interest as it may impact a number of design decisions. Particularly, ablation effects are of interest when comparing the performance of helium and hydrogen launchers, which have drastically different propellant temperatures. A brief description of the suggested modeling approach is given below.

Computational work performed by Bogdanoff [10] has shown that ablation can be an important factor in limiting performance improvements from operating two-stage light gas guns at higher propellant temperatures. This indicates that ablation may also be of concern in implosion launchers, where the gas temperatures are significantly higher. Modeling the effect of ablation on the performance of the launcher is more challenging than modeling the heat transfer from the driver gas, because the wall temperature can no longer be assumed to be constant, and must be tracked using a radial heat transfer model that calculates the heat conduction away from the launch tube walls. The level of ablation is obtained by calculating the total heat flux into launcher walls from the heat transfer calculations above, and assuming that the heat goes into increasing the temperature of the wall until it reaches its melting point. Any further heat goes into melting the wall material (heat of melting). The conductive heat transfer away from the launch tube walls would be modeled using a heat transfer finite difference solver. The ablation model would also require an adjustment to the driver gas equation of state to compensate for the fact that the propellant is composed of a mix of molten steel and the driver gas. In developing an ablation model, it would be recommended to use more appropriate methods to

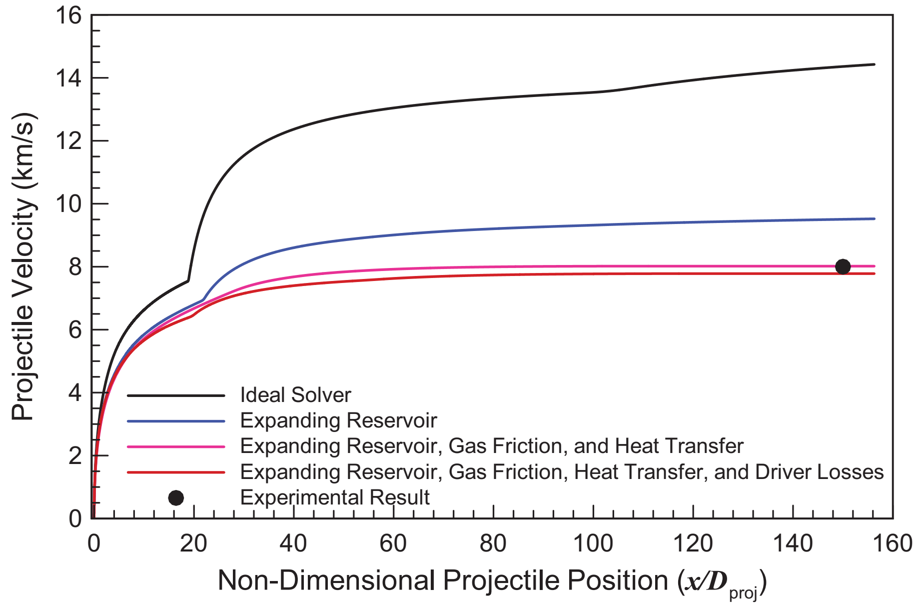

Figure 3–21: Effect of the three major losses on the velocity profile of the implosion launcher. The launcher dimensions are: $D_{LT} = 5$ mm, $D_D = \sqrt{5}D_{LT}$, $L_D = 37D_D$, $U_D = 7$ km/s, Gas = 4MPa He, $L_R = 0.10L_D$, $L_{\text{offset}} = 3D_{LT}$, Proj = $0.5(L/D)$

calculate the friction factor, including improved calculations for viscosity and non-equilibrium considerations, as these factors could have a significant impact on the level of ablation.

3.6 Experimental Validation

As was seen in the beginning of this section, the ideal version of the internal ballistics model failed to properly predict the performance of implosion launchers. In an effort to improve the modeling capability of the solver, a number of non-ideal effects were incorporated. Figure 3–21 shows the progressive effect of the three major non-ideal effects on the performance of the launcher. The experimental result for the corresponding launcher is also shown. As can be seen, the velocity predicted by the complete computational model is very close to the experimental velocity.

If one is to use the simulation results to improve the launcher design, it is important to confirm that the computational model is capable of reproducing a

Table 3–1: Comparison of simulation velocity predictions to experimental results

Shot ID	U_{exp} (km/s)	U_{sim} (km/s)	Ideal U_{sim} (km/s)	D_{LT} (mm)	Projectile	Driver Gas	$\frac{A_D}{A_{LT}}$	L_D (L/D)	$\frac{L_R}{L_D}$
L028	4.3	3.4	10.3	5	1.3 cal. Al6061	3 MPa He	5	110	0.1
L040	6.8	8.1	11.1	10	0.3 cal. Al7075	3.5 MPa He	5.2	30	0.12
L052	7.9	8.0	11	10	0.28 cal. Al7075	3.5 MPa He	5.5	23	0.12
L053	7.1	8.8	12	10	0.28 cal. Al7075	4.5 MPa He	5.5	23	0.12
L062	8.0	7.8	14.4	5	0.5 cal. ZK60	4 MPa He	5	37	0.1
PI 397-8	8.0	7.7	9.8	16	0.5 cal. Mg-Li	3.8 MPa He	4.8	28	0.18

variety of experimental results with significantly different launcher designs. Table 3–1 compares implosion-driven launcher experimental velocities to those predicted by the ideal simulation as well as the complete internal ballistics computational solver with non-ideal effects. Experimental velocities are measured by imaging the projectile using a high speed camera after it exits the launch tube. Typically, the total distance over which the projectile travels is approximately 400 mm, and the pixel size is on the order of 1 mm, resulting in a very precise measurement of projectile velocity. It can be seen that the predictions from the computational model are close to the results obtained in experiments.

There remains some variation between the velocities predicted by the solver and those obtained from experiments. A number of uncertainties contribute to the discrepancy between the results. First, it is important to note that there is some variation in the experimental launcher velocities. For example the L052 and L053 launchers in Table 3–1 have very similar design parameters, but the difference in the performance of the launchers is quite large (0.8 km/s). Another possible source of discrepancy is the inability of the model to simulate rupture of the reservoir and launch tube, which often occurs during experiments. Finally, a particular difficulty in modeling the implosion launcher is the sensitivity of the numerical model to the travel distance of the explosively driven piston. Varying the piston travel distance by one driver diameter can result in a performance change of up to 0.5 km/s. As the explosively driven piston reaches the sealing cone, it slows down and eventually stops because of the increasingly large wall thickness that must be imploded. As can be seen in Figure 3–22, it is not always clear from the launcher design exactly where the explosively driven piston will stop. This creates some uncertainty in the simulation results and can make it difficult to predict launcher velocities. It has been observed that experimental results are typically best represented when the explosively driven piston is stopped near the beginning of the sealing cone section. Despite these difficulties, the solver appears to be capturing the essential physics of the implosion launcher quite well. As will be seen, its ability to simulate the effect of non-idealities on the performance of the launcher will be critical to understanding the design tradeoffs inherent in an implosion-driven launcher.

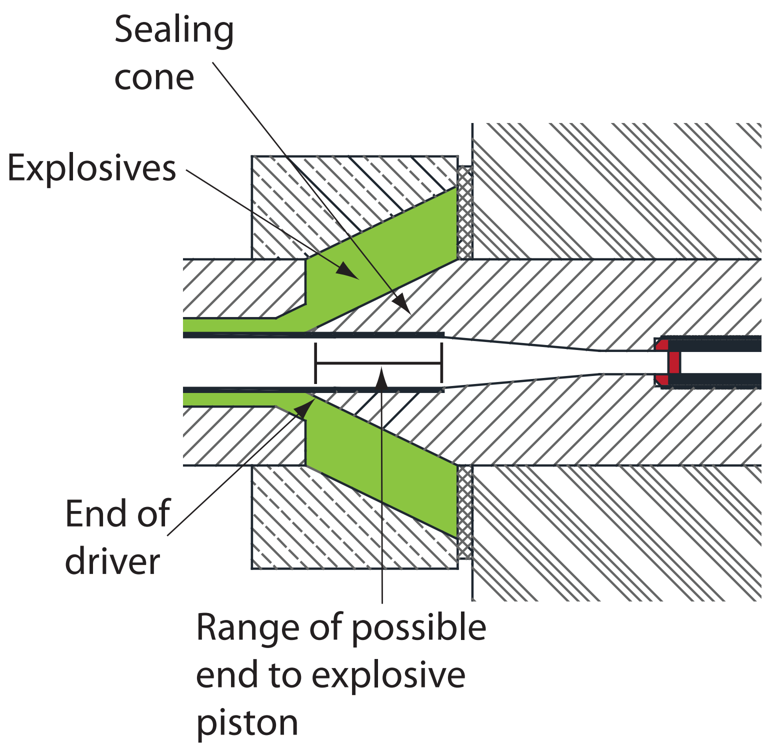

Figure 3–22: Detailed schematic of the sealing cone demonstrating the difficulty in determining the location where the explosively driven piston comes to a stop

CHAPTER 4
Internal Ballistics Considerations of an Ideal Implosion Driven Launcher

In order to effectively use the computational internal ballistics model, it is important to have a basic understanding of the main parameters affecting the launch cycle of an implosion-driven launcher. As will be seen, the launch cycle can readily be compared to that of a pre-burnt propellant ideal-gas gun (PPIG), which can be used to explain fundamental internal ballistics concepts. This section will use a simple PPIG analysis to provide an overview of the major design considerations in an implosion launcher, thus providing a framework for the launcher optimization work performed in Chapter 5. The analysis will be limited to the ideal operation of the launcher. However, care will be taken to highlight the limitations of the analysis and indicate how the results could be affected by non-ideal effects.

4.1 Introduction to the Internal Ballistics Design Parameters

It is important to understand how the design of a single stage implosion-driven launcher can be modified to improve the velocity potential of the launcher. The general goal of launcher design is to provide the highest possible impulse to the projectile. This must be done without damaging the projectile, which means that the design will be constrained by a maximum pressure. Therefore, the goal of the internal ballistics design is to maximize the average pressure applied to the projectile for a given maximum pressure. This Chapter will help establish an understanding of internal ballistics theory and determine the critical design parameters in an implosion launcher. This introductory section is meant to provide a brief overview of the design

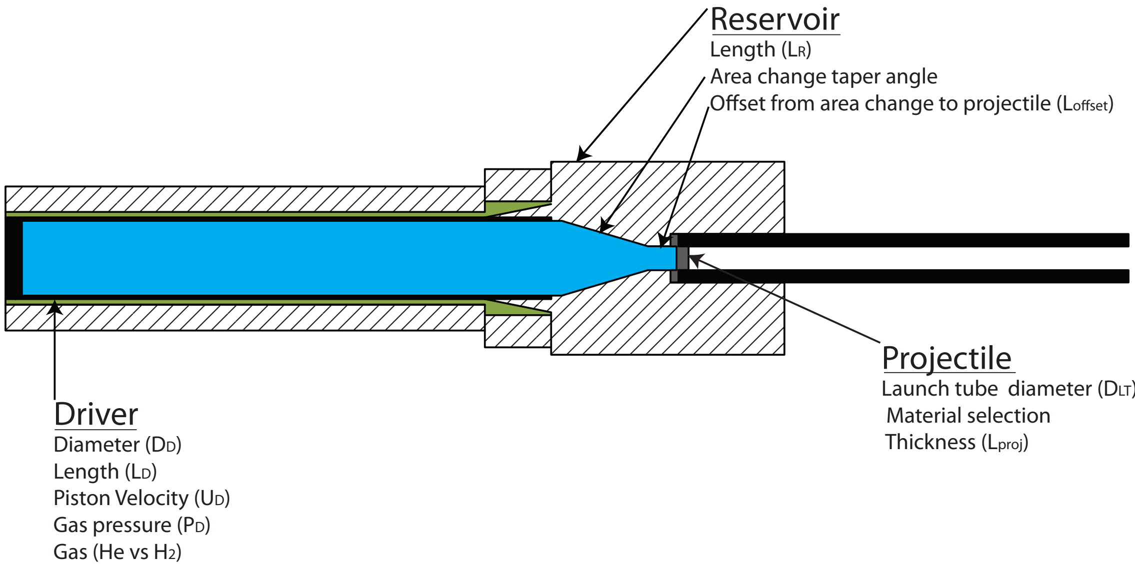

Figure 4–1: Schematic of the implosion launcher showing the design parameters that will be considered in internal ballistics analysis

Table 4–1: Summary of the major design parameters of the implosion driven launcher

Projectile	Driver	Reservoir
Thickness (L_{proj})	Length(L_D)	Length(L_R)
Material	Diameter(D_D)	Area change taper angle
Diameter (D_{LT})	Piston Velocity (U_D)	Offset to projectile (L_{offset})
	Gas pressure (p_D)	
	Driver gas (He vs H_2)	

of an implosion launcher in order to give meaning to the internal ballistics discussion in the following sections.

A standard implosion-driven launcher consists of a linear explosive driver that compresses the driver gas, a reservoir section that contains the driver gas during the projectile acceleration, and a launch tube through which the projectile accelerates. A basic schematic of the design is given in Figure 4–1. A summary of the design parameters is given in Table 4–1.

The design typically begins with the goal of launching a projectile of a certain size. The density and thickness of a projectile will determine its mass, which affects its acceleration and will ultimately have an important effect on the velocity potential of the launcher. The choice of projectile material also determines its strength, which influences the maximum driving pressure (and acceleration) that the projectile can withstand.

Once the size of the projectile has been fixed, a suitable driver must be chosen to deliver the launcher propellant. The driver diameter and length determine the volume of driver gas available to accelerate the projectile. These parameters can easily be varied by using different lengths and sizes of mechanical tubing. However, as was discussed in the introduction, the length to diameter ratio of the driver will be limited by non-ideal effects which degrade its performance. The type of gas used in the driver can also be varied. The performance of the launcher is heavily influenced by the molecular weight of the gas, which limits the options to the two light gases: helium and hydrogen. The initial pressure of the gas in the driver can also be varied. Increasing the fill pressure of the driver gas increases the mass of gas available to accelerate the projectile and increases the driving pressure on the projectile, which ultimately gives it a greater initial acceleration. Finally, by varying the type of explosive used in the linear explosive driver, the explosive-driven piston velocity can be changed. Increasing the piston velocity increases the strength of the shock wave that compresses the driver gas, resulting in higher driver gas pressures and temperatures.

The geometry of the reservoir, which is the interface between the driver and the launch tube, can also be varied. The length of the reservoir section is an important design parameter. As will be seen, the ratio of the driver length to the reservoir length determines how the explosively driven piston interacts with the compressed driver gas. The geometry of the area change section (sharp or tapered) and the initial position of the projectile relative to the area change section can also be varied and will influence the projectile driving pressure.

In this section, ideal internal ballistic theory will be used to understand the effect of varying these design parameters. This will help guide the computational analysis of the launcher in Chapter 5, as well as explain experimental and computational observations.

4.2 Analytical Launcher Analysis

The driver of an implosion-driven launcher propels the gas forward at the velocity of the explosively driven piston. This drives a shock wave which forms an increasingly long column of compressed gas ahead of the explosive pinch. As the shock wave reaches the projectile, it is reflected and begins to travel towards the back of the reservoir. The driver gas is stagnated by the reflected shock wave, bringing it to a stop at an even higher temperature and pressure. The pressure and temperature of the stagnated gas gradually decays as the gas accelerates to propel the projectile. The propellant typically sees no further compression until much later on in the launch cycle, when the explosive-driven piston interacts with the reflected shock wave. This launch cycle is similar to that of a PPIG, where one assumes that the propellant has been compressed and is quiescent before the projectile begins to accelerate. The simple PPIG model can be used to understand fundamentals of internal ballistics design and better appreciate the design considerations of an implosion-driven launcher. A comparison of the base pressure on the projectile as a function of its velocity for an ideal implosion-driven launcher and a PPIG is shown in Figure 4–2. The initial temperature and pressure in the PPIG were set to match the

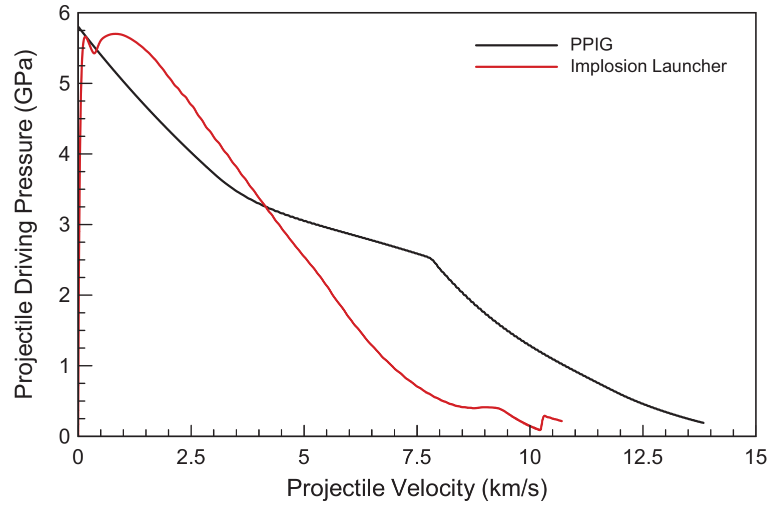

Figure 4–2: Comparison of the projectile driving pressure decay as a function of velocity for an ideal implosion launcher simulation and a PPIG simulation

reflected shock pressure and temperature in the implosion launcher. As can be seen, both profiles are quite similar which validates the discussion above. There are slight differences in the pressure profiles caused by interactions between the shock wave, the area change, and the expanding gas in the implosion-driven launcher. Nonetheless, a number of valuable lessons can be drawn from analyzing the internal ballistics of a PPIG.

4.2.1 Unsteady Expansion Process

The rapid acceleration of a projectile in a hypervelocity launcher is an unsteady process in which the wave dynamics in the driver gas play an important role. As the projectile accelerates forward, the driver gas must expand into the space created by the moving projectile. This leads to an unsteady expansion process, whereby both the driver gas and the projectile are accelerated in the launch tube. This process is shown schematically in Figure 4–3. As the projectile accelerates, expansion waves (or rarefaction waves) travel backwards into the driver gas. These isentropic waves travel at the local communication velocity of the gas (speed of sound minus gas

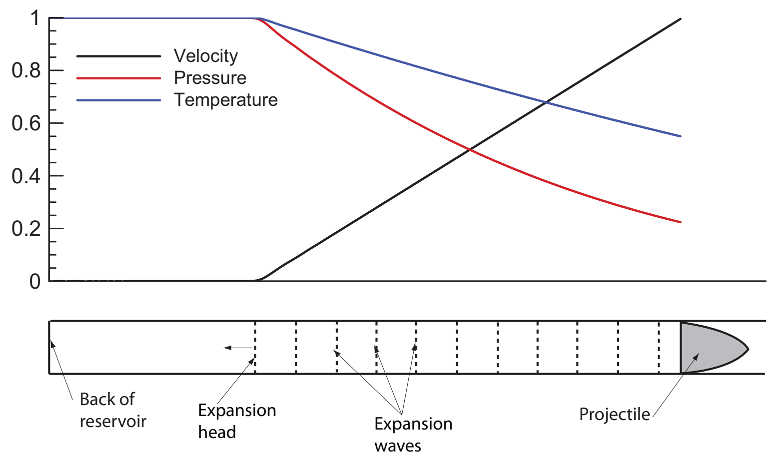

Figure 4–3: Schematic of the unsteady expansion process and the resulting gas velocity, pressure, and temperature profiles

velocity). The expansion waves accelerate the driver gas forwards, thereby lowering its pressure and temperature. As will be seen, the rate at which the driving pressure drops behind the projectile depends on the properties of the driver gas and the geometry of the reservoir. The goal is to design a launcher with a propellant and a reservoir geometry that will provide the highest possible average base pressure on the projectile, in order to maximize its velocity potential.

4.2.2 Propellant Considerations

The propellant in a hypervelocity launcher needs to be able to maintain a high pressure as it expands to propel the projectile. The magnitude of the pressure drop in an expanding flow is highly dependent on the thermodynamic properties of the gas. By analyzing the isentropic expansion (no heat transfer or friction losses) of a gas in a constant area section, one can obtain a much better understanding of the requirements for a high-speed launcher propellant. The expression for the differential change in pressure for a fluid element as a function of a differential increase in velocity across an expansion wave is given by Equation 4.1. Seigel presents the derivation of this equation using the method of characteristics [31]. It should be noted that this expression is obtained without relying on the ideal gas law, which means it applies to any fluid.

$$dp = -a\rho dU \tag{4.1}$$

As can be seen, the magnitude of the pressure drop is dependent on the gas property $a\rho$, known as the acoustic impedance. By minimizing the acoustic impedance, one can minimize the pressure drop for a given change in velocity. One needs to be careful not to jump to the conclusion that the ideal propellant would have a low density and sound speed. In order to compare propellants, it is instructive to use the ideal gas law to obtain the proportional change in pressure ($\frac{dp}{p}$) as a function of a change in velocity, as is shown in Equation 4.2. Of course this result is only valid for an ideal gas, but presents a much clearer picture of propellant requirements.

$$\frac{dp}{p} = \sqrt{\frac{\gamma MW}{R_u T}} dU = \frac{\gamma}{a} dU \tag{4.2}$$

Equation 4.2 shows that in order to have a low proportional change in pressure for a given change in velocity, the propellant should have a low molecular weight (MW) and a high temperature (i.e., a high speed of sound), and a low specific heat ratio (γ). A low molecular weight gas is desired because the gas needs to accelerate itself during the unsteady expansion process. The lighter the gas, the less energy is required to accelerate it. A high temperature gas will have a high internal energy. The expansion process essentially converts the internal energy of the gas into kinetic energy. Having more initial internal energy means there is more energy available to accelerate the gas. The specific heat ratio controls the change in pressure for a given change in volume for an isentropic expansion, as is shown in Equation 4.3. A gas with a lower specific heat ratio will have a smaller change in temperature and pressure as a gas expands into a given volume.

$$\frac{p_2}{p_1} = \left(\frac{\rho_2}{\rho_1}\right)^{\gamma} \tag{4.3}$$

The method of characteristics can also be applied to a constant area PPIG with an infinite chamber (gas reservoir) length to understand the effects of the gas properties on the performance of the launcher. The infinite chamber length assumption applies to any launcher before the first rarefaction wave from the projectile reflects off the back of the chamber and interacts with the projectile. Before this point, the gas properties behind the projectile are described by equations directly relating the projectile velocity to the speed of sound or pressure. Although most launchers do not operate with an effectively infinite chamber, the analysis is a useful tool for determining desirable propellant properties for a hypervelocity launcher. Again heat transfer and friction forces have been neglected, leading to an isentropic expansion. For an infinite chamber launcher the flow behind the projectile can be modeled using the method of characteristics in a simple wave flow. The resulting expressions for pressure and speed of sound behind the projectile as a function of velocity are given by Equation 4.4 and 4.5.

$$\frac{p_{\mathrm{proj}}}{p_o} = \left[1 - \frac{(\gamma-1)}{2}\frac{U_{\mathrm{proj}}}{a_o}\right]^{\frac{2\gamma}{\gamma-1}} \tag{4.4}$$

$$\frac{a_{\mathrm{proj}}}{a_o} = 1 - \frac{(\gamma-1)}{2}\frac{U_{\mathrm{proj}}}{a_o} \tag{4.5}$$

As can be seen, the decay in pressure and speed of sound depends on the ratio of the projectile velocity to the initial speed of sound of the propellant, as well as the specific heat ratio of the propellant. Figures 4–4 and 4–5 show the effect of the

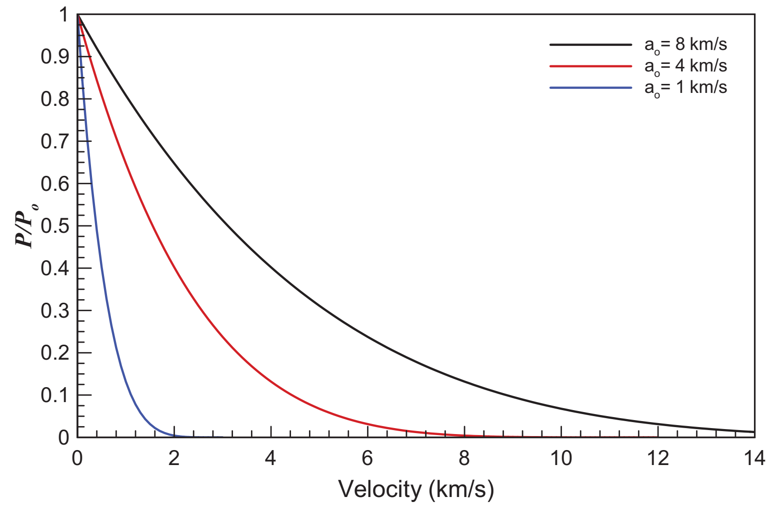

Figure 4–4: Graph showing the effect of the initial speed of sound of a gas on the change in pressure as a function of change in velocity for an unsteady expansion

speed of sound and specific heat ratio on the decay of the projectile base pressure as it accelerates. As expected, a driver gas with a high speed of sound and a low specific ratio will have a lower drop in pressure for a given increase in velocity, meaning that it is a superior propellant.

As can be seen from Equation 4.4, for any gas where $\gamma > 1$ the base pressure on the projectile eventually decays to 0. This occurs at the velocity where the speed of sound of the gas behind the projectile reaches 0. This velocity corresponds to the maximum possible projectile velocity in a constant area launcher, and is given by Equation 4.6:

$$U_{\text{escape}} = \frac{2}{\gamma - 1} a_o \tag{4.6}$$

The strong effect of the specific heat ratio on the escape velocity can be explained by the fact that a low specific heat ratio leads to a smaller temperature change as the gas expands. This is due to the fact that gasses with smaller specific heat ratios have more degrees of freedom and therefore have more internal energy stored for a given

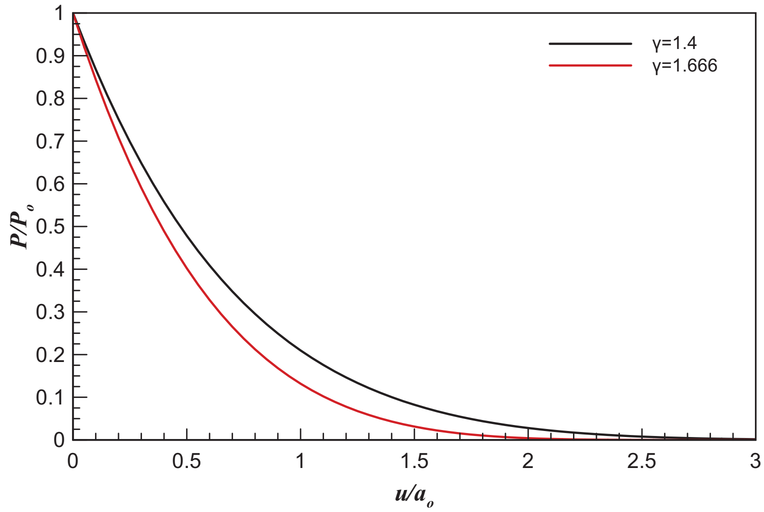

Figure 4–5: Graph showing the effect of the specific heat ratio (γ) of a gas on the change in pressure as a function of change in velocity for an unsteady expansion

temperature, causing the temperature to decay more slowly as the gas expands. As a result, the speed of sound in a gas with a lower specific heat ratio will decay more slowly. Equation 4.6 indicates that the maximum projectile velocity could approach 3 ($\gamma = 1.666$, helium) to 5 ($\gamma = 1.4$, hydrogen) times the initial speed of sound of the gas. Although a small difference in the specific heat ratio leads to large differences in the escape velocity, as can be seen in Figure 4–5, beyond twice the initial speed of sound, the pressure has dropped to less than ten percent of its initial value for both gases. The exponential decay in pressure along with heat transfer and friction losses in real launchers mean that in practice maximum projectile velocities are rarely above two times the initial speed of sound.

As is shown in Figure 4–4, propellant performance is strongly dependent on its speed of sound. Therefore, the performance of the launcher will be sensitive to the way in which the propellant is compressed. Figure 4–6 compares the speed of sound ratio as a function of pressure ratio for an isentropic and a reflected shock compression (as in an implosion driven launcher). As can be seen, the speed of

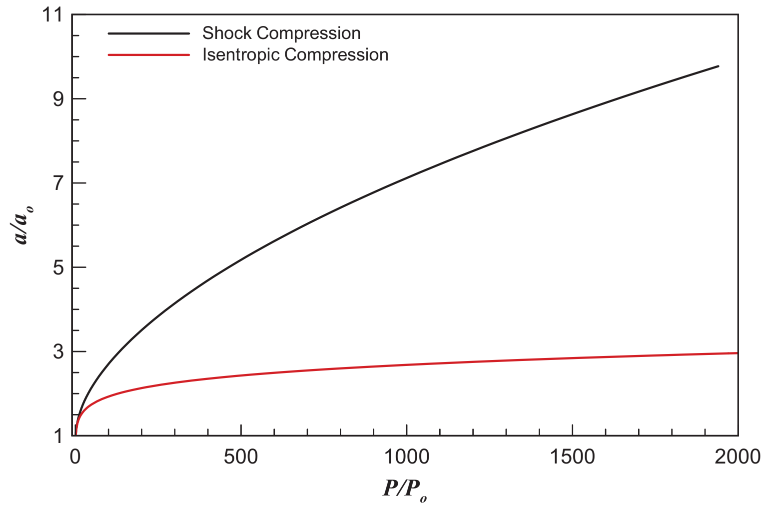

Figure 4–6: Comparison of the increase in speed of sound as a function of pressure ratio for an isentropic compression and a shock compression

sound ratio in a reflected shock compression is much larger, which means that there are significant advantages to providing a dynamic compression to the driver gas. In reusable launchers, such as two-stage light-gas guns, the ablation of launcher wall material places a practical limit on the propellant temperature, which limits the level of dynamic compression used in the launch cycle. However, since implosion launchers are single shot devices, they can utilize a much more dynamic compression cycle which compresses the driver gas to significantly higher temperatures. Figure 4–4 also indicates that it might be possible to improve the performance of an implosion-driven launcher by increasing the velocity of the explosively driven piston, as it would increase the pressure ratio and speed of sound ratio of the compression.

In practice, due to molecular weight considerations, there are only two options for the driver gas in light-gas launcher: hydrogen and helium. One might prematurely conclude that hydrogen should be the propellant of choice, given the fact that it has a lower molecular weight and lower specific heat ratio. However, it is important to remember that helium, having a higher specific heat ratio, typically reaches a much

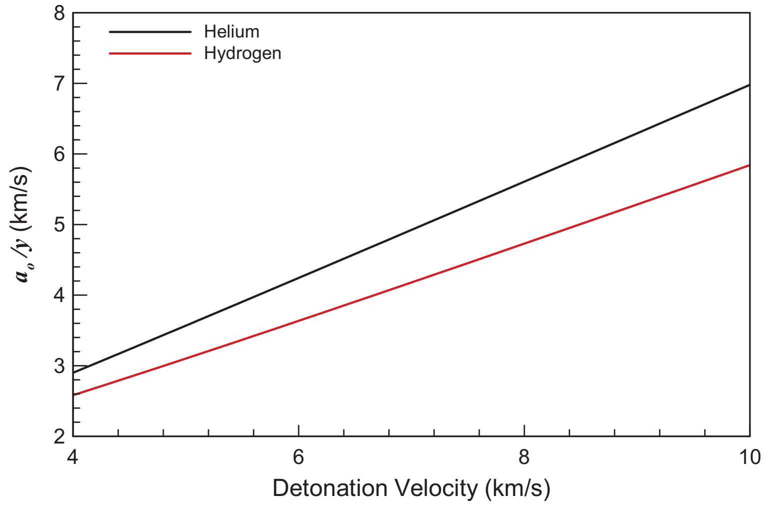

Figure 4–7: Comparison speed of sound divided by the specific heat ratio as a function of piston velocity for a reflected shock compression in helium and hydrogen. This provides an empirical comparative measure of the two gases as propellants in the implosion launcher.

higher temperature and speed of sound than hydrogen during the compression of the driver gas. Seigel [31] showed empirically that the ratio of $\frac{a_o}{\gamma}$ can be used to compare propellants with different specific heat ratios. Propellants with a higher $\frac{a_o}{\gamma}$ are expected to yield superior performance. Figure 4–7 shows the variation of $\frac{a_o}{\gamma}$ as a function of the piston velocity for a gas compressed by a shock reflection (as in the implosion-driven launcher). As can be seen, helium appears to hold a slight advantage over hydrogen in the piston velocities of interest (>5 km/s). This simple analysis appears to indicate that both gasses may be worthwhile candidates for propellants in an implosion-driven launcher.

4.2.3 Effect of Finite Driver Gas Mass in a Constant Area Launcher

A launcher with a gas reservoir of a finite size will have a lower performance than an effectively infinite chamber length launcher, given that there is a limited amount of propellant available to accelerate the projectile. A launcher can no longer be considered to have an infinite chamber length when the first rarefaction from the

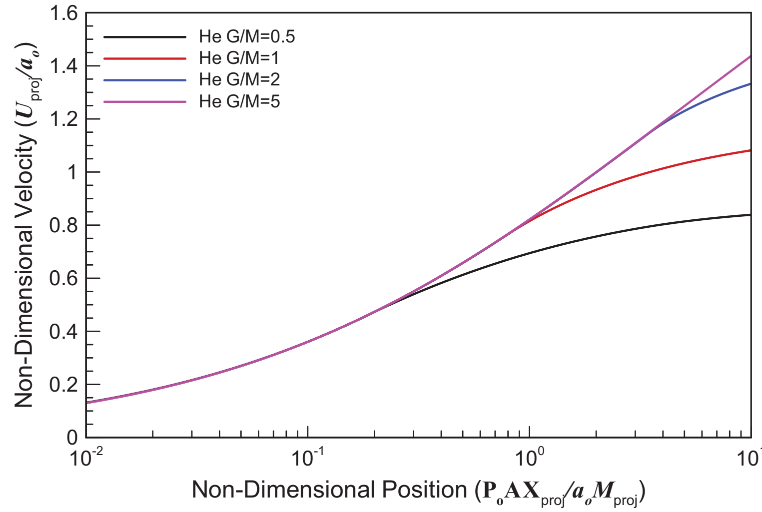

Figure 4–8: Non-dimensional projectile velocity as a function of its position in the launch tube showing the effect of driver gas mass to projectile mass on the performance of a PPIG

acceleration of the projectile reflects from the back of the chamber and catches back up with the projectile. The reflected rarefaction waves communicate the fact that there is a limited amount of propellant available to accelerate the projectile, which brings about a very steep decline in the projectile base pressure and significantly lowers the theoretical maximum attainable velocity of the propellant. The effect of having a finite mass of driver gas on launcher performance is demonstrated by Figure 4–8, which shows the non-dimensional projectile velocity as a function of non-dimensional distance for launchers with varying driver gas mass to projectile mass ratios (G/M). Initially all the curves lie together, but begin to diverge as the reflected rarefactions catch up to the projectiles in the launchers with lower G/M. This figure clearly indicates the strong dependence of the mass of driver gas on the maximum attainable velocity of a launcher.

As can be seen, increasing the G/M delays and diminishes the effect of reflected rarefaction waves on launcher performance. The driver gas mass can be increased by increasing the chamber length, increasing the density of the gas, or chambering the launcher (increasing the size of the driver relative to the launch tube). In an implosion driven launcher, the gas must be compressed into the chamber by the linear explosive driver. Therefore, the mass of driver gas available to accelerate the projectile is determined by the volume and initial density of the gas in the explosive driver. For this reason, the driver will need to be sufficiently long to generate enough driver gas to accelerate the projectile. As was discussed in the Introduction, non-ideal effects lead to large driver gas losses and reduced propellant compression in linear explosive drivers with large length to diameter ratios ($> 80\ L/D$). The design of the driver for an implosion launcher is a compromise between ensuring it is large enough to provide the necessary driver gas mass, while being sufficiently short as to ensure its performance is not degraded by non-ideal effects. As will be seen in Section 4.2.4, implosion-launchers are typically designed with chambrage (driver diameter is greater than the launch tube diameter), which allows a large mass of propellant to be contained in a relatively short driver.

At this point it is instructive to compare the effect of finite driver gas mass for helium and hydrogen implosion-driven launchers. The comparison will be performed for launchers with the same driver length, since both helium and hydrogen driver lengths will be limited by non-ideal effects. Furthermore, the initial driver gas pressures should be set such that the reflected shock pressures in both launchers are also equal. In order to get similar initial driving pressures in an implosion launcher, the initial density of the helium and the hydrogen drivers must be approximately equal. This means that for a fixed driver length and a similar maximum allowable pressure, hydrogen and helium launchers will have nearly the same G/M. Using the previously obtained result that the ratio of $\frac{a_o}{\gamma}$ will be similar for both gases (see Figure 4–7),

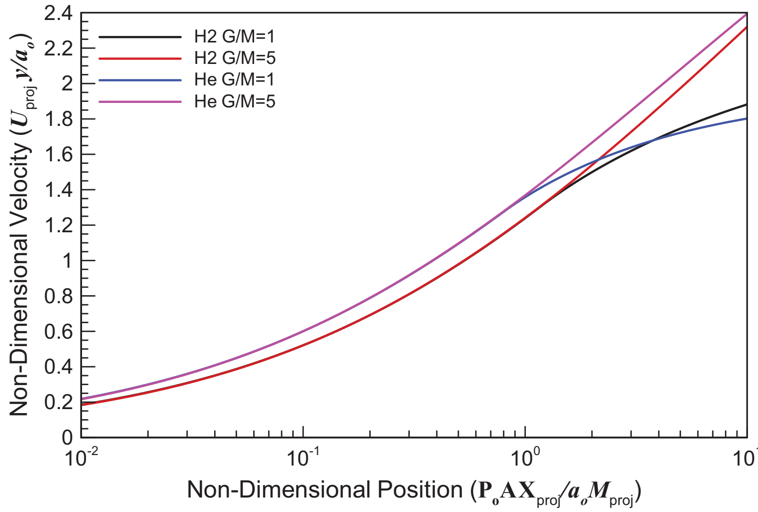

Figure 4–9: Comparison of non-dimensional projectile velocity as a function of its position in the launch tube for helium and hydrogen PPIGs with finite driver gas mass

the performance of helium and hydrogen launchers can be compared in a plot similar to Figure 4–8, where the velocity is now non-dimensionalized by $\frac{a_o}{\gamma}$. As can be seen in Figure 4–9, for a similar G/M the performance of both gases is nearly equivalent. Once again, helium appears to hold a slight advantage over hydrogen. The comparative performance of helium and hydrogen will be further verified in Section 5.3 using a complete computational model of the implosion launcher, including relevant non-ideal effects.

4.2.4 Effect of Chambrage

A common way to improve launcher performance is to increase the diameter of the reservoir. This is known as chambering the launcher, and improves performance by increasing the mass of driver gas available to accelerate the projectile. If the chamber length to diameter ratio is fixed, as is the case for an implosion driven launcher, a chambered launcher will have the advantage of having a driver that is both larger and longer, which allows for substantial gains in terms of G/M for relatively small values of chambrage. In a chambered launcher, the expansion waves that are produced as the projectile accelerates partially reflect from the area change section as compression waves, communicating the fact that there is a large mass of gas that is available to accelerate the projectile. The reflected compression waves help maintain a higher base pressure on the projectile as it accelerates. Figure 4–10 shows a schematic of the wave dynamics in a chambered PPIG. The reflected compression waves allow a chambered launcher to perform better than a non-chambered launcher, even for similar values of G/M. Seigel determined empirically that when comparing launchers with the same G/M and different chambrage, launchers with more chambrage perform better early in the launch cycle, but that all launchers with similar G/M perform more or less the same after many rarefaction wave reflections (for very long launch tube lengths) [31].

In order to quantify the potential performance increase from chambrage in an implosion launcher, a series of PPIG simulations were run for various values of chambrage. The chamber length to diameter (L/D) ratio of the PPIG was held constant and was chosen to represent a typical implosion-driven launcher. Figure 4–11 shows the non-dimensional projectile velocity as a function of non-dimensional position for various area ratios. As can be seen, significant gains in projectile velocity can be made using chambrage. Early in the launch, the reflected compression waves in the chambered launchers give a significant velocity advantage. Later in the launch cycle, the advantage of the increased G/M in the chambered launchers is also beneficial. It should be noted that for a fixed launch tube length, a point of diminishing returns is reached, where there appears to be little benefit to further increasing the area ratio. It is also important to note that although Figure 4–11 shows the behavior of a gas

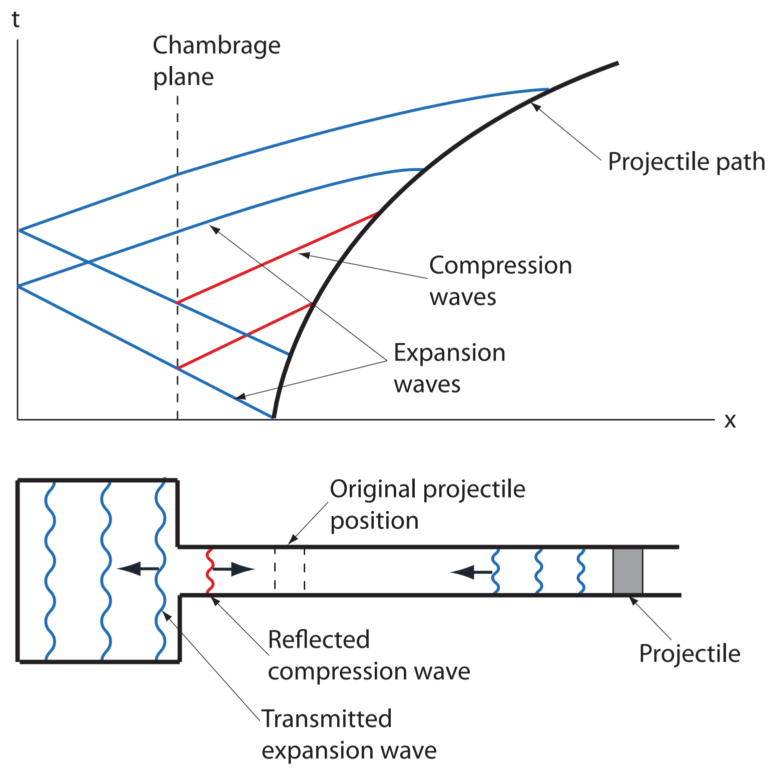

Figure 4–10: Schematic of the wave dynamics in a chambered PPIG launcher

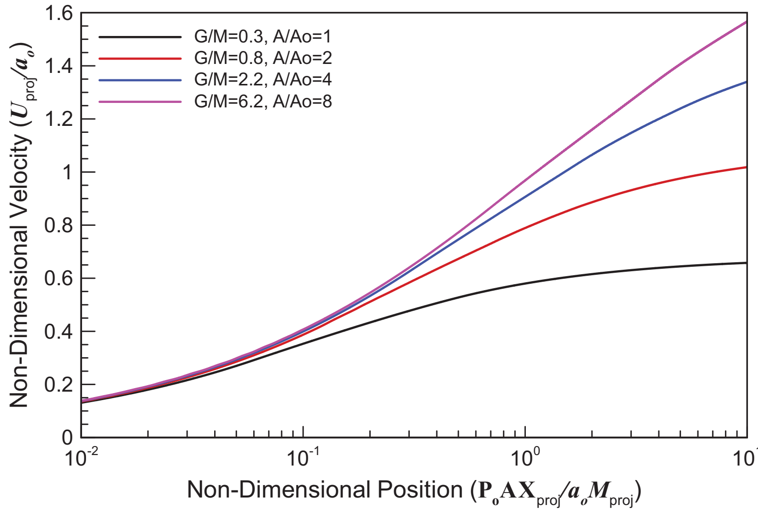

Figure 4–11: Non-dimensional projectile velocity as a function of its position in the launch tube showing the effect of chambrage on the performance of a PPIG

with a specific heat of 1.666, the effect of chambrage has been shown to be relatively insensitive the specific heat ratio of the gas [31], which means that similar gains can also be expected for hydrogen launchers.

Two important design consideration play into the choice of the area ratio in an implosion-driven launcher. First, the area ratio section focuses the precursor shock wave, which means that if the initial driver gas fill pressure is held constant, the initial projectile base pressure will be higher in a launcher with a larger area ratio. Although this may seem desirable, the pressures generated in an implosion driven launcher with modest chambrage are already sufficient to cause severe projectile damage or fracture. In order to maintain acceptable projectile loading, the initial fill pressure in launchers with large area ratios must be lowered, which offsets some of the advantage of increasing the driver volume. This effect will be observed using complete launcher simulations in Section 5.5. The second important factor in choosing a value of chambrage in a real launcher stems from the fact that the mass of steel and explosive required for the linear explosive driver scales with the cube of its radius.

This means that the cost of the launcher and the size of the facility required to conduct experiments (indoor facilities have explosive mass constraints) can escalate quickly as the chambrage is made larger.

As can be seen, the choice of driver length and diameter in an implosion driven launcher appears to be a compromise between reaching the target G/M ratio for an effectively infinite chamber length, while ensuring that the explosive driver is short enough to maintain adequate performance, and that its diameter is in the range where the launcher benefits from chambrage without greatly increasing the cost of the launcher.

Finally, it should be noted that the initial position of the projectile relative to the area change section can have an important impact on the projectile base pressure history. By placing the projectile closer to the area change section, the reflected compression waves from the reservoir can reach the projectile faster during its early acceleration. However, in the implosion driven launcher, the propellant behind the shock wave flows through the area change section before it reaches the projectile. Watson [38] showed both computationally and experimentally that the area change section can disturb the flow, which can damage the projectile by loading it unevenly. An offset of approximately three diameters between the end of the area change section and the initial projectile position was suggested in order to allow the flow to become more uniform, thus ensuring projectile survivability. The sensitivity of projectile velocity to its initial position relative to the area change section will be determined using computational simulations in Section 5.6.

4.2.5 Projectile Considerations

The performance of a launcher is very sensitive to the mass and cross-sectional area of the projectile being launched. This was shown by Figure 4–8, where one can see that by lowering projectile mass, the G/M ratio is increased and the launch tube length required to reach a given velocity is decreased. These effects can significantly increase the final projectile velocity for a given launcher configuration. To gain an understanding of projectile design considerations, one can use the simple case of a constant base pressure launcher, where the acceleration of the projectile is assumed to be constant. Equation 4.7 shows the expression for the velocity of a projectile in a constant base pressure launcher in terms of the pressure (P), the position (X/D), the projectile density (ρ_{proj}), and the projectile thickness ($(L/D)_{\text{proj}}$). As can be seen, the position and projectile thickness have been non-dimensionalized. In order to improve the performance of a launcher through projectile considerations, one must minimize the $\rho\left(\frac{L}{D}\right)_{\text{proj}}$ term, which will be called the "scaled projectile density." Scaled projectile density can be reduced by making the projectile thinner (reducing $(L/D)_{\text{proj}}$) or reducing the density of the projectile material. Of course, there are practical limits to the projectile thickness and its density. As will be seen in Section 5.2, the projectile design in an implosion driven launcher is even more critical than a typical launcher due to the severe expansion of the reservoir under the high driving pressure. As the projectile aerial density (mass over area) is made larger, the projectile's resistance to acceleration is made larger, which means that the projectile takes longer to be accelerated. This gives more time for the driving pressure to be attenuated by the expansion of the reservoir.

$$U = 2P\left[\frac{1}{\rho_{\text{proj}}}\left(\frac{D}{L}\right)_{\text{proj}}\right]\frac{X}{D} \tag{4.7}$$

It should be noted that in order to maintain reasonable scaled densities, projectiles in hypervelocity launchers are typically launched using lightweight sabots.

Sabots are cylinders constructed to carry the projectile down the launch tube. By increasing the apparent cross sectional area of the projectile, sabots can propel spheres, rods, and dense flyer plates which would otherwise have unacceptably large scaled densities. The projectile discussion in this section, as well as throughout this work will be limited to launching uniform cylindrical projectiles, keeping in mind that these projectiles could eventually be used as sabots to perform hypervelocity impact testing. Theoretically, the loading on the projectile should be completely uniform and the confinement from the barrel walls should allow the projectile to withstand driving pressures much greater than its yield strength. In fact, the loading on the projectile is akin to a glass of water in a very large gravitational field. The stress state is purely hydrostatic, and increases towards the bottom of the glass. The water has no strength, but will retain its shape as long as it is constrained by the walls of the glass. Similarly, the stress state in the projectile should be relatively hydrostatic, with the pressure increasing towards the projectile surface being driven by the propellant gas. However in a real launcher system, imperfections in the launch tube, interactions with shock waves in the flow, or flow disturbances (both behind and ahead of the projectile) can lead to uneven loading on the projectile. For this reason, a projectile must have suitable strength to survive the uneven loading in a real launch system. The projectile must also be thick enough to prevent it from tumbling in the launch tube when exposed to uneven driving forces. The large hydrostatic stresses on the projectile can also cause large frictional forces at the interface between the projectile and the launch tube. This is likely to lead to erosion of the radial surface of the projectile. As the driving pressure decreases, the stress at the projectile-barrel interface may decrease to the point where the eroded projectile will be prone to tumbling or to allow severe blow-by of driver gas.

Projectile design becomes a compromise between choosing a low density material while ensuring it has the required strength to survive the launch, and making the projectile as thin as possible while ensuring it is reliably accelerated without tumbling. Section 5.2 will present the computational and experimental work performed in designing projectiles for implosion driven launchers.

4.2.6 Propellant Fill Pressure

By adjusting the initial driver gas fill pressure in the implosion-driven launcher, one can increase both the G/M and the initial rate of acceleration of the projectile. For example, if the initial fill pressure in an implosion-driven launcher is doubled, the G/M of the launcher will be doubled. The initial projectile driving pressure will also be doubled, which means that the projectile will have travelled twice the non-dimensional distance for a given launch tube length. As was seen in Figure 4–8, both these effects have the potential to significantly improve the performance of a launcher.

Although linear explosive drivers can produce very large reflected shock pressures (>10 GPa), non-ideal effects related to projectile damage and severe expansion and fracture of the reservoir limit the potential gains from increasing the launcher fill pressure. The ideal propellant fill pressure in an implosion launcher is determined by the point of diminishing returns where the losses related to projectile damage and reservoir fracture begin to outweigh the gains from increasing the G/M and the initial rate of acceleration of the projectile. Section 5.2 will present experimental and computational results in an effort to quantify the gains from increasing fill pressure.

4.2.7 Effect of Reservoir Length

The reservoir length is defined as the distance between the back of the reservoir once it has been sealed and the end of the area change section. The reservoir length

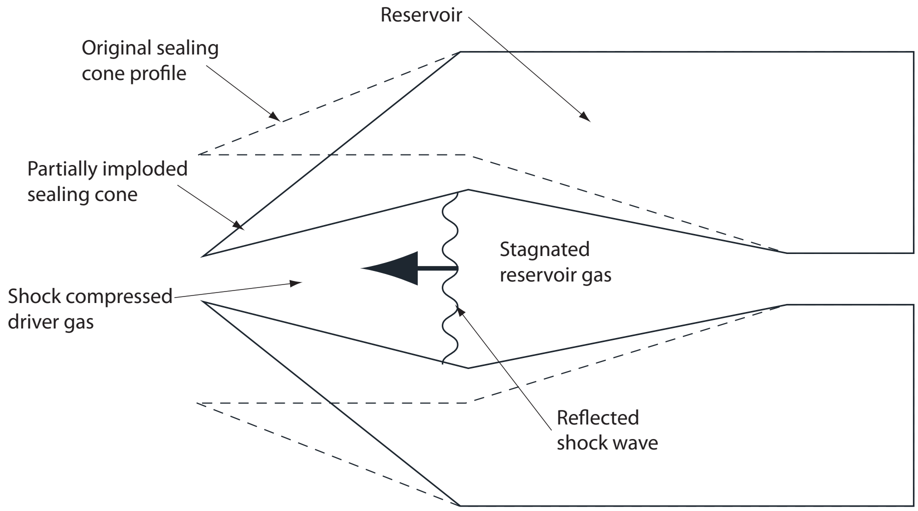

Figure 4–12: Schematic of the reflected shock wave criteria used to determine the length of the reservoir in an implosion launcher

is typically chosen such that the explosively driven piston stops when it meets the reflected shock wave, as is shown in Figure 4–12. If we neglect the slight variations of the shock wave velocity in the area change section, a simple analytical expression can be obtained for the reservoir length corresponding to this criterion. As can be seen in Equation 4.8, the ratio of reservoir length to driver length is dictated by the explosive-driven piston velocity (U_{piston}), the precursor shockwave velocity (U_S), and the reflected shockwave velocity ($U_{S\text{refl}}$). These parameters can be obtained analytically from the conservation of mass, momentum, and energy across the incident and reflected shock wave. From this analysis it can be seen that the reservoir length (L_R) should be approximately 10 percent of the driver length (L_D) for a helium launcher, and 6 percent for a hydrogen launcher.

$$\frac{L_R}{L_D} = \left(\frac{1}{U_{\text{piston}}} - \frac{1}{U_S}\right)\left(\frac{1}{U_S} + \frac{1}{U_{S\text{refl}}}\right) \tag{4.8}$$

If the reservoir is made longer than this criterion, the explosively driven pinch stops before reaching the reflected shock wave. The sudden deceleration of the "piston" can rapidly expand the gas in the reservoir, resulting in a sudden drop in the projectile driving pressure. Conversely, if the reservoir is made much shorter than this criterion, the explosively driven pinch can be disrupted by trying to implode and drive forward the dense stagnated driver gas in the reservoir. This disruption can lead to significant driver gas loss, which could also result in a sudden drop in the projectile base pressure. As can be seen, the choice of reservoir length is a compromise between ensuring that the driver gas is sufficiently compressed, while allowing the explosively driven pinch to seal the driver gas. This effect will be examined through the use of computational simulations in Section 5.6.

4.2.8 Further Compression of the Driver Gas

The PPIG analysis assumes that the driver gas is not further compressed once the projectile begins to accelerate. As was seen in Figure 4–11, operating the implosion-driven launcher with chambrage should allow it to reach velocities well above $1.5a_o$, or 12 km/s in a helium launcher. Although the implosion launcher appears to have the potential to reach very large velocities operating as a PPIG, losses related to the expansion of the chamber under the large driver gas pressure significantly limit its velocity potential. Although small performance increases can be achieved through the careful consideration of the internal ballistics design parameters outlined above, one will always be limited by the exponential pressure decay during the expansion of the driver gas. However, it is possible to gain significant velocity potential by continuing to compress the driver gas during the launch cycle. Indeed, by continuing to add energy to the flow, it is possible to maintain a nearly constant base pressure on the projectile. The ability of high explosives to deliver large amounts of energy in a very short period of time makes them an ideal tool for continuing to add energy to the driver gas during the launch cycle.

As was mentioned in the Introduction, the Physics International launcher demonstrated significant performance gains by surrounding the reservoir with a layer of explosive that was detonated during the early stages of projectile acceleration. This technique was able to reverse the effects of radial expansion by partially imploding the reservoir. As a result, the decay of the projectile driving pressure was significantly reduced. The reservoir explosive technique has been verified experimentally and will be reported in Section 6.1.

Although reservoir explosives can help slow the decay in the projectile driving pressure, this technique is limited by the fact that the explosive must be detonated well after the projectile has been set in motion. This ensures that the projectile is not damaged by the stress wave created by the detonating explosive. For this reason, reservoir explosives should be seen as a technique for improving launcher efficiency rather than a method for providing a constant projectile driving pressure.

Further gains could be made from a technique that gradually increases the reservoir pressure during the initial projectile acceleration. This can be done by accelerating the explosive-driven piston in the linear explosive driver. As the piston accelerates, compression waves are sent forward communicating the fact that the gas is being driven more aggressively. If the timing of the accelerating piston is set such that the compression waves reach the reservoir as the projectile begins to accelerate, a constant base pressure can be maintained on the projectile until the explosive-driven piston reaches the launcher chamber. The challenge in implementing this technique is designing a linear explosive driver with an accelerating explosive-driven piston. In order for this technique to work properly, the accelerating piston must be capable of accelerating the driver gas in the linear explosive driver without incurring significant gas loss through the explosive pinch. The accelerating driver piston will be discussed in further detail in Section 6.2.

CHAPTER 5
Parametric Study of Single-Stage Implosion-Driven Launcher

The pre-burnt propellant ideal-gas gun analysis was valuable in drawing a number of important conclusions on the effect of varying the major design parameters of the implosion launcher. From the analysis, it is possible to formulate a general set of design guidelines for the launcher:

1. maximize propellant speed of sound
2. maximize driver gas mass to projectile mass (G/M)
3. maximize driver to launch tube area ratio (chambrage)
4. peak driving pressure should be near the limit of projectile survivability
5. minimize projectile scaled density ($\rho\left(\frac{L}{D}\right)$)

Although valuable, these qualitative criteria cannot be used to design a launcher, since they do not take into account the inherent design tradeoffs brought about by the non-ideal effects and realistic limitations on the size and cost of experiments. In order to establish design criteria for the launcher, complete computational simulations as well as experimental results are needed. In this section, computational and experimental data will be used to quantify the effect varying the design parameters of the launcher, with the goal of identifying a range of optimal operation or diminishing returns for the design parameters identified in Section 4.1. As will be seen, the scalability of the launcher will allow these design criteria to apply to wide range of launcher sizes.

It is important to understand the limitations of this analysis. Within the scope of this project, it is not realistic to perform a complete multi-parameter optimization that covers the entire design map of an implosion-driven launcher. The conclusions drawn from the analysis in the previous section and the experience acquired from performing experiments will be used to focus the parametric study. For example, when studying the effect of driver geometry, the projectile mass and maximum projectile base pressure will be held constant at values established during experimental trials. It is also important to note that although the internal ballistics model takes into account a number of important features of the implosion driven launcher, its results should be taken with some skepticism. The value in this analysis is not in predicting the exact performance of a launcher or the exact gains from a design change, but rather in identifying design guidelines that are applicable to a reasonably wide range of implosion-driven launchers, as well as strategies for improving upon the current state of the art launcher design.

As will be seen, the ability of the computational model to study the effect of varying a large quantity of design parameters over a wide range will help provide valuable insight into how one might go about improving the design of an implosion launcher. Experiments will be used to validate the conclusions that are drawn and help pinpoint design criteria that cannot be determined solely by the computational model. It should be noted that the analysis will rely on launcher data obtained throughout the McGill project (including experiments performed before the present authors involvement in the project), as well as experiments reported during the Physics International project.

5.1 Implosion-Driven Launcher Scalability

Performing a parametric study of the launcher design is much more valuable if it can be done using non-dimensional design parameters that can be scaled to any size launcher. Using analytical and computational analyses, this section will show that the performance of implosion-driven launchers, including non-ideal effects, scales very well for a large range of launcher sizes. The fundamental design of the implosion launcher will be defined using the following non-dimensional parameters: the driver length to diameter ratio ($\left(\frac{L}{D}\right)_D$), the area ratio between the driver and the launch tube ($AR = \frac{A_D}{A_{LT}} = \left(\frac{D_D}{D_{LT}}\right)^{\frac{1}{2}}$), the ratio of reservoir length to driver length ($\frac{L_R}{L_D}$), the effective projectile density ($\rho_{\text{proj}}\frac{L_{\text{proj}}}{D_{LT}}$), and the projectile position to launch tube diameter ratio ($\frac{X_{\text{proj}}}{D_{LT}}$).

The goal of the scalability analysis is to show that the launcher performance is independent of scale, as long as these non-dimensional design parameters are held constant. In order to establish the scalability of the launcher, it must be shown that the ideal performance of the launcher remains constant when these design parameters are fixed. Furthermore, it must be shown that the real performance of the launcher, which is affected by radial expansion losses, driver non-ideal effects, and gas friction and heat transfer losses, also remains constant, regardless of the scale of the launcher.

The non-dimensional curves of launcher performance as a function of G/M for a PPIG showed that the performance of a launcher will scale well as long as the G/M ratio, non-dimensional launch tube length, and the initial properties of the compressed driver gas remain constant. As can be seen below, by keeping the non-dimensional design parameters and the initial driver gas density constant, the G/M and launch tube length of the launcher remain constant.

$$\frac{G}{M} = \frac{\rho_o L_D A_D}{\rho_{\text{proj}} L_{\text{proj}} A_{LT}} = \rho_o AR^{\frac{3}{2}} \left(\frac{L}{D}\right)_D \left(\frac{D_{LT}}{\rho_{\text{proj}} L_{\text{proj}}}\right) \tag{5.1}$$

$$\bar{X} = \frac{P_o A_{LT} X_{\text{proj}}}{a_o m_{\text{proj}}} = \left(\frac{\rho_o}{\gamma}\right) \left(\frac{D_{LT}}{\rho_{\text{proj}} L_{\text{proj}}}\right) \left(\frac{X_{\text{proj}}}{D_{LT}}\right) \tag{5.2}$$

In an implosion launcher, the internal ballistics performance is complicated by the fact that the internal flow is dynamic. One of the most important factors is the interaction of the explosive-driven piston with the reflected precursor shock wave. In Section 4.2.7, an expression was established for the ratio of reservoir length to driver length such that the explosively driven piston would stop as it reached the reflected shock wave. Recalling the expression for the ratio of reservoir length to driver length, one can see that it only depends on the ratio of the piston velocity to the shock velocity, which remains constant regardless of launcher scale (only a function of the driver gas and the piston velocity).

$$\frac{L_R}{L_D} = \left(\frac{1}{U_{\text{piston}}} - \frac{1}{U_S}\right)\left(\frac{1}{U_S} + \frac{1}{U_{S\text{refl}}}\right) \tag{5.3}$$

The analytical analysis thus far seems to indicate that the ideal performance of the launcher should scale well. In order to confirm this, two ideal simulations of the launcher at a 5:1 scaling were performed while keeping the non-dimensional design parameters constant. As can be seen in Figure 5–1, the resulting launcher performance is completely independent of its scale.

Although the performance of the ideal launcher scales very well, it is important to look at the scaling of non-ideal effects, which have been shown to significantly affect the performance of implosion launchers. The scaling of reservoir expansion can be paralleled to the scaling of the isentropic expansion of a gas contained in a cylinder. The relative change in pressure can be determined by the relative change in volume:

$$\frac{dP}{P} = -\gamma\frac{dV}{V} \tag{5.4}$$

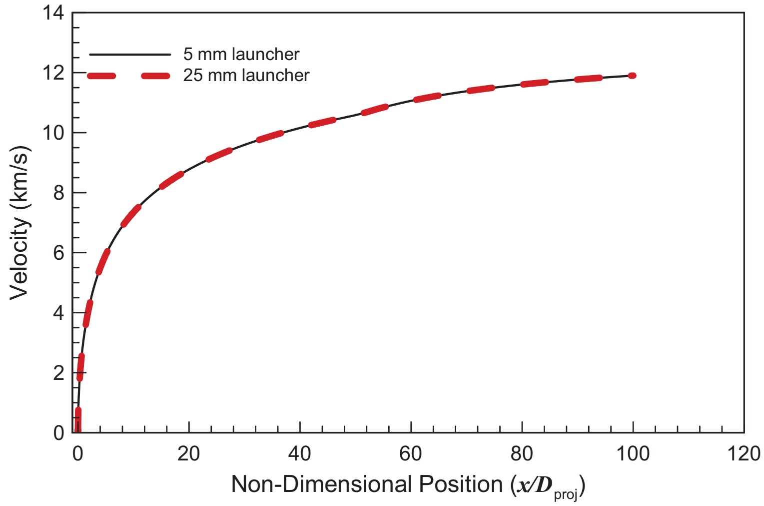

Figure 5–1: Comparison of the projectile velocity as a function of position for 5 and 25 mm for ideal implosion-driven launcher simulations

The variation in the volume of an expanding cylinder as a function of time is given by the following expression, which can be divided by its volume to give the relative differential change in volume as a function of a differential interval of time. For this analysis, it will be assumed that the radial wall velocity ($\dot{r}$) of the cylinder (or reservoir) is independent of launcher size. This assumes that the driver gas pressures are sufficiently large such that the deformation is hydrodynamic, and as a result the wall velocity will only be a function of the driver gas pressure and wall material.

$$\frac{dV}{dt} = 2\pi L r \dot{r} \tag{5.5}$$

$$\frac{dV}{V} = \pi \dot{r} \left(\frac{dt}{D_{LT}} \right) \tag{5.6}$$

As can be seen, the proportional change in the cylinder volume as a function of time is inversely proportional to its size. In order for the effect of reservoir expansion to scale with launcher size, the relative change in reservoir volume (and thus pressure) as a function of projectile velocity must be independent of launcher scale.

As can be seen in the last term of Equation 5.6, this requires that the time taken for the projectile to reach a given velocity be proportional to the launch tube diameter ($dt \propto D_{LT}dU$). As is shown in the following expression, if the effective projectile density remains constant, the projectile aerial density (kg/m^2, its resistance to acceleration) increases with the diameter of the launch tube.

$$\frac{m_{\text{proj}}}{A_{LT}} = \left(\rho_{\text{proj}} \frac{L_{\text{proj}}}{D_{LT}}\right) D_{LT} \tag{5.7}$$

By applying Newton's second law to a projectile under constant pressure, it can be seen that the acceleration of a projectile will be inversely proportional to its diameter if the effective density remains constant.

$$\frac{dU}{dt} = \frac{F}{m_{\text{proj}}} = \frac{PA_{LT}}{\rho_{\text{proj}} A_{LT} L_{\text{proj}}} = \frac{P}{\left(\rho_{\text{proj}} \frac{L_{\text{proj}}}{D_{LT}}\right) D_{LT}} \tag{5.8}$$

From this result, it can be seen that time taken for a projectile to accelerate to a given velocity will be proportional to the radius of the launcher:

$$dt = \frac{1}{P} \left(\rho_{\text{proj}} \frac{L_{\text{proj}}}{D_{LT}}\right) D_{LT} dU \tag{5.9}$$

From Equations 5.6 and 5.9, it can be seen that the proportional change in reservoir volume for a given change in projectile velocity will be independent of launcher scale. As a result of this analysis, the expansion losses are expected to be independent of launcher scaling. This can be explained by the fact that although the projectile in a larger launcher will be slower to accelerate, the relative change in the volume of the reservoir will also occur more slowly.

$$\frac{dV}{V} = \frac{\pi \dot{r}}{P} \left(\rho_{\text{proj}} \frac{L_{\text{proj}}}{D_{LT}}\right) dU \tag{5.10}$$

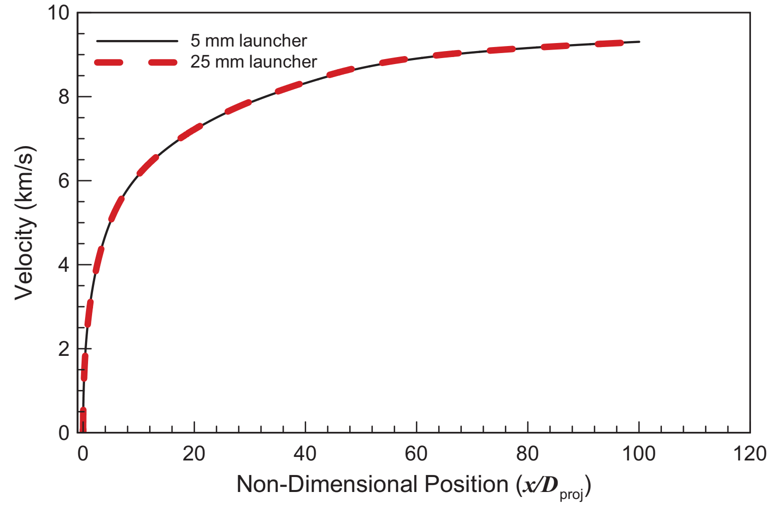

Figure 5–2: Comparison of the projectile velocity as a function of position for 5 and 25 mm for implosion-driven launcher simulations with the reservoir expansion model

It is important to note that this simple isentropic expansion model does not take into account internal ballistics consideration, including the communication time between the expanding reservoir and the projectile. For this reason, the scaling of the expansion losses has been verified using simulations with the expanding reservoir model, where the internal and external dimensions of the launcher have been varied using a 5:1 scaling. As can be seen in Figure 5–2, the simulations confirm that expansion losses are independent of launcher size.

Another important source of losses in implosion launchers is the non-ideal operation of the linear explosive driver. As has been explained in the Introduction (Section 1.3.1), the performance of linear explosive drivers (including non-ideal effects) has been shown to scale well as the size of the driver is varied. Therefore, as long as the driver length to diameter (L/D) remains constant, the losses related to driver non-ideal effects will be independent of launcher size.

It has also been shown that losses related to gas friction and heat transfer to the launcher walls can have a significant effect on performance. The magnitude of these losses depends on the surface area of the internal walls of the launch tube over which the gas is flowing. However, the resulting proportional loss of momentum and energy depends on the volume of the gas. The ratio of the volume of a cylinder over its radial surface is proportional to its radius. Therefore, as the size of a launcher increases, the relative effect of friction and heat transfer losses decreases. This can be shown by writing the expressions for friction and heat transfer of an internal cylindrical flow:

$$dU = \frac{F}{M}dt = \frac{\frac{1}{2}f\rho U^2 \pi D L}{\rho \frac{\pi D^2}{4} L}dt = \frac{1}{D}(2fU^2)dt \tag{5.11}$$

$$de = \frac{\dot{Q}}{m}dt = \frac{\frac{1}{2}f\rho U \pi D L H_\infty}{\rho \frac{\pi D^2}{4} L}dt = \frac{1}{D}(2fUH_\infty)dt \tag{5.12}$$

The effect of scaling on gas friction and heat transfer losses can be verified using the computational model. Figure 5–3 compares the velocity profile for a 0.5 cm launcher and a 2.5 cm launcher with friction and heat transfer to an expanding simulation without these losses. These two projectile sizes represent the range of launcher sizes that have been used for the majority of implosion-driven launcher experiments. As expected, the 2.5 cm launcher is less affected by the losses. The difference in performance between the two launchers is approximately 220 m/s, or 2 percent of the final projectile velocity.

It is important to remember that these simulations do not take into account the mixing of ablated wall material with the light driver gas. The resulting increase in molecular weight could have an important effect on launcher performance. Again, small launchers would be more susceptible to this effect, as its relative impact depends on the ratio of surface area to volume.

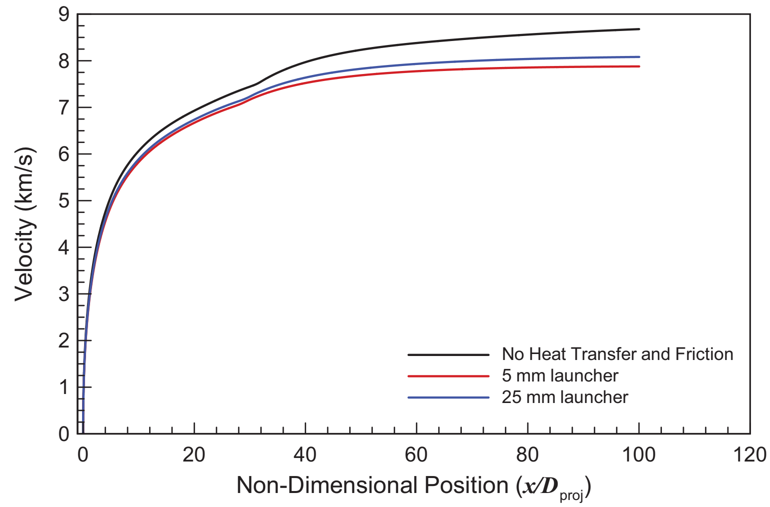

Figure 5–3: Comparison of the projectile velocity as a function of position for 5 and 25 mm for implosion-driven launcher simulations with reservoir expansion, gas friction, and heat transfer

The results from this section show that the performance of the implosion driven launcher scales well. Although experiments have never been performed to directly verify launcher scaling, launchers with similar designs and drastically different scaling have been shown to have similar performance. Therefore, the results from the parametric study of launcher design will be presented in non-dimensional form and should apply to a wide range of launcher sizes. Due to the fact that the gas friction and heat transfer losses do not scale well, the study will be performed using a 1-cm diameter projectile, which represents the mid-range of typical implosion-launcher sizes for the project.

5.2 Projectile Considerations

When designing a projectile (sabot) for a launcher, there are essentially two decisions that need to be made: its material and its thickness. The combination of material density and thickness will determine the effective density of the projectile ($\rho\left(\frac{L}{D}\right)$). The material choice will also affect the maximum driving pressure that can be applied to the projectile without damage. As will be seen, the effective density and driving pressure threshold of a projectile will have a strong influence on the performance of the launcher. The effect of varying the effective projectile density and the maximum driving pressure can readily be examined using the computational model. However, it is difficult to directly relate the material properties of a projectile to the maximum driving pressure it can sustain, given that the mechanisms for projectile failure are not well understood (see Section 4.2.5). For this reason, experimental data will be used to supplement the computational results in order to determine the merit of different projectile materials.

From ideal internal ballistics consideration, it was seen that decreasing the effective projectile density and increasing the driver fill pressure vastly improved launcher performance by increasing the rate of acceleration of the projectile and decreasing the proportional amount of driver gas energy needed to propel it. In order to maximize the velocity capability of an ideal launcher, the ratio of driver gas fill pressure over effective projectile density must be made as large as possible. Ideal implosion launchers (no losses) with the same ratio of driver fill pressure over effective projectile density will perform identically, as long as all other launcher design parameters are held constant. As a result, an increase in effective projectile density can be compensated by increasing the driver fill pressure by the same proportion. As will be seen, this is not the case in an implosion launcher when non-ideal effects are taken into account. In order to establish the optimum projectile material, it is important to determine the relative sensitivity of varying the effective projectile density and driver fill pressure on the performance of real launchers.

In an implosion launcher, minimizing the effective projectile density is critical because expansion losses increase as this parameter increases. A projectile with a

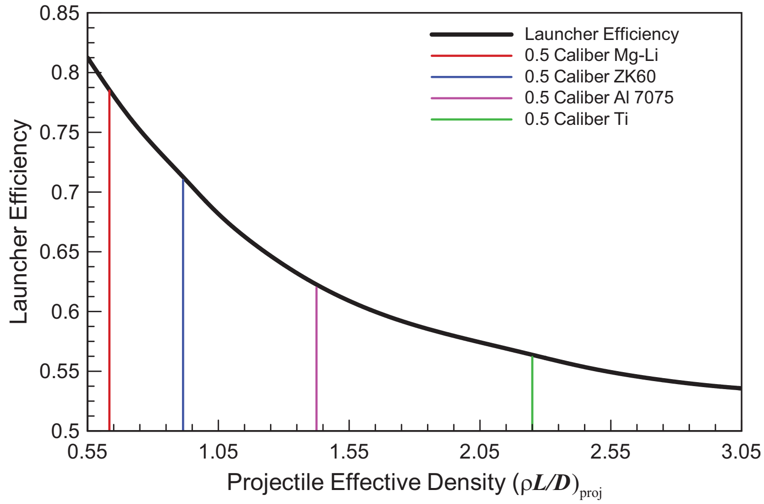

Figure 5–4: Effect of the effective density of a projectile on launcher efficiency. Lines indicating the corresponding effective density of 0.5 caliber magnesium, aluminum, and titanium projectiles have been included for reference.

higher effective density will accelerate slower, which gives more time for the reservoir to expand and increases the proportion of driver gas energy that is lost to expansion. This can be demonstrated by the computational model and expressed in the form of efficiency, which will be defined as the simulation final velocity of a launcher in which all losses (expansion, friction, driver) are taken into account, divided by the velocity result from an ideal simulation. As can be seen in Figure 5–4, increasing the effective density of the projectile significantly decreases the efficiency of the launcher. This means that even if an increase in effective projectile density is accompanied by an equal increase in pressure, the performance of the launcher will decrease. It is important to note that although the efficiency curve was obtained for a specific launcher geometry, it is expected to apply to a wide range of launcher designs. These results indicate that the velocity potential of implosion launchers will be very sensitive to the effective density of the projectile, which will likely favour the use of a thin, low density projectile.

Although the previous analysis seems to suggest that using a projectile material with a low density might be advantageous, it is still possible that a heavy projectile with a significantly higher pressure threshold may prove to be superior. In order to overcome the large decrease in launcher efficiency, an increase in effective projectile density brought about by a change in projectile material needs to be offset by a significant increase in the mass of driver gas and the maximum projectile driving pressure. Although this can readily be accomplished by increasing the initial driver gas fill pressure, it is not clear that the efficiency of the launcher will remain constant as the maximum driving pressure is increased, due to the resulting augmentation in reservoir radial expansion.

In order to verify this, the variation in the launcher efficiency as a function of maximum projectile driving pressure was determined using the computational model. The results are presented in terms of a relative efficiency (ratio of the efficiency at the given pressure divided by the efficiency at a driver fill pressure of 4 MPa). In this way, the computational results can be compared to experimental launchers having different baseline efficiencies. As can be seen in Figure 5–5, the computational model predicts that the relative efficiency is nearly constant for a wide range of maximum driving pressures, which seems to indicate that large gains can be made by increasing the driver gas fill pressure. The constant efficiency can be explained by the fact that the higher projectile acceleration offsets the fact that the reservoir is expanding faster under the larger driver gas pressures.

As can also be seen in Figure 5–5, this constant relative efficiency has not been observed in experiments. Single stage launcher experiments have shown significant diminishing returns (large reductions in efficiency) beyond maximum driving pressures of 5 GPa. This represents a driver fill pressures of approximately 4 MPa in

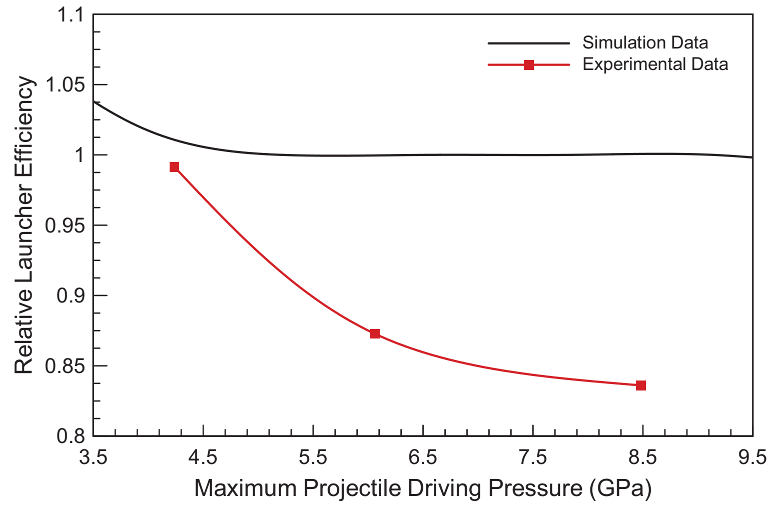

Figure 5–5: Effect of the maximum projectile driving pressure of a projectile on launcher efficiency

a typical implosion launcher (piston velocity of 7 km/s and driver to launch tube area ratio of 5). This trend can also be seen in Table 5–1, which shows four series of experiments in which increasing the maximum projectile driving pressure beyond 5 GPa resulted in little or no gains in velocity. The reason for the reductions in efficiency at higher fill pressures is not clear, but is believed to be related to reservoir failure under the large driver gas pressures. Recovered launchers from high pressure experiments have shown signs of reservoir fracture, which may have caused large quantities of driver gas to leak early in the launch cycle, leading to a significant reduction in the projectile driving pressure. It is important to note that the expansion model used in the internal ballistic solver does not take into account material failure, which may explain the discrepancy between the model and the experimental results.

It is also possible that the reduction in efficiency is caused by projectile damage during the launch cycle. Although a projectile may appear to be intact in high speed photographs, it is possible that the high driving pressure caused significant radial erosion, which allowed the driver gas to leak past the projectile. In this

Table 5–1: Summary of experiments in which launchers of similar design were fired with large differences in initial fill pressure.

Shot ID	Maximum Driving Pressure (GPa)	Velocity (km/s)	Projectile	Comments
L025	4.64	4.7	1.3 cal. Al6061	All other launcher parameters held constant
L026	5.8	4.3	1.3 cal. Al6061	
L052	4.24	7.9	0.28 cal. Al7075	All other launcher parameters held constant
L053	5.45	7.1	0.28 cal. Al7075	
L055	6.06	7.3	0.5 cal. ZK60	All other launcher parameters held constant
L056	8.48	7.5	0.5 cal. ZK60	
PI-397-8	3.98	8.0	0.5 cal. Mg-Li	All other launcher parameters held constant
PI-397-5	7.97	7.8	0.5 cal. Mg-Li	

case, it could be possible that using a stronger and stiffer material would allow gains in efficiency to be made at higher pressures. Experiments have never been performed to systematically verify the effect of projectile material on the efficiency of the launcher. Although it has been observed that plastic projectiles tend to underperform in implosion launchers, presumably due to a strength and stiffness deficiency, it is not believed that aluminum or titanium alloys would hold a significant advantage over lighter but weaker magnesium alloys in preventing the bypass of driver gas in high pressure experiments. Indeed, as was seen in Table 5–1, a similar point of diminishing returns in increasing the maximum projectile driving pressure has been observed with four different metal alloys (Al 6061, Al 7075, ZK60, Mg-Li alloy). For this reason, it is believed that the reduction in efficiency at high pressures is related to reservoir failure and cannot be reversed by the use of aluminum or titanium projectiles.

The reduction in launcher efficiency as the driver gas pressure is increased means that it is not likely that the performance of aluminum or titanium alloys is capable of matching that of much lighter magnesium alloys. ZK60 and Mg-Li projectiles have been launched intact under maximum driving pressures exceeding 7 GPa, which is well beyond the point of diminishing returns identified in experiments. In the beginning of this section, it was established that according to ideal internal ballistics, the performance of a launcher remains constant if the ratio of initial fill pressure over effective projectile density remains constant. The reductions in efficiency as fill pressure and effective projectile density are increased means that this statement is not true for real implosion launchers. As a result, even if the maximum ratio of fill pressure to effective projectile density that could be sustained by aluminum or titanium projectiles was higher than that of magnesium, the limited gains from the pressure increase would not be able to overcome the lower efficiency caused by the increase in effective density and maximum driving pressure.

The thickness of a projectile also has a direct influence on its effective density. Therefore, it is desirable to make the projectile as thin as possible, while ensuring reliable launcher performance. A thin projectile will be more susceptible to being damaged and will be more likely to tumble inside the launch tube when exposed to uneven driving forces. In keeping in mind that the eventual goal of the launcher is to perform hypervelocity impact testing, the projectile must be capable of being used as a sabot which can carry a projectile such as an aluminum sphere for orbital debris impact testing. The sabot must be sufficiently thick to ensure it can survive the stresses induced by having to propel the aluminum sphere. The minimum projectile thickness that results in reliable launcher performance must be determined experimentally. As can be seen in Table 5–2, some experiments performed on projectiles having thicknesses below 0.5 launch tube diameters have had sporadic results. Admittedly, it is not clear whether the inconsistencies are a direct result of projectile

Table 5–2: Summary of experiments in which launchers of similar design were fired with low thickness projectiles, resulting in sporadic velocity results

Shot ID	Maximum Driving Pressure (GPa)	Velocity (km/s)	Projectile	Comments
L043	4.24	6.7	0.3 cal. Al7075	Small variation in driver tamper, all other launcher parameters held constant
L046	4.24	6.0	0.3 cal. Al7075	
L047	4.24	6.4	0.3 cal. Al7075	
L052	4.24	7.9	0.28 cal. Al7075 (0.65 g)	All other launcher parameters held constant
L053	5.45	7.1	0.28 cal. Al7075 (0.65 g)	
L054	4.24	7.4	0.5 cal. ZK60 (0.53 g)	

thicknesses, or due to other factors related to the fabrication, assembly, and experimental setup of the launcher. Nonetheless, inconsistent results, combined with the fact that thin projectiles would likely not be suitable as sabots in eventual experiments, have led to the use of a projectile thickness of 0.5 calibers for the McGill project. Further study of the influence of projectile thickness on the stability and survivability of the projectile, as well as the repeatability of the launcher, would be beneficial in understanding the limit on projectile thickness and the potential gains from reduced effective projectile density.

To summarize, the maximum performance of an implosion launcher is very sensitive to the effective density of the projectile and relatively insensitive to its maximum pressure threshold. For this reason, it is critical that the effective density of the projectile be made as small as possible in order to maximize the performance of the implosion launcher. As a result, ZK60 which is the lightest readily available engineering alloy has become the material of choice for the McGill project. Efforts have also been made to reduce the effective projectile density by making the projectile as thin as possible, while ensuring consistent performance.

5.3 Driver Gas Considerations

In attempting to maximize the performance of the implosion launcher, it is important to determine whether hydrogen or helium hold an advantage as a propellant. From ideal internal ballistics considerations (pre-burnt propellant ideal gas gun), it was found that both propellants are expected to perform similarly, with helium holding a slight advantage over hydrogen. However, it has been established that the non-ideal effects in the launch cycle of the implosion launcher have an important impact on performance. These effects are likely to affect the propellants differently. Hydrogen, having a lower specific heat ratio, should be less susceptible to expansion losses, since the pressure change will be less for a given change in reservoir volume. The dissociation of hydrogen molecules prevent it from reaching very high temperatures, which means that heat transfer losses and the ablation of launcher wall material into the driver gas will be less severe. The relatively strong real gas effects present in hydrogen launchers may also affect the comparison. As was seen in Section 3.4, in the early launch cycle, the density of hydrogen is such that intermolecular repulsive forces increase the pressure of the gas well beyond the values predicted by the ideal gas law.

The computational model can be used to directly compare the performance of both propellants. Simulations were performed where helium and hydrogen launchers with the same design parameters (driver geometry, projectile, reservoir geometry) were directly compared. The driver fill pressure for both gases was chosen such that both launchers would have the same maximum projectile driving pressure. For this comparison the real gas model based on the SESAME database is used. The expanding model and the heat transfer and gas friction model are also included. The simulation does not take into account driver losses, due to the fact that there

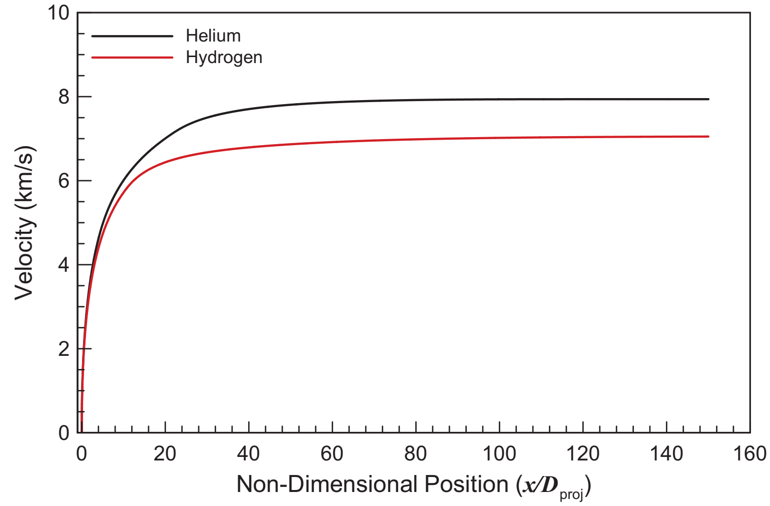

Figure 5–6: Comparison of the projectile velocity profile for a helium and hydrogen launcher. The simulations include the reservoir expansion model, gas friction/heat transfer losses, and the SESAME equation of state model. The launcher dimensions are: $D_{LT} = 10$ mm, $D_D = \sqrt{5}D_{LT}$, $L_D = 30D_D$, $U_D = 7$ km/s, (Gas = 4MPa He, $L_R = 0.18L_D$) or (Gas = 5.4MPa H_2, $L_R = 0.12L_D$), $L_{\text{offset}} = 3D_{LT}$, Proj = $0.5(L/D)$

is no available data for hydrogen drivers. It is also important to re-iterate that the simulations do not take into account the mixing of ablated launcher wall material with the driver gas. Figures 5–6 and 5–7 show the resulting projectile velocity and driving pressure profiles for the simulation. As can be seen, the hydrogen launcher appears to perform significantly worse than the helium launcher. Despite the fact that the hydrogen propellant should be less affected by expansion and heat transfer losses, its driving pressure decays more rapidly than the helium launcher. This is caused by two main factors: real gas effects and lower driver gas mass.

As can be seen in Figure 5–8, which compares the decay of the driving pressure in a hydrogen launcher for simulations with the ideal gas and SESAME equations of state, the pressure decays more rapidly in the simulation with the real gas model. The large initial decay in the driving pressure during the real gas simulation can be attributed to the fact that as the gas initially expands, its density is rapidly reduced,

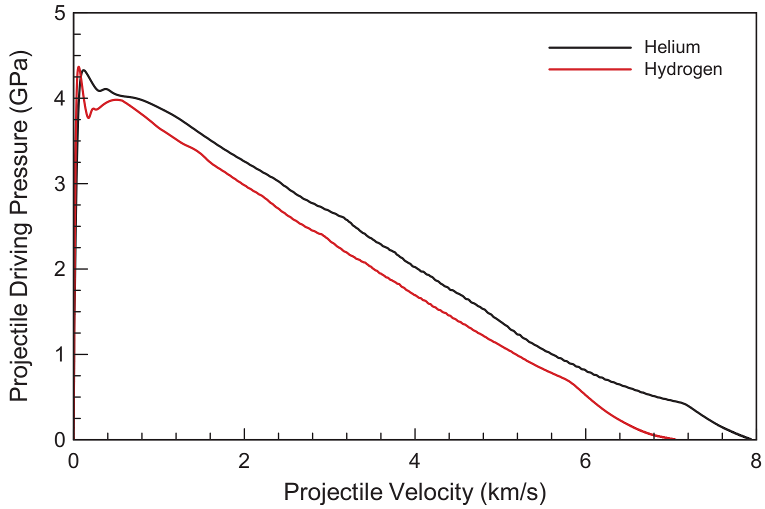

Figure 5–7: Comparison of the projectile base pressure decay as a function of velocity for a helium and hydrogen launcher. The simulations include the reservoir expansion model, gas friction/heat transfer losses, and the SESAME equation of state model. The launcher dimensions are: $D_{LT} = 10$ mm, $D_D = \sqrt{5}D_{LT}$, $L_D = 30D_D$, $U_D = 7$ km/s, (Gas = 4MPa He, $L_R = 0.18L_D$) or (Gas = 5.4MPa H_2, $L_R = 0.12L_D$), $L_{\text{offset}} = 3D_{LT}$, Proj = $0.5(L/D)$

which attenuates the strong intermolecular repulsive forces responsible for the higher initial pressure. Although the pressure rise caused by real gas effects can offer an advantage in other types of launchers, notably the two-stage light gas gun, it can be seen as a disadvantage in the implosion launcher because it results in faster propellant pressure decay during expansion. As a result of real gas effects, the average driving pressure in the helium launcher is higher than in a hydrogen launcher for matching maximum pressures.

The fact that real gas effects increase the maximum driving pressure of hydrogen launchers means that the driver fill pressure in the hydrogen launcher must be significantly reduced, relative to the ideal calculations performed in Section 3.4, to match the maximum projectile driving pressure in the helium launcher. Although ideal calculations predicted that both launchers would have a similar G/M, real gas effects cause hydrogen launchers to have a significantly smaller propellant mass than

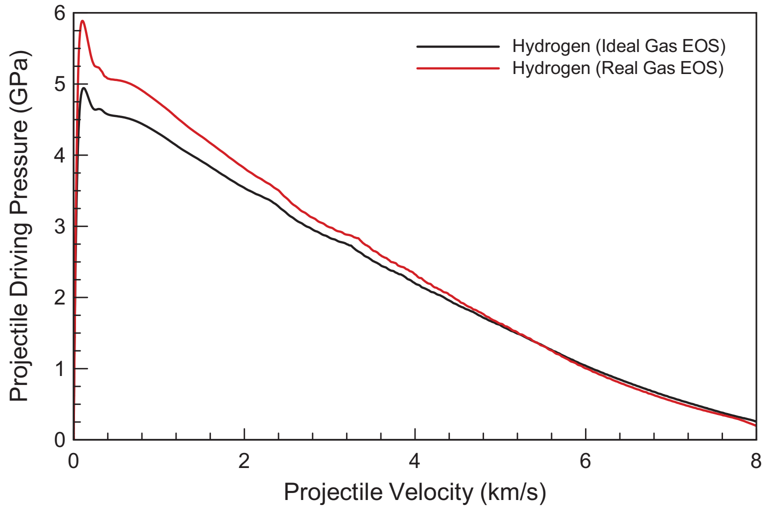

Figure 5–8: Comparison of the projectile base pressure decay as a function of velocity for a hydrogen launcher with a SESAME equation of state and an ideal gas equation of state. The simulations include the reservoir expansion model and gas friction/heat transfer losses. The launcher dimensions are: $D_{LT} = 10$ mm, $D_D = \sqrt{5}D_{LT}$, $L_D = 30D_D$, $U_D = 7$ km/s, Gas = 5.4MPa H_2, $L_R = 0.12L_D$, $L_{\text{offset}} = 3D_{LT}$, Proj = $0.5(L/D)$

an equivalent helium launcher with the same maximum driving pressure. This is an important factor in the apparent difference between hydrogen and helium propellants in the simulation. Figure 5–9 presents the results from a simulation where the driver length of the hydrogen launcher was increased to match the G/M of the helium launcher. As can be seen, the performance is nearly equal.

The computational analysis performed above appears to indicate that the performance of helium should be superior to that of hydrogen when launchers are compared directly. It was also seen that the performance is expected to be quite similar if the driver volume of the hydrogen launcher is increased to match the G/M of the helium launcher. Admittedly, the analysis is partially incomplete, since it neglects two important aspects of real implosion launchers: the non-ideal driver operation and the effect of the mixing of ablated wall material with the driver gas during the launch

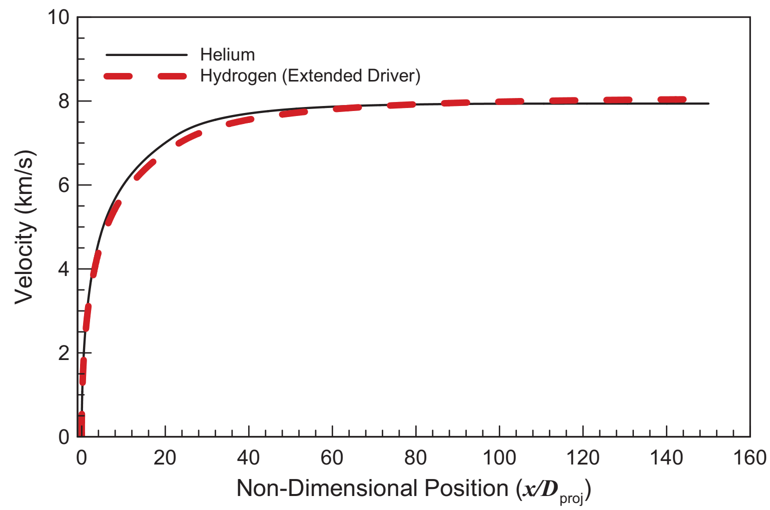

Figure 5–9: Comparison of the projectile velocity profile for a helium and hydrogen launcher having the same G/M. The simulations include the reservoir expansion model, gas friction/heat transfer losses, and the SESAME equation of state model. The launcher dimensions are: $D_{LT} = 10$ mm, $D_D = \sqrt{5}D_{LT}$, $U_D = 7$ km/s, (Gas = 4MPa He, $L_R = 0.18L_D$, $L_D = 30D_D$) or (Gas = 5.4MPa H_2, $L_R = 0.12L_D$, $L_D = 44.4D_D$), $L_{\text{offset}} = 3D_{LT}$, Proj = $0.5(L/D)$

cycle. In order to confirm the results from the analysis, direct experimental comparisons of hydrogen and helium launchers can be used. Table 5–3 shows a summary of two different experimental comparisons. The driver fill pressures were adjusted to give similar maximum driving pressures and the reservoir length was adjusted to compensate for the smaller precursor shock wave velocity in the hydrogen driver. As can be seen, helium launchers appear to hold a significant advantage, which confirms the results obtained from the computational analysis.

The experiments reported in Table 5–3 can also serve to estimate the effect of ablation losses on the comparison between both propellants. If ablation had a significant effect on performance, one would expect that the difference between the predicted velocity from the computational model, which does not include ablation effects, and the experimental results would be greater (more overpredicted) for the helium launcher, due to the higher propellant temperature. This does not appear to

Table 5–3: Summary of implosion launcher experiments comparing the performance of helium and hydrogen as driver gases

<table>
<tr><th>Shot ID</th><th>Driver Gas</th><th>$P_{\max}$ (GPa)</th><th>Velocity (km/s)</th><th>Simulation Velocity (km/s)</th><th>Percent Error</th><th>G/M</th><th>Comments</th></tr>
<tr><td>L040</td><td>Helium</td><td>3.45</td><td>6.8</td><td>8.1</td><td>19%</td><td>2.37</td><td rowspan="2">Reservoir length adjusted for driver gas, other launcher parameters constant</td></tr>
<tr><td>L041</td><td>Hydrogen</td><td>3.89</td><td>5.66</td><td>7.22</td><td>28%</td><td>1.83</td></tr>
<tr><td>L043</td><td>Helium</td><td>3.62</td><td>6.7</td><td>7.8</td><td>16%</td><td>1.97</td><td rowspan="2">Reservoir length adjusted for driver gas, other launcher parameters constant</td></tr>
<tr><td>L044</td><td>Hydrogen</td><td>4.06</td><td>6.0</td><td>7.2</td><td>20%</td><td>1.52</td></tr>
</table>

be the case. As can be seen, the difference between the computational and experimental performance is nearly the same for both helium and hydrogen launchers. This seems to indicate that ablation may not be an important factor in the comparison between the propellants.

Both the computational and experimental results indicate that when comparing identical launcher designs, helium appears to be the superior propellant. It also appears that ablation losses do not have a significant effect on the comparative performance of both driver gasses. The computational model appears to indicate that the performance of hydrogen could match that of helium if the launcher G/M was held constant rather than using the same driver geometry for both launchers. Nonetheless, it appears unlikely that the performance of a hydrogen launcher will offer significant benefits over helium. As a result, helium remains the propellant of choice for the McGill project.

5.4 Explosively Driven Piston Velocity

The velocity of the explosive piston in the driver determines the strength of the shock wave which compresses the driver gas. By increasing the piston velocity, the temperature and speed of sound of the driver gas can be dramatically increased. As was seen in Section 4.2.2, the speed of sound of the driver gas determines the rate at which the projectile driving pressure decays. Therefore, increasing the speed of sound can help maintain a high driving pressure on the projectile and significantly improve launcher performance.

The piston velocity in the driver is determined by the detonation velocity of the explosive. Typical high-explosive detonation velocities range between 6 and 9 km/s. However, it is also possible to use phase velocity techniques to increase the apparent detonation velocity of the explosive. These techniques, which rely on tilting the detonation wave to increase the apparent velocity of the explosively driven piston have been used to operate linear explosive drivers at effective piston velocities of up to 16 km/s [24, 23]. Explosive phase velocity is explained in further detail in Appendix D. It should be noted that the performance of phased linear explosive drivers falls significantly below that of typical drivers, presumably due to the implosion geometry. Beyond phase velocities of 12 km/s, where the phased detonation wave becomes very oblique, the operation of the driver departs significantly from that of typical linear explosive drivers. For this reason, the analysis will focus on explosive driven piston velocities ranging from 6 to 12 km/s.

The computational model can readily be used to observe the effect of varying the driver piston velocity on the performance of the implosion launcher. Figure 5–10 shows the predicted projectile velocity as a function of the driver piston velocity for two different driver lengths. The initial driver gas fill pressure was adjusted in order to maintain a constant maximum projectile driving pressure. As a result, launchers with higher piston velocities have a lower driver gas mass to projectile mass ratio (G/M). The real gas equation of state, expansion model, and heat transfer and gas

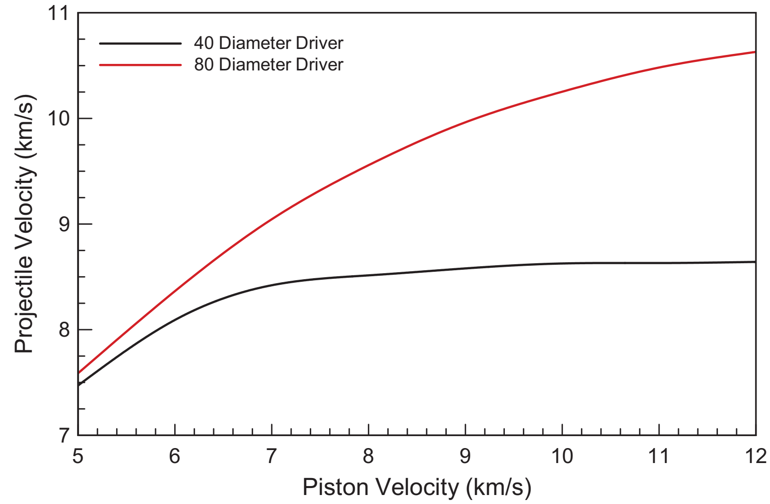

Figure 5–10: Predicted projectile velocity as a function of explosively driven piston velocity. Launchers having two different driver lengths are compared. The simulations include the reservoir expansion model, gas friction/heat transfer losses, and the non-ideal pump tube model. The launcher dimensions are: $D_{LT} = 10$ mm, $D_D = \sqrt{5}D_{LT}$, Gas=He, $L_R = 0.2L_D$, $L_{\text{offset}} = 3D_{LT}$, Proj $= 0.5(L/D)$

friction models were used in the simulations. The driver was assumed to operate ideally, given that there is no data available for higher explosively driven piston velocities and limited data for phased drivers.

As can be seen in Figure 5–10, the driver piston velocity appears to have very little influence on the performance of the launcher for the shorter driver. However, when the driver length is increased, there is a significant increase in launcher performance as the piston velocity is increased. In the simulations with the shorter driver, the performance of the launchers with higher piston velocities does not improve because they are limited by their G/M, which is much lower due to the lower fill pressure. When the G/M is increased by increasing the driver length, the performance of launchers with high piston velocities is dramatically increased by the fact that sufficient driver gas is available for the launchers to reach their higher theoretical potential. The projectile velocity of the slower drivers is only marginally increased

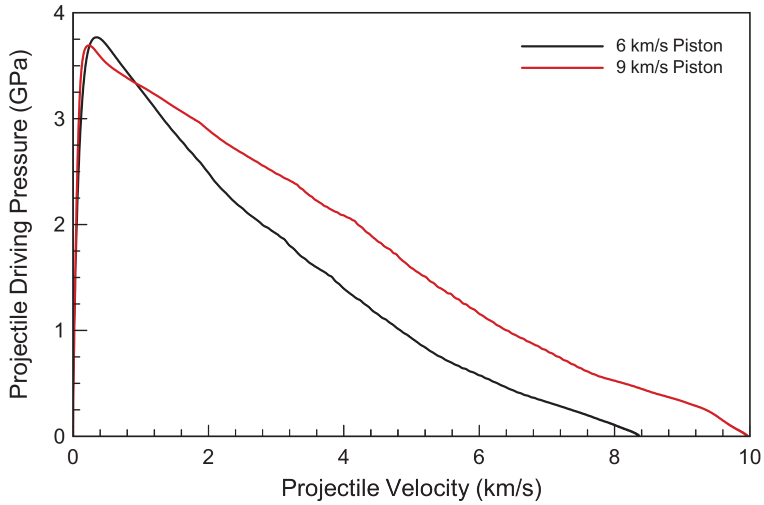

Figure 5–11: Comparison of the projectile driving pressure decay in launchers having different explosively driven piston velocities. The simulations include the reservoir expansion model, gas friction/heat transfer losses, and the non-ideal pump tube model. The launcher dimensions are: $D_{LT} = 10$ mm, $D_D = \sqrt{5}D_{LT}$, $L_D = 60D_D$, Gas=He, $L_R = 0.2L_D$, $L_{\text{offset}} = 3D_{LT}$, Proj $= 0.5(L/D)$

because of diminishing returns on increasing the G/M. The effect of G/M will be explored in detail in Section 5.5. The benefit of increasing the speed of sound of the driver gas on the launch cycle can be seen in Figure 5–11, which compares the decay of the projectile driving pressure for a launcher with a piston velocity of 6 and 9 km/s. It is clear that the driving pressure decays significantly slower for the launcher with a 9 km/s piston.

As can be seen, there are significant gains to be made in launcher performance by increasing the driver piston velocity as long as sufficient driver gas mass can be provided to the launcher. It should be noted that by increasing the temperature of the driver gas, there is likely to be significantly more mixing of ablated launcher wall material with the driver gas. These losses are not taken into account in the computational model. However, from Figure 5–10, it appears likely that the large increase in launcher performance will outweigh the increase in ablation losses. It is therefore recommended that an explosive with the highest available detonation velocity be used in the driver.

The question remains as to whether there is an advantage to using a phased linear explosive driver to compress the driver gas in the implosion launcher. In order to observe performance improvements at high piston velocities (> 9 km/s), a large column of driver gas must be generated, due to the low initial propellant density needed to maintain a reasonable maximum driving pressure. Figure 5–12 compares the evolution of the standoff distance between the explosive driven piston and the precursor shock wave as a function of position for a typical driver and a phased driver. As can be seen, the performance of the phased driver falls well short of the standard one, which limits the amount of driver gas that can be supplied to the launcher. While the precursor shock wave velocity in the standard driver remains close to ideal for a long period of time (>50 L/D) this is not the case for the phased driver. For example, the precursor shock wave velocity in a 12 km/s phased driver is similar to what would be expected in an ideal 10 km/s driver. Although the lower shock velocity reduces the performance gains that should be expected from phased drivers, they may still hold a significant advantage over the standard 7 km/s driver currently being used in experiments.

As a result of the low initial driver pressure and the lower standoff between the precursor shock wave and the explosively driven piston, a launcher with a phased driver would require a large area ratio between the driver and the launch tube in order to supply the necessary amount of driver gas. Preliminary calculations indicate that an area ratio of 15 should supply sufficient driver gas to the launch cycle without having to exceed a maximum projectile driving pressure of 5 GPa. It appears possible that with a driver of this size, a launcher with a phased driver could outperform a

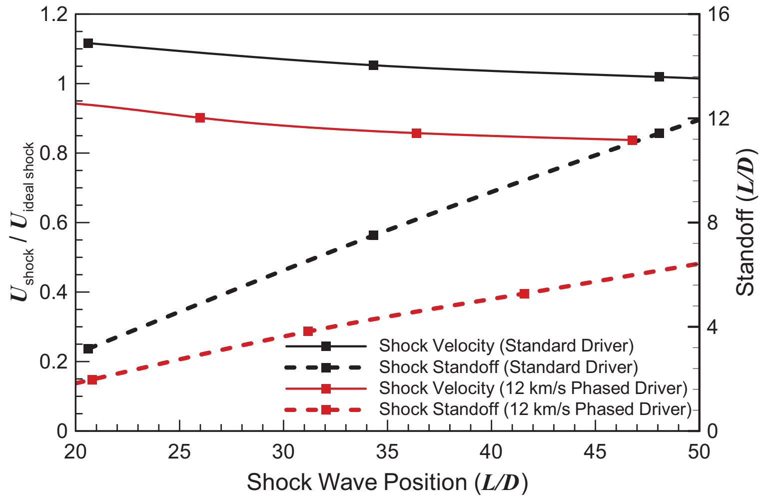

Figure 5–12: Comparison of the precursor shock wave velocity and standoff between the precursor shock wave and the explosively driven piston for phased and non-phased drivers

standard launcher by more than 1 km/s. It should be noted that it may be possible to improve the design of the phased driver such that the precursor shock wave velocity is much closer to ideal predictions. In this case, a phased driver could hold an even greater advantage over a standard driver and would not require such a large area ratio to provide sufficient driver gas mass.

5.5 Driver Geometry

The length and cross sectional area of the driver have an important influence on the launch cycle of the implosion driven launcher. As was discussed in Section 4.2.3, the gas mass to projectile mass ratio (G/M), determined by the volume of the driver, and the area ratio between driver and launch tube (chambrage) are important parameters in maximizing the velocity potential of the launcher. It is expected that increasing the cross-sectional area and length of the driver will improve the performance of the launcher. However, the occurrence of non-ideal effects in long drivers and the diminishing returns on increasing the G/M mean that there will be a point where the performance of the launcher no longer benefits from increasing the driver length. Similarly, diminishing returns on the benefit of chambrage and G/M will limit the gains to be made from increasing the cross sectional area of the driver relative to the launch tube. It is important to remember that the driver length and area have an important influence on the cost of the launcher and the size of the facility required to perform experiments. For this reason, efforts should be made to ensure the use of an efficient driver size which maximizes performance without significantly increasing the cost of the launcher.

As a preliminary exercise, it is interesting to observe the effect of the driver length and the driver to launch tube area ratio on the launcher G/M, which is shown in Figure 5–13. The real (non-ideal) performance of the driver is considered, which explains why the G/M does not increase linearly with driver length. The driver fill pressure has been adjusted such that the maximum projectile driving pressure would remain constant, regardless of the area ratio (compensates for shock wave focusing, see Section 4.2.4). As can be seen, the G/M is very sensitive to the area ratio, and relatively insensitive to the driver length. As a result, the analysis of driver geometry will likely favour a relatively short driver which operates nearly ideally, with a relatively large area ratio. While this analytical analysis is insightful in observing the sensitivity of the launcher G/M to the reservoir geometry, complete launcher simulations are needed to identify the optimum driver length and the point of diminishing returns on the area ratio.

The effect of driver geometry on the launch cycle can readily be verified using the computational model. A study was performed in which the driver length to diameter ratio was varied for a variety of driver to launch tube area ratios. The initial driver fill pressure was varied to ensure that the maximum projectile driving pressure was held constant, despite the variation in the launcher chambrage and driver length.

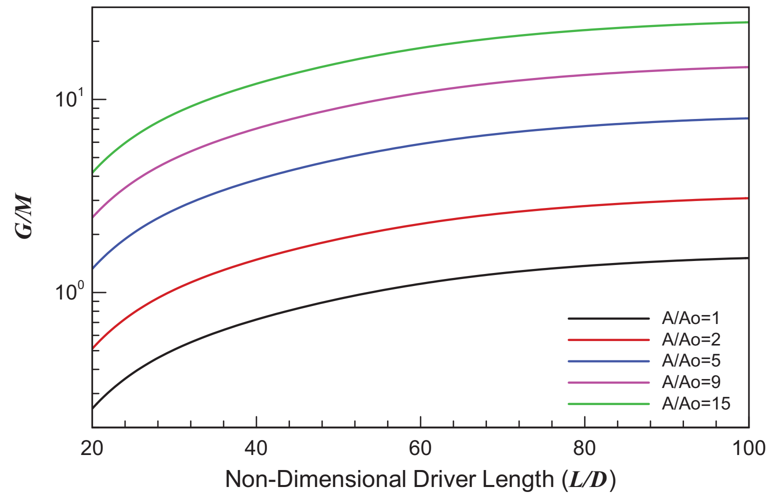

Figure 5–13: Variation in the gas mass to projectile mass ratio of an implosion launcher as a function of the area ratio and length of the driver

The simulations included the expanding model, non-ideal driver effects, and the gas friction and heat transfer model. The result of the study can be seen in Figure 5–14. As can be seen, initially there are large gains to be made from increasing the driver length and area ratio of the launcher. However, beyond driver lengths of 40 diameters and an area ratio of 5, the benefits from increasing the size of the driver appear to be limited. This is the point where it becomes apparent the launcher G/M is sufficiently large, and a further increase in driver size is not likely to significantly improve performance. It appears that there are slight gains to be made beyond this driver size, especially with regards to increasing the area ratio. However, little experimental data exists for launchers having area ratios greater than 5 to confirm these findings.

The driver geometry analysis essentially identifies a minimum driver length and diameter for a given launcher to perform adequately. This analysis was performed assuming a 0.5 caliber ZK60 projectile was launcher with a maximum driving pressure of approximately 5 GPa and a driver piston velocity of 7 km/s. It is important to note

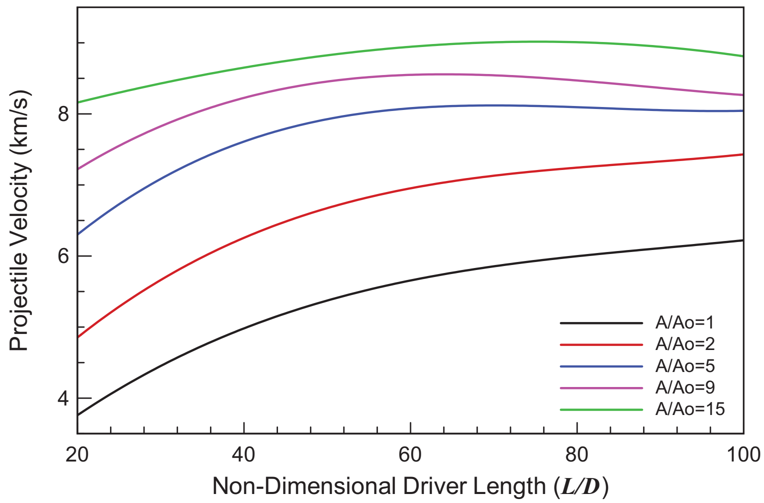

Figure 5–14: Variation in the predicted projectile velocity of an implosion launcher as a function of the area ratio and length of the driver. The simulations include the reservoir expansion model, gas friction/heat transfer losses, and the non-ideal pump tube model. The launcher dimensions are: $D_{LT} = 10$ mm, $D_D = \sqrt{5}D_{LT}$, $L_D = 40D_D$, $U_D = 7$ km/s, Gas = 4MPa He, $L_R = 0.2L_D$, $L_{\text{offset}} = 3D_{LT}$, Proj = $0.5(L/D)$

that the results of this analysis would be slightly different if the previous parameters were changed. Increasing the effective density of the projectile or the driver piston velocity would cause a decrease in the G/M ratio, which would favour a larger driver. The inverse would be true if the maximum projectile driving pressure was increased. If the results from the computational analysis are compared to those from the analytical analysis, it appears that the point of diminishing returns on launcher performance occurs at a G/M of approximately 3.5. If a full analysis cannot be completed for a launcher, a good rule of thumb would be to choose a driver length of 40 diameters and a driver to launch tube area ratio that results in a launcher G/M of at least 3.5. This should also provide a good guideline to follow in determining whether an advantage can be obtained from increasing the piston velocity of the driver. If a G/M of 3.5 cannot be reached without exceeding the driver size and

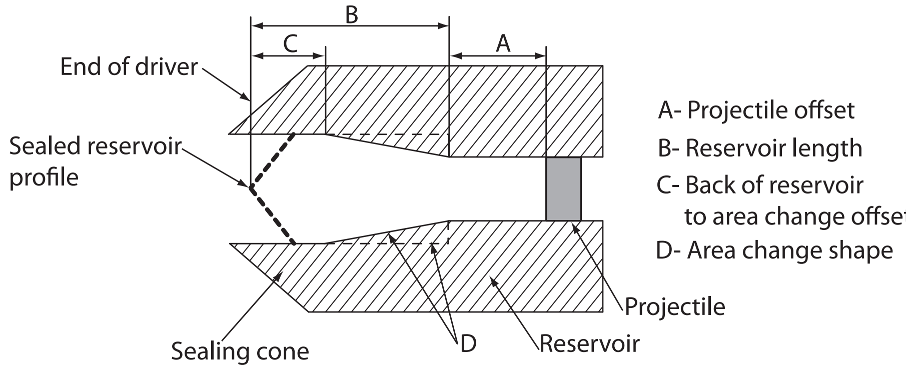

Figure 5–15: Schematic of the definition of reservoir length in an implosion-driven launcher.

maximum driving pressure limitations of the launcher for a given piston velocity, then the gains from an increase in driver piston velocity will be limited.

5.6 Reservoir Geometry

In attempting to maximize the performance of the implosion launcher, a number of design decisions need to be made regarding the reservoir, which is the interface between the driver and the launch tube. This section will look at the effect of varying the shape of the area change section, the length of the reservoir section, the offset between the projectile and the area change section, and the offset between the back of the reservoir (end of the driver) and the area change section. These design parameters are illustrated in Figure 5–15.

5.6.1 Shape of Area Change Section

The shape of the area change section (sharp or tapered) can have a significant effect on the flow field inside the implosion driven launcher. Unfortunately, a one-dimensional internal ballistics solver is limited in its ability to simulate the effect of changing the shape of the reservoir. Qualitatively, the main disadvantage to using an abrupt area change section is that the flow of driver gas is likely to be strongly disturbed, which may lead to flow losses, uneven projectile loading, and large quantities of ablation as the flow passes around the sharp corners. On the other hand, an abrupt area change section may offer an advantage early in the launch cycle due to chambrage effects. In a chambered launcher the expansion waves emanating from the projectile are reflected from the reservoir as compression waves. This gasdynamic effect is stronger in a sharp area change because the expansion wave meets the nearly stagnant reservoir gas. It is also important to consider the fact that an abrupt area change will not focus the precursor shockwave, and will therefore require a larger driver gas fill pressure to reach similar maximum projectile driving pressures. This is not seen as an advantage or disadvantage, but rather a fact to keep in mind when comparing launchers having different area change geometries.

Table 5–4 shows two experiments in which abrupt and gradual area changes were directly compared. As can be seen, the driver gas fill pressure was held constant, which means that the maximum projectile driving pressure will be lower in the abrupt area change launchers. There appears to be little difference in the launcher performance for the high pressure experiments, but a notable difference in performance for the low pressure experiments. The large difference in the low pressure experiments could be caused by the fact that the maximum driving pressure on the projectile is significantly lower for the direct area change. While this may have little effect on the high pressure launchers, where expansion and fracture of the reservoir play a dominant role (see Section 5.2), it may have an important impact on the low pressure launchers. The effect of area change geometry on launcher performance remains unclear because there are no experiments directly relating the performance of launchers with the same maximum projectile driving pressure. However, it appears improbable that there are large gains to be made from changing the geometry of the area change section.

Table 5–4: Summary of experiments in which the shape of the area change section was varied

Shot ID	Area Change Shape	Maximum Driving Pressure (GPa)	Velocity (km/s)	Comments
L043	Gradual	4.24	6.7	All other launcher parameters held constant
L048	Sharp	1.92	4.5	
PI-397-5	Gradual	7.97	7.8	All other launcher parameters held constant
PI-397-2	Sharp	3.87	8.3	

In practice, the choice of area change geometry is dictated by the fact that the performance of the launcher can be significantly improved by surrounding the reservoir with a layer of explosives to provide confinement, as will be discussed in Section 6.1. In order to ensure that the reservoir implosion does not cut off the flow of driver gas to the launch tube, a very gradual area change section is typically used in the launcher.

5.6.2 Projectile Offset from Area Change Section

The position of the projectile relative to the area change section has an important influence on chambrage effects, which help maintain a high base pressure on the projectile. Typically, the initial projectile position would be next to the end of the area change, in order to maximize the benefits from chambrage. However, during the Physics International project, it was observed that placing the projectile less than three launch tube diameters from the end of the area change section could lead to severe damage. This is not a problem for typical launchers, where the flow is typically nearly stagnant before the projectile begins to accelerate. However, in the implosion launcher, the driver gas has a large flow velocity (nearly equal to the piston velocity) as the precursor shock wave passes through the area change section. It is possible that the flow becomes non-uniform as it passes through the area change section. The stagnation of an uneven flow against the projectile could potentially induce damage.

The convention of placing the projectile 3 launch tube diameters after the area change section was a result of an experimental and computational study performed by Physics International [38]. This convention has also been adopted for the McGill launchers. However, it is important to note that Physics International never experimentally verified the effect of projectile offset in launchers with a gradual area change. For this reason, it remains of interest to verify if it is possible that significant performance gains can be made by reducing the projectile offset from the area change section. The one-dimensional internal ballistics solver can be used to determine the possible benefit from placing the projectile closer to the chambrage plane. Figure 5–16 shows the variation in projectile velocity as a function of the initial offset between the projectile and the area change section. As can be seen, there are moderate gains (<0.5 km/s) to be made from placing the projectile closer to the area change section. The analysis was performed for a launcher having a gradual area change section with a $5°$ taper and a driver to launch tube area ratio of 5, which represents a typical implosion launcher. The simulations included reservoir expansion, non-ideal driver effects, and gas friction and heat transfer losses. Although small performance gains may be possible, it does not appear to be worthwhile to attempt to reduce the current projectile offset due to the likelihood of affecting projectile survivability.

5.6.3 Reservoir Length

As was explained in Section 4.2.7, the length of the reservoir section has an important influence on the interaction between the explosively driven piston and the reservoir driver gas which has been stagnated by the reflected shock wave. A general guideline was established where the ratio of reservoir length to driver length should be chosen such that the piston reaches the end of the driver as it meets the reflected shock wave. In a constant area helium launcher, this represents a reservoir length

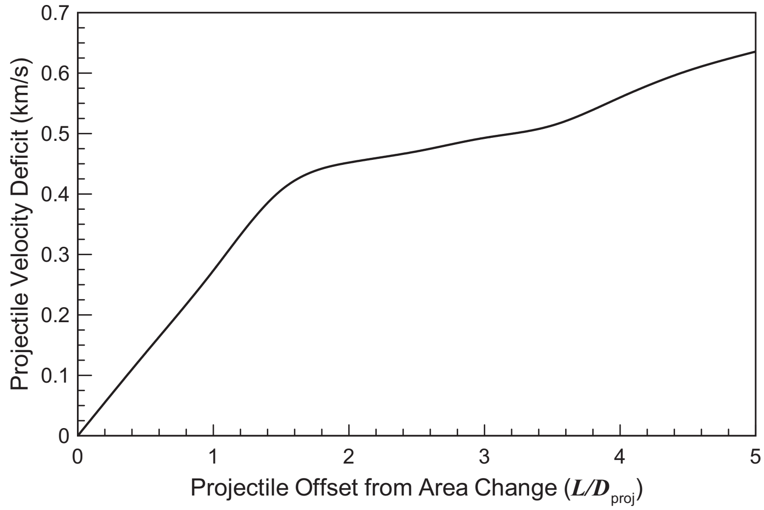

Figure 5–16: Variation in the predicted projectile velocity of an implosion launcher as a function of the offset between the area change section and the projectile. The simulations include the reservoir expansion model, gas friction/heat transfer losses, and the non-ideal pump tube model. The launcher dimensions are: $D_{LT} = 10$ mm, $D_D = \sqrt{5}D_{LT}$, $L_D = 40D_D$, $U_D = 7$ km/s, Gas = 4MPa He, $L_R = 0.2L_D$, Proj = $0.5(L/D)$

equivalent to approximately 10 percent of the driver length. This guideline varies slightly for chambered launchers, where the precursor shock wave is accelerated as it passes through the gradual area change section

The computational analysis thus far has focused on launchers with long reservoir lengths, where the explosively driven piston is stopped before it meets the stagnated reservoir driver gas. This has been done to ensure that the effect of reservoir length did not influence the phenomenon being studied. However, in attempting to maximize the performance of the launcher, there may be significant gains to be made by allowing the piston to travel further into the reservoir and recompress the nearly quiescent driver gas. Figure 5–17 shows the projectile driving pressure profile for two launchers with different reservoir lengths. As can be seen, the supplemental compression of the driver gas in launchers with short reservoirs can lead to a second spike in the projectile driving pressure. Simulations have shown that this spike, referred to

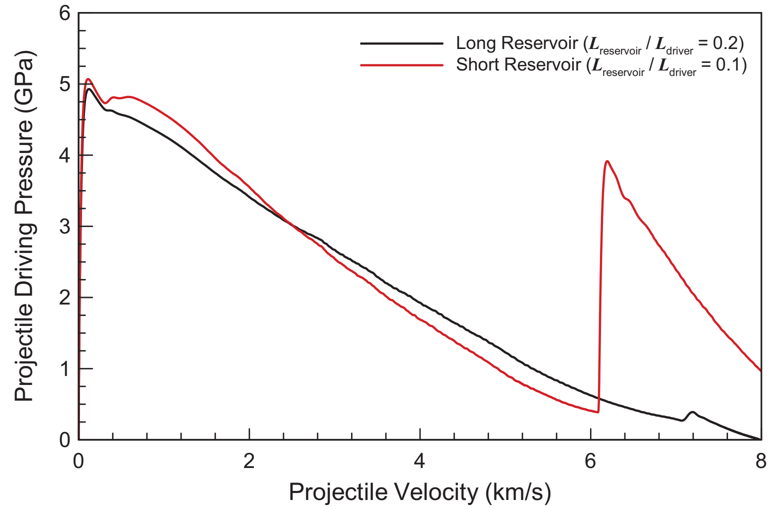

Figure 5–17: Comparison of the evolution of the projectile driving pressure in implosion launchers having significantly different reservoir lengths. The simulations include the reservoir expansion model, gas friction/heat transfer losses, and the non-ideal pump tube model. The launcher dimensions are: $D_{LT} = 10$ mm, $D_D = \sqrt{5}D_{LT}$, $L_D = 40D_D$, $U_D = 7$ km/s, Gas = 4MPa He, $L_{\text{offset}} = 3D_{LT}$, Proj = $0.5(L/D)$

as the second shock reflection, can significantly increase the average driving pressure and final velocity of a launcher. The level of reservoir gas compression is principally influenced by two reservoir design parameters: the ratio of reservoir length to driver length, and the distance between the end of the driver and the beginning of the area change section. By reducing the ratio of reservoir length to driver length, the piston is allowed to travel further into the reservoir, which further compresses the driver gas. Reducing the offset between the driver and the area change section, which is equivalent to changing the internal taper angle of the reservoir, can also increase the compression of driver gas by reducing the volume of the reservoir.

The computational model can be used to determine the sensitivity of projectile velocity to the ratio of reservoir to driver length and the offset between the end of the driver and the area change section. A number of computational simulations were performed in which the reservoir length and area change offset of the launcher

Table 5–5: Summary of experiments in which the offset between the end of the explosively driven piston and the beginning of the area change section was varied

Shot ID	Area Change Offset (diameters)	Velocity (km/s)	Comments
L043	0	6.7	All other launcher
L049	2.5	5.85	parameters held constant

were varied while keeping all other design parameters constant. The simulations included the expansion model, non-ideal pump tube behavior, and gas friction and heat transfer. The simulations were performed using a driver length of 40 diameters, a driver to launch tube area ratio of 5, a maximum projectile driving pressure of 5 GPa, and a 0.5 caliber ZK60 projectile. Figure 5–18 shows the resulting profiles of projectile velocity as a function of the reservoir length to driver length ratio. Also shown in Figure 5–18 is the maximum driver gas pressure against the explosively-driven piston. As expected, further compressing the driver gas, either by decreasing the reservoir to driver length ratio or the offset between the driver and the area change section, leads to a significant increase in projectile velocity. However, this also leads to large increases in the maximum pressure against the explosively driven piston.

The effect of varying the offset between the driver and the area change section has been observed in experiments. As can be seen in Table 5–5, an increase of 2.5 diameters in the offset between the end of the driver and the area change section led to a velocity deficit of 0.85 km/s, which is similar to what has been observed in the computational analysis.

The results from this analysis appear to indicate that there are large performance gains to be made by reducing the reservoir length to driver length ratio and the offset between the end of the driver and the area change section. However, realizing these gains in experiments requires that the explosively driven piston be able to

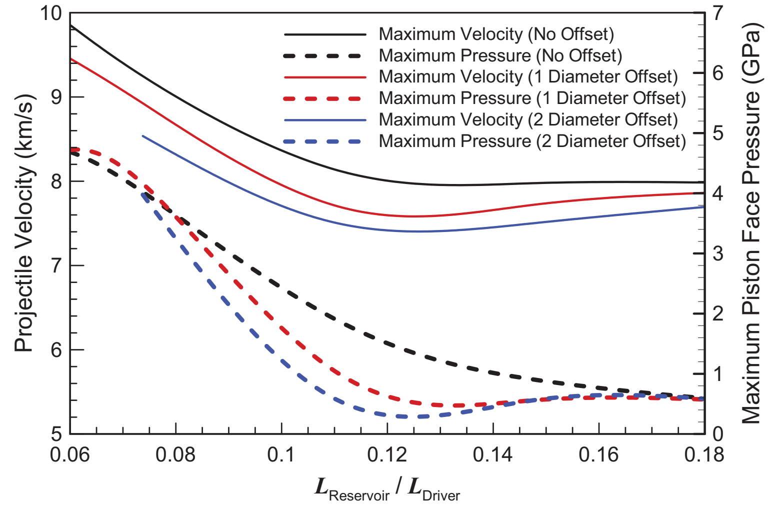

Figure 5–18: Variation in the predicted projectile velocity of an implosion launcher as a function of the reservoir length. The effect of the reservoir length on the maximum pressure against the explosively driven piston is also shown. The simulations include the reservoir expansion model, gas friction/heat transfer losses, and the non-ideal pump tube model. The launcher dimensions are: D_{LT} = 10 mm, $D_D = \sqrt{5}D_{LT}$, $L_D = 40D_D$, U_D = 7 km/s, Gas = 4MPa He, $L_{\text{offset}} = 3D_{LT}$, Proj = 0.5($L/D$)

compress the driver gas to pressures comparable to the detonation pressure of the explosive. Experiments reported by Szirti [34] have shown that the final section of the driver from launchers with very small reservoir length to driver length ratios can be interrupted by the high pressure gas. As a result, such launchers showed a decrease in performance rather than an improvement, likely due to the fact that the interruption of the explosively driven piston prevented the further compression of the gas and lead to large losses of driver gas. Attempts to operate linear explosive drivers at high pressures, reported by Serge et al. [33], identified pressure limit of approximately 1 GPa, beyond which the device can no longer drive a precursor shock wave. According to the analysis above, if a pressure limit of 1 GPa against the explosively driven piston is imposed on the design, the best reservoir configuration is one where the area change section extends all the way to the end of the driver and its length is equivalent to 0.13 times the driver length. It is important to note that while the general observations from the analysis apply to a wide range of launcher designs, the optimum reservoir length to driver length may vary as the driver length and area ratio of the launcher are changed.

Although the gains from decreasing the ratio of reservoir length to driver length appear to be small, due to the limitations of the driver, there is the possibility of using the implosion of the sealing cone as a means to further compress the driver gas. As was described in the Introduction, typical implosion launchers seal the driver gas within the reservoir through the implosion of a steel conical section placed at the end of the driver. The sealing cone is typically three driver diameters in length, and surrounded by a large mass of explosive to ensure proper implosion (see Figure 3–22). As the detonation reaches the sealing cone, the mass of the explosively driven piston increases gradually and its velocity tapers off, eventually coming to a stop. If the driver is designed such that the piston begins to face high pressures (>1 GPa) at the beginning of the sealing cone, it is possible that the increasingly massive explosively driven piston may be able further compress the driver gas despite the increasingly large reservoir pressures. A further compression of three driver diameters represents a reservoir length to driver length of 0.08 in a typical launcher, which according to Figure 5–18, could lead to performance gains of more than 1 km/s.

It is important to note that the sealing cone analysis presented above is somewhat speculative, given the fact that the computational model cannot predict how the driver and sealing cone will interact with the high pressure driver gas. As a result, the variation of reservoir parameters in the implosion launcher must be determined experimentally. Szirti [34] performed a systematic variation of reservoir length to driver length early in the McGill project. However, one should be careful to apply the results to more recent iterations of the implosion launcher which have a significantly different driver geometry, effective projectile density, and sealing cone design. Recent implosion launcher designs in the McGill project have used relatively conservative (long) reservoir lengths, in order to ensure that the sealing cone is not interrupted by the high pressure driver gas. Given that the performance of the sealing cone has been shown to have little effect on launcher performance (see Section 3.3), and that the computational analysis presented above showed the possibility of large performance gains from making slight adjustments to the reservoir length and geometry; it is recommended that experiments be undertaken to verify the possibility of improving launcher performance by reducing the length of the reservoir section and the offset between the area change section and the end of the driver.

5.7 Launcher Mechanical Design

The analysis in this section has focussed on internal ballistics considerations a single stage the implosion launcher. However, the mechanical design of the launcher can have an equally important influence on its performance. Some of the largest performance gains during the McGill project have been brought about by the use of the single piece reservoir and self-sealing projectile, described in the Introduction. Another important mechanical design consideration is the sizing of the reservoir and launch tube. If these components are not made sufficiently large, the driver gas pressures can readily rupture the launcher walls, leading to large performance losses.

During the launch cycle, the driving pressure gradually decays as the projectile travels through the launch tube. As a result, the required launcher wall thickness also tapers off. In order to provide appropriate confinement to the launch tube, the thick reservoir section is extended up to the point where the driving pressure has significantly decayed. It should be noted that stock 4130 steel tubing is typically used for the launch tube, which limits the launch tube external diameter to internal

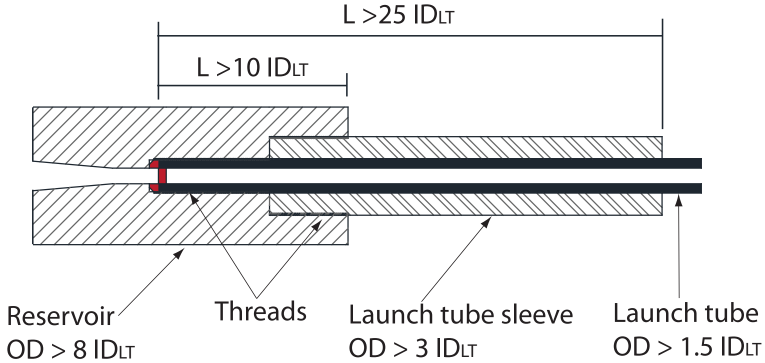

Figure 5–19: Summary of mechanical design recommendations for a typical single stage implosion driven launcher

diameter ratio to approximately two. For this reason, a launch tube sleeve which threads into the end of the reservoir is used to provide intermediate confinement at the point where the full reservoir thickness is not required but the launch tube thickness is not sufficient. A schematic of the launch tube assembly can be seen in Figure 5–19.

The computational model, which simulates the expansion of the reservoir and launch tube, can be a useful tool in ensuring that the reservoir and launch tube sleeve are appropriately sized and extend sufficiently far to prevent the rupture of the launch tube walls. Because the reservoir wall expansion is hydrodynamic, it is expected that a point will be reached where increasing the reservoir wall thickness no longer leads to an appreciable improvement in velocity. Similarly, extending the reservoir past a certain point along the launch tube will also have diminishing returns on performance. Identifying these design criteria is important to maximizing launcher performance while keeping launcher costs reasonable. Figure 5–19 shows the recommended reservoir, sleeve, and launch tube thicknesses and lengths for a typical single stage implosion launcher. The criteria have been non-dimensionalized by the launch tube internal diameter (projectile diameter) to ensure its applicability to a wide range of launcher designs.

5.8 Summary of Single-Stage Launcher Parametric Study

The computational model, supported by experimental data, has been used to draw a number of important conclusions on the design of single stage implosion driven launchers. In order to consolidate the results, the findings have been summarized as a series of design recommendations for a single stage implosion-driven launcher:

1. **Projectile Design:**

   Material: ZK60, high strength magnesium alloy

   Thickness: 0.5 calibers

   Maximum Driving Pressure: 5 GPa

2. **Driver Design**

   Length: 30 to 50 diameters

   Diameter: sufficiently large for a $G/M > 3.5$ (area ratio between launch tube and driver > 5)

   Driver Gas: Helium

   Piston Velocity: as large as possible (use explosive with highest available detonation velocity)

3. **Reservoir Design**

   Length: Reservoir length to driver length ratio of approximately 0.15 (varies with driver geometry)

Area Change Section Geometry: gradual area change that begins at the beginning of the sealing cone and ends 3 launch tube diameters behind the projectile

5.9 Recommended Experiments

The computational analysis has also identified a number of ways to potentially improve launcher performance over the current state of the art McGill launchers. Summaries of proposed changes to the current design are given below:

1. **Area Ratio Variation**

   The optimization of the driver geometry showed that it may be possible to increase the performance of the launcher by increasing the diameter of the driver. According to simulations, gains of 1 km/s can be expected by increasing the area ratio from 5 to 9.

2. **Reservoir Length Variation**

   Recent iterations of McGill launchers have employed relatively conservative (long) reservoir lengths. Although previous experiments reported by Szirti have shown limited gains from decreasing reservoir length, improvements to the sealing cone design and large decreases in effective projectile density in state of the art launchers may increase the gains provided by shortening the reservoir. Simulations indicate that gains of upward of 1 km/s may be possible if a short reservoir length is used in which the sealing cone compresses the reservoir gas, as was described in Section 5.6.3. For these experiments, the distance between the beginning of the sealing cone and the end of the area change section should be approximately 13 percent of the driver length. The area change section should extend to the beginning of the sealing cone.

3. **Piston Velocity Variation**

   According to simulations, gains of up to 0.5 km/s can be expected by increasing the explosively driven piston velocity from 7 to 8 km/s. Further gains may be possible if the driver volume is increased. For this reason, it is recommended that Primasheet 2000, a commercially available explosive with a detonation velocity of 8.2 km/s, be used in place of the Primasheet 1000 (detonation velocity of 7 km/s) that is currently being used for launchers.

4. **Phase Velocity Driver**

   It has been demonstrated that performance gains of 1 km/s may be obtained by using phase velocity techniques to increase the driver piston velocity to 12 km/s. The principal challenge in the design of the phase velocity launcher is providing sufficient driver gas to allow the propellant to reach its theoretical potential. With this in mind, it is recommended that a large driver to launch tube area ratio (> 15) be used in the design of the launcher. A larger driver will provide sufficient driver gas while allowing the maximum driving pressure to be held below 5 GPa.

CHAPTER 6
Velocity Augmentation Techniques

The parametric launcher study performed in the previous section appears to indicate that the performance of a single-stage implosion launcher is unlikely to be able to surpass 10 km/s. Although the initial projectile acceleration in the implosion-driven launcher is very large, it is only sustained for a short period of time due to the rapid decay in driver gas pressure that results from the combined acceleration of the driver gas and expansion of the reservoir. This chapter will present two techniques which can be used to maintain a more constant driving pressure on the projectile.

6.1 Auxiliary Pump Cycle

The auxiliary pump cycle uses explosives to dynamically confine the reservoir. The intense inward pressure applied by the detonating explosive reverses radial expansion and partially implodes the reservoir, which provides additional compression to the driver gas. As was mentioned in Section 1.3.3, Physics International successfully used this technique to improve launcher performance by approximately 4 km/s. However, differences in the projectile and the geometry of the launcher mean that the design and timing of the auxiliary pump cycle cannot be taken directly from this work.

6.1.1 Stress Wave Timing

The effectiveness of the auxiliary pump cycle is strongly dependant on the timing of the explosive initiation. Indeed, initiating the explosives more promptly results in earlier reservoir implosion and less radial expansion before the auxiliary pump cycle. As a result, the projectile feels the benefits of the auxiliary pump cycle earlier and in a more pronounced fashion. The limitation on the auxiliary pump timing is that a strong shock wave is driven into the reservoir by the detonating explosive. This shock wave (or stress wave) can damage the projectile. For this reason, the auxiliary pump must be initiated late enough such that the stress wave never reaches the projectile. Three main parameters affect the timing of the stress wave along the projectile plane: the stress wave velocity, the explosive detonation velocity, and the location of the explosive initiation.

The speed of sound in steel is of approximately 4.6 km/s, which is the propagation velocity of a weak acoustic wave. The speed of the shock wave driven by the detonating explosive will be greater than the speed of sound, and can be determined from the conservation of mass, momentum, and energy. The following expressions can be used to determine the shock wave velocity (U_s) from the explosive detonation pressure (P_1), the density of steel (ρ_o), and the material constants (c_o=4.6 km/s) and (s=1.49) relating the shock wave velocity and the particle velocity behind the shock (U_1) (obtained from experiments) [15, 40].

$$U_s = c_o + sU_1 \tag{6.1}$$

$$P_1 = \rho_o U_1 (c_o + sU_1) \tag{6.2}$$

$$0 = \frac{\rho_o}{s} U_s^2 - \frac{\rho_o c_o}{s} U_s - P_1 \tag{6.3}$$

$$U_s = \frac{\frac{\rho_o c_o}{s} + \left[\left(\frac{\rho_o c_o}{s} \right)^2 + 4 P_1 \frac{\rho_o}{s} \right]^{\frac{1}{2}}}{2 \frac{\rho_o}{s}} \tag{6.4}$$

From these expressions, it can be seen that as the detonation pressure increases, so does the speed of the shock wave driven in the steel. Typical detonation pressures

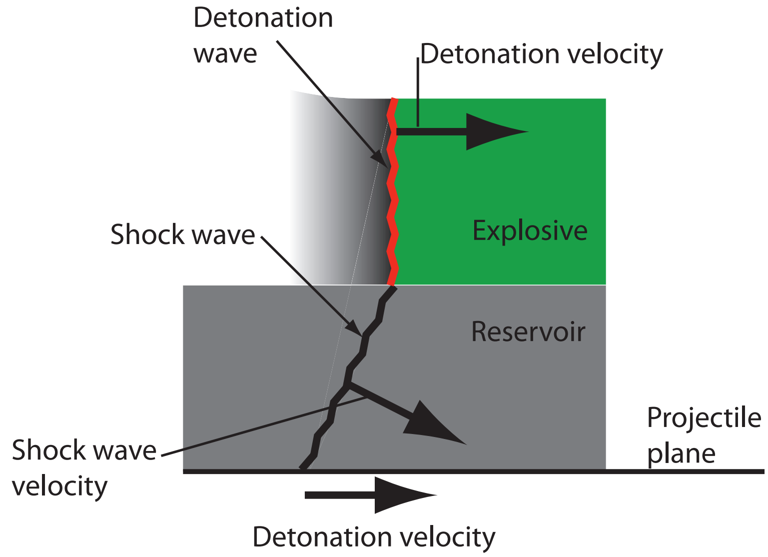

Figure 6–1: Schematic of the dragged (phased) shock wave that results when a detonation wave travels over the reservoir at a velocity which is greater than the shock wave velocity. The resulting shock wave velocity along the projectile plane is equal to the detonation velocity.

of 10 to 30 GPa yield shock wave velocities of 5 to 5.6 km/s in steel. While the propagation velocity of the stress wave in the steel is of approximately 5.5 km/s, the actual arrival velocity of the stress wave along the projectile plane will also depend on the speed at which the detonation wave travels along the surface of the reservoir. As is shown in Figure 6–1, if the detonation velocity is greater than the shock wave propagation velocity in the steel, a tilted (or phased) shock wave is formed which arrives at the projectile plane at the explosive detonation velocity. The principle of wave phasing is described in greater detail in Appendix D.

It can be seen that in attempting to initiate the auxiliary pump as early as possible, there is an advantage to using an explosive with a detonation velocity that is closely matched to the shock wave propagation velocity in the reservoir. Typical explosive detonation velocities vary between 5 and 9 km/s. It is important to note that the detonation velocity of an explosive also has an important effect on the detonation pressure. Cooper [15] showed that the detonation pressure of conventional condensed phase explosives follows the trend in Equation 6.5, indicating that the detonation pressure (P_1) increases roughly with the square of detonation velocity (U_D). For this reason the explosive choice for the auxiliary pump is a compromise between having a sufficiently high detonation pressure to dynamically confine the reservoir while having a relatively low detonation velocity to allow the explosive to be initiated as early as possible. The recommended explosive for this purpose is nitromethane diluted with 30 percent (by mass) of diethylenetriamine, having a detonation velocity of 5.5 km/s and an estimated detonation pressure of 10 GPa. The resulting shock wave velocity in the steel is of 5 km/s.

$$P_1 = \rho_o (U_D)^2 (1 - 0.7125 (\rho_o)^{0.04}) \tag{6.5}$$

It is important to note that the velocity at which the detonation travels along the reservoir surface is also strongly affected by the point at which the detonation is initiated in the explosive. The auxiliary pump typically uses a relatively large explosive thickness (can be > 5 projectile diameters thick). If the explosive is initiated near the top of the auxiliary pump, the apparent arrival velocity of the detonation will be very rapid in the initial stage of the auxiliary pump, as is shown schematically in Figure 6–2. As can be seen, the arrival velocity of the detonation wave is equal to the detonation velocity divided by the sine of the angle between the tangent to the detonation wave and the reservoir surface (θ). This phase velocity effect becomes more pronounced as the height of explosive initiation is increased. This is demonstrated by Figure 6–3, which shows the progression in the apparent detonation velocity of the explosive as a function of position along the reservoir for different

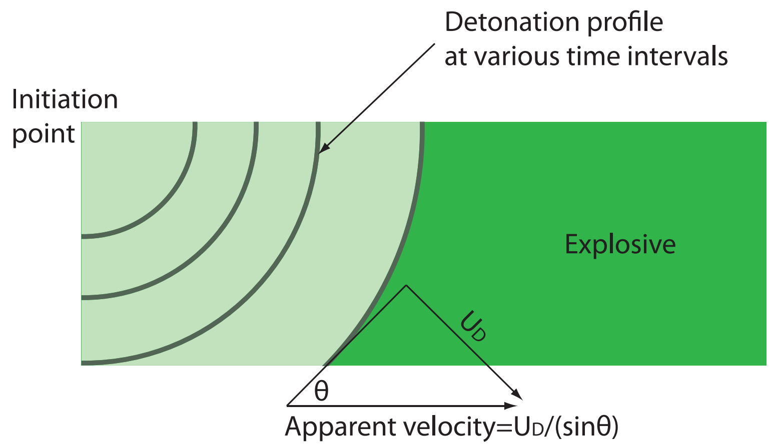

Figure 6–2: Schematic of the phase velocity effect that results from initiating the auxiliary pump above the reservoir surface. The arrival velocity of the detonation wave along the reservoir surface will be higher than the detonation velocity.

initiation heights. In order to mitigate this effect, the explosive should be initiated as close to the surface as possible.

As can be seen, by using an explosive with a low detonation velocity and initiating it near the surface of the reservoir, one can ensure that the auxiliary pump cycle is initiated as early as possible. The internal ballistics solver can be used to determine the delay required such that the stress wave does not overtake the projectile. In Figure 6–4 a position-time diagram shows the propagation of the projectile and the stress wave along the projectile plane. The projectile trajectory is calculated using the internal ballistics model, including reservoir expansion, and heat transfer and gas friction losses. The stress wave trajectory is calculated considering the height of the explosive initiation and assuming a 5.5 km/s propagation velocity in the steel and the explosive (slightly conservative). The delay is chosen such that the stress wave trajectory never overtakes the projectile. A margin of error of 2 to 5 μs is typically added to the calculated delay.

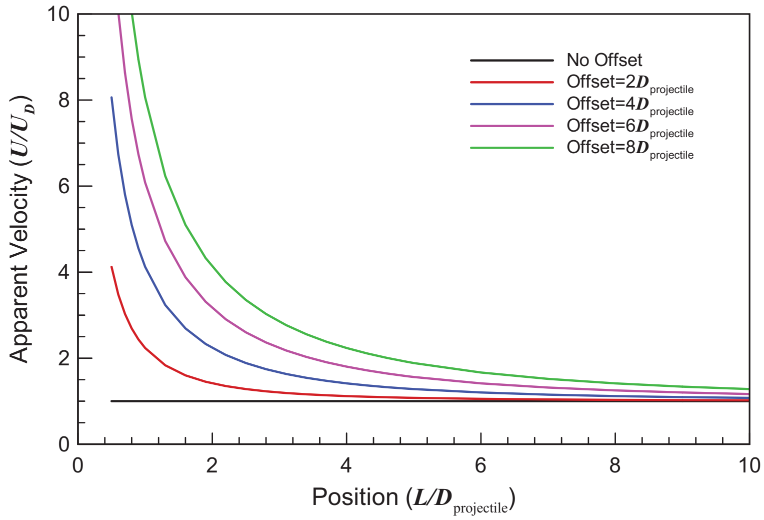

Figure 6–3: Graph showing the effect of the auxiliary pump initiation height on the arrival velocity of the detonation wave along the reservoir surface. The position and velocity axis have been non-dimensionalized by the projectile diameter and the detonation velocity respectively.

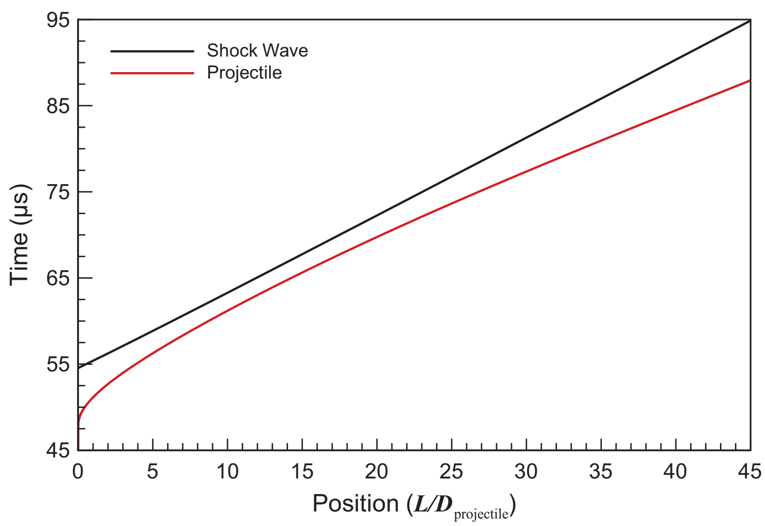

Figure 6–4: Position-time diagram showing the profile of the projectile (obtained from simulations) and the arrival of the stress wave along the projectile plane. These diagrams are used to determine the optimal timing for the initiation of the auxiliary pump cycle.

In performing this analysis, it becomes clear that the time taken for the projectile to reach the propagation velocity of the stress wave along the projectile plane is another important consideration to the auxiliary pump cycle. In launchers where the projectile is accelerated to less than 6.5 km/s, the gains from the auxiliary pump cycle are not likely to be substantial, due to the fact that a long delay must be given before the explosives can be initiated. This limits the use of the auxiliary pump technique to launchers firing projectiles having a low effective density using a large driver gas mass and an elevated maximum driving pressure. It should also be noted that in launchers where the final projectile velocity is much greater than 6.5 km/s, there may be an advantage to using a faster explosive near the end of the auxiliary pump to allow the reservoir implosion to follow the projectile as closely as possible.

6.1.2 Auxiliary Pump Experiments

Although a number of experiments incorporating an auxiliary pump cycle have been performed during the McGill project, a large number of these have been unsuccessful, resulting in broken projectiles or limited velocity gains. It is believed that a number of these failures were caused by using a reservoir having too large a diameter. Although the diameter of the reservoir must made large enough to provide confinement in the early stages of projectile acceleration, there are two important consequences to making the reservoir wall thickness too large. If the reservoir is too thick, the implosion caused by the detonating explosive will be too weak to significantly compress the driver gas. Furthermore, due to phase velocity effects discussed in the previous section, increasing the reservoir wall thickness can result in an important increase in the apparent arrival velocity of the shock wave along the projectile plane in the beginning of the auxiliary pump. Experiments performed by McGill and Physics International [38] have shown that reservoirs having a diameter

Table 6–1: Summary of two launcher experiments comparing the performance of an implosion-driven launcher with and without an auxiliary pump cycle

Projectile Mass (g)	Velocity (km/s)	Launch Tube Diameter (mm)	Projectile	Driver Fill Pressure (MPa)	Driver to Launch Tube Area Ratio	Driver Length (L/D)	Reservoir to Driver Length Ratio
0.1	8.0	5	0.5 cal. ZK60	4.0	4.4	37	0.15

Projectile Mass (g)	Velocity (km/s)	Driver Fill Pressure (MPa)	Reservoir Diameter (D_r/D_p)	Reservoir Mass to Explosive Mass (M/C)	Projectile to End of Explosives (L/D_p)
0.1	9.1	4	6.5	0.96	20

equivalent to six times the projectile diameter result in acceptable auxiliary pump performance. It should be noted that it may be possible to improve performance by further decreasing the diameter of the reservoir beyond this value.

The most successful auxiliary pump shot is presented in Table 6–1, which summarises a series of experiments in which a direct comparison of the performance of a launcher with and without an auxiliary pump was performed. The geometry of the launchers is identical, and both launchers fired similar projectiles at similar initial fill pressures. As can be seen, the use of the auxiliary pump resulted in a performance gain of 1.1 km/s. A picture of the launcher as well as a drawing showing a cross sectional view of the reservoir can be seen in Figure 6–5. A 7.1 km/s sheet explosive (Primasheet 1000) was used for the auxiliary pump. Due to the geometry of the launcher, the explosive was initiated at the top of the explosive thickness. A safety margin of approximately 2 μs was used from the stress wave criteria to determine the timing for the initiation of the explosive.

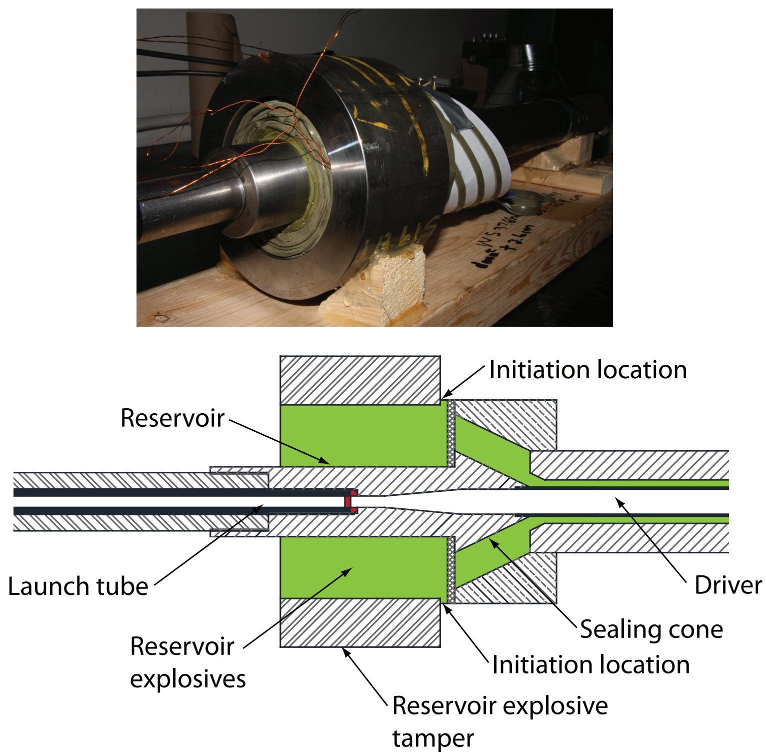

Figure 6–5: Cross sectional view of the arrangement of the auxiliary pump experiment. A picture of the reservoir explosive arrangement is also shown.

6.1.3 Future Work

As was mentioned, the auxiliary pump shot presented in the previous section used an explosive having a detonation velocity of 7.1 km/s and was initiated at the top of the explosive layer. Future experiments are being prepared in which a 5.5 km/s explosive (70 percent nitromethane, 30 percent diethylenetriamine by mass) will be used and initiated near the base of the explosive layer. These design changes will allow the auxiliary pump to be initiated 6.5 μs earlier, which may lead to a significant improvement in launcher performance.

It is also possible that significant gains could be made by varying the reservoir thickness, explosive thickness, and length of explosive, as well as looking at using a fast explosive near the end of the auxiliary pump cycle. A computational model capable of simulating the effect of the auxiliary pump on reservoir expansion would be an important asset in optimizing the geometry of the reservoir explosives. The hydrocode developed in Section 3.1 could be adapted to simulate the auxiliary pump cycle.

6.2 Accelerating Driver Piston

The launch cycle of the conventional implosion-driven launcher is relatively inefficient, due to the fact that the driver gas receives little compression after the projectile has been set in motion. As a result, the projectile driving pressure decays very quickly and the launcher has a poor piezometric efficiency (ratio of average projectile driving pressure divided by maximum projectile driving pressure). This means that further increasing the speed of sound of the driver gas or the maximum projectile driving pressure will have limited benefits on performance, as was seen in Chapter 5. In order to significantly improve performance, one needs to find a way to further compress the driver gas in the initial stages of projectile acceleration, thus

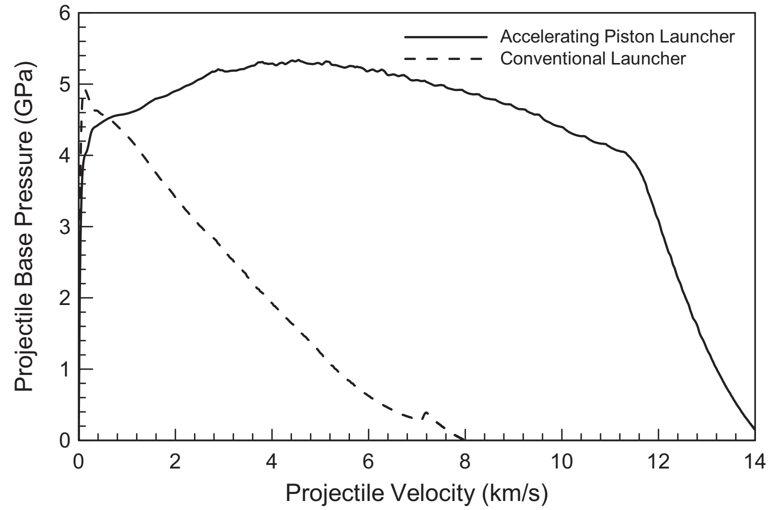

Figure 6–6: Comparison of the predicted evolution of the projectile driving pressure in an accelerating driver piston launcher and a conventional implosion-driven launcher. The simulations include reservoir expansion and heat transfer and gas friction losses.

providing a higher average projectile driving pressure. This can be accomplished by gradually increasing the velocity of the explosively driven piston.

The use of velocity phasing techniques (described in Appendix D) allows for the possibility of providing a gradual acceleration to the explosively driven piston. Loiseau et al. [23] showed that the detonation velocity in a linear explosive driver can be phased to twice the detonation velocity while maintaining reasonably good driver performance. Using the internal ballistics solver for the implosion launcher, it is possible to look at the effect of accelerating the explosively driven piston to twice the detonation velocity during the launch cycle. Figure 6–6 shows the resulting predicted projectile driving pressure as a function of velocity. The profiles for a conventional implosion launcher are also shown. The simulations include reservoir expansion and heat transfer and gas friction losses. The driver is assumed to operate ideally.

As can be seen, the accelerating piston allows for a significant increase in the average projectile driving pressure, resulting in a predicted projectile velocity approaching 14 km/s. It is important to reiterate that the simulation assumes that the accelerating piston driver operates ideally. In reality, accelerating the explosively-driven piston may lead to a loss of driver gas which could limit the benefits of the accelerating piston scheme. Nonetheless, this approach appears promising and warrants further experimental development.

CHAPTER 7
Conclusion

The ability to launch relatively large and well characterized projectiles to velocities above 10 km/s is of interest for a number of scientific fields, including orbital debris impact simulation. It appears that the implosion-driven launcher may be capable of reaching this performance envelope. In this work, an internal ballistics solver capable of simulating the launch cycle of the implosion-driven launcher has been developed. The solver includes models for the radial expansion of the launcher walls and the non-ideal operation of the explosive pump tube, two non-ideal effects that are unique to the implosion-driven launcher. The solver has been validated against launcher experiments to ensure its validity over a wide range of designs. The non-ideal effect models were observed to significantly improve the agreement between the solver and experiments. The solver has helped identify radial expansion of the launcher walls as the main source of performance loss for the implosion-driven launcher.

The solver was used in conjunction with ideal internal ballistics theory and experimental results to perform a parametric study of the design of an implosion-driven launcher. A number of measures were identified to improve the performance of current state of the art McGill launchers. A study of velocity augmentation techniques was undertaken in an effort to design a launcher capable of reaching the target performance envelope. The use of reservoir explosives allowed the McGill launcher to reach a velocity of 9.1 km/s. The accelerating piston scheme, in which the explosively-driven piston is accelerated during the launch cycle may allow the launcher to operate more efficiently and reach velocities well beyond 10 km/s.

Appendix A – Nomenclature

Although an effort has been made to identify variables in the text, this section provides an overview of the nomenclature for commonly used variables.

U	Velocity
X	Position
t	Time
v	Specific Volume
ρ	Density
e	Specific Internal Energy
q	Artificial Viscosity
p	Pressure
a	Speed of Sound
m	Mass
r	Radius
f	Friction Factor
h	Enthalpy
T	Temperature
R	Specific Ideal Gas Constant
MW	Molecular Weight
M	Mach Number
μ	Dynamic Viscosity
γ	Specific Heat Ratio
D	Diameter
L	Length

L/D Aspect Ratio

V Volume

ϵ Strain

s Deviatoric Stress

r Radius

Y_o Yeild Strength

Subscripts

j Cell Index

n Timestep Index

Appendix B – Self-Sealing Projectile Design

This section presents the design of the self sealing projectile used for the implosion-driven launcher. Self sealing projectiles enable the sealing of the initial driver gas pressure without the need for a separate fast acting valve. This ensures that the projectile will not be damaged by the fast acting valve or resulting flow asymmetries during the rupture of the valve. The projectile is initially held in place by a sacrificial web, which instantly shears when exposed to the reflected shock pressure. Given that the pressure ratio across the reflected shock wave is approximately 1000, the web can be made very thin, thus ensuring that the initial projectile acceleration is essentially unaffected by the shearing of the web. A general overview of the self sealing projectile is given in Figure 7–1. Attached to the projectile (cylindrical body) is a tab which rests on the launch tube face to hold the projectile in place. This tab has a chamfer which is used to seal against a corner o-ring. The back of the tab has been bored out to a slightly greater diameter than the projectile. This exposes a thin web, having a thickness equal to the difference between the bore depth and the tab thickness. Equation 7.1 shows the calculation for the minimum web thickness (t_w), in terms of the initial fill pressure (P), and the launch tube diameter (D_{LT}). As can be seen, the shear stress (τ), is calculated from the pressure force acting on the projectile (F), and the area over which the shear stress is applied (A). Typically a safety factor (SF) of 1.5 to 2 is used to ensure the web will not fail under the initial driver gas pressure.

$$SF = \frac{Y_o}{\sqrt{3}\tau} = \frac{Y_o}{\sqrt{3}}\frac{A}{F} = \frac{Y_o}{\sqrt{3}}\left(\frac{\pi D_{LT} t_w}{P\frac{\pi D_{LT}^2}{4}}\right) = \frac{Y_o}{\sqrt{3}}\left(\frac{4t_w}{PD_{LT}}\right) \tag{7.1}$$

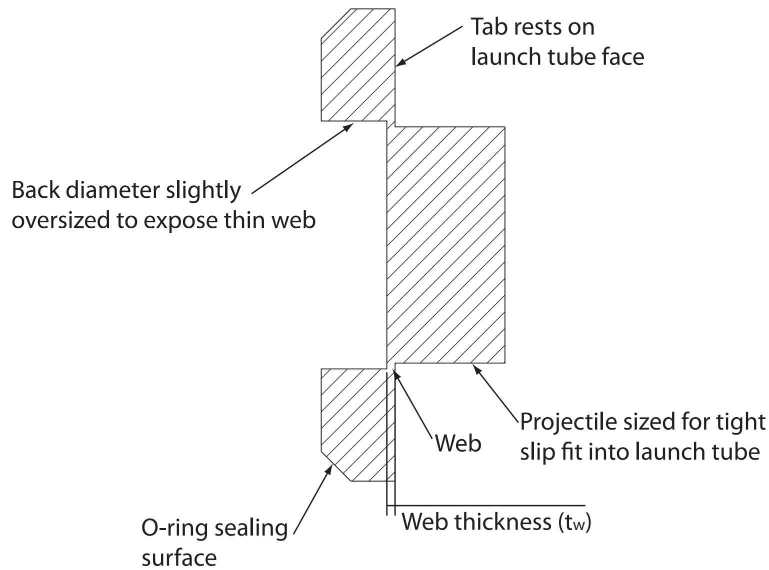

Figure 7–1: Detailed drawing of a self sealing projectile cross-section showing the main features of the design

$$t_w = SF = \frac{\sqrt{3}\tau}{Y_o}\left(\frac{PD_{LT}}{4}\right) \tag{7.2}$$

A note should be made regarding the fit of the projectile in the barrel. In an unconfined environment, the pressure on the face of the projectile during the launch cycle would lead to significant radial strain (Poisson expansion). The question arises as to whether it is favourable to undersize the projectile to allow for radial expansion, or to fit the projectile to the barrel diameter to allow it to be constrained by the launch tube walls. By under-sizing the projectile, it is possible to reduce stresses caused by friction between the launch tube walls and the projectile. However, under-sizing the projectile also reduces the level of radial confinement provided by the launch tube walls. This confinement places the projectile in a state of hydrostatic stress, which is believed to be the reason why it can withstand driving pressures that are an order of magnitude higher than its yield strength [9]. Admittedly, this issue has yet to be resolved. For the McGill project, projectiles are generally fit to provide a tight slip fit into the barrel (undersized by < 0.03 mm), in order to maximize the radial confinement of the projectile. While some projectile material surely ablates as the pressurized projectile travels down the launch tube (due to the large radial stresses confining the projectile), this has not been observed to affect its integrity.

Appendix C – Radial Hydrocode Finite Difference Equations

This section will present the finite difference equations for the radial hydrocode. The equations are based on the scheme presented by Wilkins [40]. It should be noted that for convenience of use in the equation of state, the equations are written using the relative specific volume (v/v_o), the internal energy per original volume (e/V_o), and the mass per unit length (kg/m). ρ_o denotes the initial density of the material being studied.

Cell Mass

$$m_{j-1/2} = \frac{\rho_o}{2}\left[(r_j^{n=1})^2 - (r_{j-1}^{n=1})^2\right] \tag{7.3}$$

Conservation of Momentum

$$U_j^{n+1/2} = U_j^{n-1/2} + \frac{\frac{1}{2}(\Delta t^n + \Delta t^{n-1})}{\Phi_j^n}\left[(\Sigma_r)_{j+1/2}^n - (\Sigma_r)_{j-1/2}^n\right] + \frac{1}{2}(\Delta t^n + \Delta t^{n-1})\beta_j^n \tag{7.4}$$

$$\Phi_j^n = \frac{1}{2}\left[\rho_o\left(\frac{r_{j+1}^n - r_j^n}{v_{j+1/2}^n}\right) + \rho_o\left(\frac{r_j^n - r_{j-1}^n}{v_{j-1/2}^n}\right)\right]$$

$$(\Sigma_r)_{j-1/2}^n = \left[-(p_{j-1/2}^n + q_{j-1/2}^{n-1/2}) + (s_1)_{j-1/2}^n\right]$$

$$(\Sigma_\theta)_{j-1/2}^n = \left[-(p_{j-1/2}^n + q_{j-1/2}^{n-1/2}) + (s_2)_{j-1/2}^n\right]$$

$$\beta_j^n = \left(\left[\frac{(\Sigma_r)_{j+1/2}^n - (\Sigma_\theta)_{j+1/2}^n}{\frac{1}{2}(r_{j+1}^n + r_j^n)}\right]\left(\frac{v_{j+1/2}^n}{\rho_o}\right) + \left[\frac{(\Sigma_r)_{j-1/2}^n - (\Sigma_\theta)_{j-1/2}^n}{\frac{1}{2}(r_j^n + r_{j-1}^n)}\right]\left(\frac{v_{j-1/2}^n}{\rho_o}\right)\right)$$

Cell Boundary Position

$$r_j^{n+1} = r_j^n + U_j^{n+1/2}\Delta t^n \tag{7.5}$$

Specific Volume

$$v_{j-1/2}^{n+1} = \frac{1}{2}\frac{\rho_o}{m_{j-1/2}}[(r_j^{n+1})^2 - (r_{j-1}^{n+1})^2] \tag{7.6}$$

Strain Rate

$$(\dot{\epsilon}_1)_{j-1/2}^{n+1/2} = \frac{U_j^{n+1/2} - U_{j-1}^{n+1/2}}{r_j^{n+1/2} - r_{j-1}^{n+1/2}} \tag{7.7}$$

$$(\dot{\epsilon}_2)^{n+1/2}_{j-1/2} = \frac{U^{n+1/2}_j + U^{n+1/2}_{j-1}}{r^{n+1/2}_j + r^{n+1/2}_{j-1}} \tag{7.8}$$

Principal Stress Deviators

$$(s_1)^{n+1}_{j-1/2} = (s_1)^n_{j-1/2} + 2G\left[(\dot{\epsilon}_1)^{n+1/2}_{j-1/2}\Delta t^n - \frac{2}{3}\left(\frac{V^{n+1}_{j-1/2} - V^n_{j-1/2}}{V^{n+1}_{j-1/2} + V^n_{j-1/2}}\right)\right] \tag{7.9}$$

$$(s_2)^{n+1}_{j-1/2} = (s_2)^n_{j-1/2} + 2G\left[(\dot{\epsilon}_2)^{n+1/2}_{j-1/2}\Delta t^n - \frac{2}{3}\left(\frac{V^{n+1}_{j-1/2} - V^n_{j-1/2}}{V^{n+1}_{j-1/2} + V^n_{j-1/2}}\right)\right] \tag{7.10}$$

$$(s_3)^{n+1}_{j-1/2} = -\left[(s_1)^{n+1}_{j-1/2} + (s_2)^{n+1}_{j-1/2}\right] \tag{7.11}$$

G is the shear modulus

Local Yeild Stress (Constitutive Model)

$$(Y_o)^n_{j-1/2} = [A(1 + B((\sigma^p_{eq})^n_{j-1/2})^N][1 + Cp^n_{j-1/2}(v^n_{j-1/2})^{1/3} - h(T^n_{j-1/2} - 300)] \tag{7.12}$$

$T^n_{j-1/2} = \frac{\frac{e^n_{j-1/2}}{\rho_o} - \epsilon_o}{3R}$

A,B,N, C, h, R, ϵ_o are constants given in Section 3.1.2.3

Yeild Criterion

IF

$$\sqrt{\frac{3}{2}(((s_1)^{n+1}_{j-1/2})^2 + ((s_2)^{n+1}_{j-1/2})^2 + ((s_3)^{n+1}_{j-1/2})^2)} = (\sigma^*_{eq})^{n+1}_{j-1/2} \geq (Y_o)^{n+1}_{j-1/2} \tag{7.13}$$

THEN

$$(s_1)^{n+1}_{j-1/2} = s1^{n+1}_{j-1/2}\frac{(Y_o)^n_{j-1/2}}{(\sigma^*_{eq})^n_{j-1/2})} \tag{7.14}$$

$$(s_2)^{n+1}_{j-1/2} = s2^{n+1}_{j-1/2}\frac{(Y_o)^n_{j-1/2}}{(\sigma^*_{eq})^n_{j-1/2})} \tag{7.15}$$

$$(s_3)^{n+1}_{j-1/2} = s3^{n+1}_{j-1/2}\frac{(Y_o)^n_{j-1/2}}{(\sigma^*_{eq})^n_{j-1/2})} \tag{7.16}$$

$$(\Delta\epsilon^p_{eq})^{n+1}_{j-1/2} = \left(\frac{(\sigma^*_{eq})^{n+1}_{j-1/2}}{(Y_o)^n_{j-1/2}} - 1\right)\frac{1}{3G}(Y_o)^n_{j-1/2} \tag{7.17}$$

Artificial Viscosity

IF $U_{j-1}^{n+1/2} > U_j^{n+1/2}$

$$q_{j-1/2}^{n+1/2} = \frac{C_0\rho_o}{v_{j-1/2}^{n+1/2}}(U_{j-1}^{n+1/2} - U_j^{n+1/2})^2 + C_1\frac{a_{j-1/2}^{n+1/2}\rho_o}{v_{j-1/2}^{n+1/2}}(U_{j-1}^{n+1/2} - U_j^{n+1/2}) \tag{7.18}$$

ELSE

$$q_{j-1/2}^{n+1/2} = 0 \tag{7.19}$$

$a_{j-\frac{1}{2}}^{n+\frac{1}{2}} = \left[\left(\frac{\partial p}{\partial \rho}\right)_{e=\text{const}} + \frac{p}{\rho^2}\left(\frac{\partial p}{\partial e}\right)_{\rho=\text{const}}\right]^{\frac{1}{2}}$

$\left(\frac{\partial p}{\partial \rho}\right)_{e=\text{const}} = k_1\frac{(v_{j-\frac{1}{2}}^{n+\frac{1}{2}})^2}{\rho_o} + 2k_2(1 - v_{j-\frac{1}{2}}^{n+\frac{1}{2}})\frac{(v_{j-\frac{1}{2}}^{n+\frac{1}{2}})^2}{\rho_o} + 3k_3(1 - v_{j-\frac{1}{2}}^{n+\frac{1}{2}})^2\frac{(v_{j-\frac{1}{2}}^{n+\frac{1}{2}})^2}{\rho_o}$

$\frac{p}{\rho^2}\left(\frac{\partial p}{\partial e}\right)_{\rho=\text{const}} = \frac{p_{j-1/2}^n(v_{j-1/2}^n)^2}{(\rho_o)^2}\gamma_o$

$v_{j-1/2}^{n+1/2} = \frac{1}{2}(v_{j-1/2}^{n+1} + v_{j-1/2}^n)$

C_0 and C_1 are the artificial viscocity constants (see Section 2.1)

Wilkins [40] recomends setting C_0 to 4 and C_1 to 1

k_1,k_2,k_3,γ_o are equation of state constants (see Section 3.1.2.2)

Internal Energy

$$e_{j-1/2}^{n+1} = \frac{e_{j-1/2}^n - \left(\frac{1}{2}(A + p_{j-1/2}^n) + q_{j-1/2}^n\right)(v_{j-1/2}^{n+1} - v_{j-1/2}^n) + Z}{1 + \frac{1}{2}B(v_{j-1/2}^{n+1} - v_{j-1/2}^n)} \tag{7.20}$$

A and B can be found using the equation of state constants:

$A = k_1(1 - v_{j-1/2}^{n+1}) + k_2(1 - v_{j-1/2}^{n+1})^2 + k_3(1 - v_{j-1/2}^{n+1})^3$

$B = \gamma_o$

Z is the increase in shear distortion energy $Z_{j-1/2}^{n+1/2} = v_{j-1/2}^{n+1/2}(s_1\dot{\epsilon}_1 + s_2\dot{\epsilon}_2)_{j-1/2}^{n+1/2}\Delta t^n$

$q^n = \frac{1}{2}(q^{n-1/2} + q^{n+1/2})$

$v^{n+1/2} = \frac{1}{2}(v^n + v^{n+1})$

$s_1^{n+1/2} = \frac{1}{2}(s_1^n + s_1^{n+1})$

$s_2^{n+1/2} = \frac{1}{2}(s_2^n + s_2^{n+1})$

Pressure

$$p^{n+1}_{j-1/2} = k_1(1 - v^{n+1}_{j-1/2}) + k_2(1 - v^{n+1}_{j-1/2})^2 + k_3(1 - v^{n+1}_{j-1/2})^3 + \gamma_o e^{n+1}_{j-1/2} \tag{7.21}$$

k_1,k_2,k_3,γ_o are equation of state constants (see Section 3.1.2.2)

Next Timestep

$$\Delta t^{n+1}_{j-1/2} = \frac{2}{3} \frac{r^{n+1}_j - r^{n+1}_{j-1}}{\sqrt{(a^{n+1}_{j-1/2})^2 + (b^{n+1}_{j-1/2})^2}} \tag{7.22}$$

$a^{n+1}_{j-1/2} = \left[\left(\frac{\partial p}{\partial \rho}\right)_{e=\text{const}} + \frac{p}{\rho^2}\left(\frac{\partial p}{\partial e}\right)_{\rho=\text{const}} \right]^{\frac{1}{2}}$

$\left(\frac{\partial p}{\partial \rho}\right)_{e=\text{const}} = k_1 \frac{(v^{n+1}_{j-\frac{1}{2}})^2}{\rho_o} + 2k_2(1 - v^{n+1}_{j-\frac{1}{2}}) \frac{(v^{n+1}_{j-\frac{1}{2}})^2}{\rho_o} + 3k_3(1 - v^{n+1}_{j-\frac{1}{2}})^2 \frac{(v^{n+1}_{j-\frac{1}{2}})^2}{\rho_o}$

$\frac{p}{\rho^2}\left(\frac{\partial p}{\partial e}\right)_{\rho=\text{const}} = \frac{p^{n+1}_{j-1/2}(v^{n+1}_{j-1/2})^2}{(\rho_o)^2}\gamma_o$

$b^{n+1}_{j-1/2} = 8(C_0 + C_1)(r^{n+1}_j - r^{n+1}_{j-1}) \left(\frac{v^{n+1}_{j-1/2} - v^n_{j-1/2}}{\frac{1}{2}\Delta t^n (v^{n+1}_{j-1/2} + v^n_{j-1/2})} \right)$

Choose the smallest Δt

Appendix D – Phase Velocity

In order to implement the accelerating-piston launcher scheme, one must find a way to vary the velocity of the explosively driven piston with an explosive that has a constant detonation velocity. This can be done by phasing (tilting) the detonation wave. Phase velocity can be explained using a vector diagram. As can be seen in Figure 7–2, when a wave is tilted by an angle θ with respect to the observation plane, the apparent arrival velocity of the wave at the plane is equal to the wave velocity divided by $\sin\theta$. When θ is 90°, there is no tilting (phasing) and the velocity along the observation plane is equal to the wave velocity. As θ is reduced, the apparent wave velocity gradually increases. In fact, for a wave coming directly towards the observation plane ($\theta = 0°$), the arrival velocity appears to be infinite. Using this concept, one can progressively tilt the detonation wave, allowing the velocity of the explosive pinch along the barrel to accelerate with the projectile. It should be noted that while the detonation wave can be made to travel at arbitrarily high velocities along the driver tube, the maximum velocity of the explosively driven piston is limited by the implosion velocity. Watson performed an analytical analysis showing that the explosively driven piston aspect ratio gets very large for phase velocities greater than twice the detonation velocity, which places a practical limit of approximately 20 km/s on the explosively driven piston [38]. Driver experiments performed by Loiseau et al. [23] showed that a precursor shock wave could be formed ahead of a 16 km/s piston using a 6 km/s explosive (2.7 time the detonation velocity). However, it should be noted that the performance of drivers at phase velocities beyond 2 times the detonation velocity were quite poor. Although a number of techniques exist to provide a phased detonation wave, only the most relavent technique to

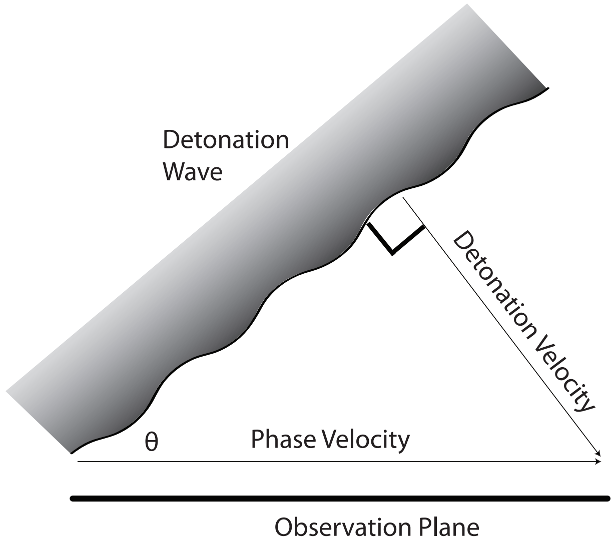

Figure 7–2: Vector diagram showing the phase velocity as a function of wave velocity and phase angle

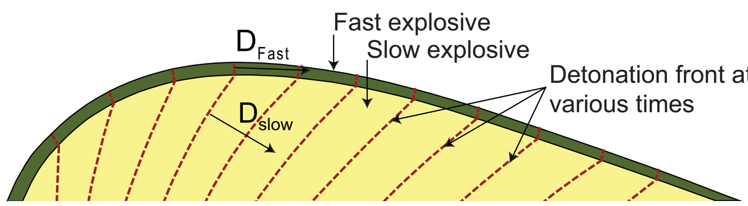

Figure 7–3: Schematic of a two component explosive lens

the accelerating piston launcher will be presented. The explosive lens, pictured in Figure 7–3, operates by having a high detonation velocity explosive drag a detonation wave into a low detonation velocity explosive. The phase velocity is determined by the angle between the fast explosive contour and the observation plane. For example, if the fast explosive is placed parallel to the observation plane (or launch tube) the phase velocity is equal to the detonation velocity of the fast explosive. As can be seen in Figure 7–3, by gradually curving the fast explosive towards the observation plane, it is possible to gradually increase the phase velocity (or phase angle) from the slow explosive detonation velocity ($\theta = 90°$) to an effectively infinite velocity.

References

[1] "Orbital debris: A technical assessment." Tech. rep., National Reserach Council, 1995.

[2] "Limiting future collision risk to spacecraft: An assessment of NASA's meteoroid and orbital debris programs." Tech. rep., National Research Council, 2011.

[3] "Orbital debris quarterly news." Volume 15, Issue 1, Page 10, 2011.

[4] Y. V. Bat'kov, N. P. Kovalev, A. D. Kovtun, V. G. Kuropatkin, A. I. Lebedev, Y. M. Makarov, S. F. Manachkin, S. A. Novikov, V. A. Raevsky, and Y. M. Styazhkin. "Explosive three-stage launcher to accelerate metal plates to velocities more than 10 km/s." *International Journal of Impact Engineering*, vol. 20, no. 15, 1997, pp. 89–92.

[5] D.W. Baum. "Development of explosively driven launcher for meteoroid studies." Tech. Rep. NASA CR-2143, Physics International Company, 1973.

[6] D.W. Baum. "Explosively driven hypervelocity launcher second-stage augmentation techniques." Tech. Rep. PIFR-245-1, Physics International Company, March 1973.

[7] B.I. Bennett, J.D. Johnson, G.I. Kerley, and G.T. Rood. "Recent developments in the SESAME equation-of-state library." Tech. Rep. LA-7130, Los Alamos Scientific Laboratory, 1978.

[8] R. E. Berggren and R. M. Reynolds. "The light-gas-gun model launcher." Tech. Rep. 19710004103, NASA - Ames Research Center, 1970.

[9] H. Bernier. *Scaling and Designing Large-Bore Two-Stage High Velocity Guns*, chap. 2. High-Pressure Shock Compression of Condensed Matter. Springer Berlin Heidelberg, 2005, pp. 37–83.

[10] D.W. Bogdanoff. "CFD modelling of bore erosion in two-stage light gas guns." Tech. Rep. NASA/TM-1998-112236.

[11] D.W. Bogdanoff and R.J. Miller. "New higher-order Godunov code for modelling performance of two-stage light gas guns." Tech. Rep. NASA Technical Memorandum 110363, 1995.

[12] A. C. Charters. "Development of the high-velocity gas-dynamics gun." *International Journal of Impact Engineering*, vol. 5, no. 14, 1987, pp. 181–203.

[13] L. C. Chhabildas, L. N. Kmetyk, W. D. Reinhart, and C. A. Hall. "Enhanced hypervelocity launcher - capabilities to 16 km/s." *International Journal of Impact Engineering*, vol. 17, no. 13, 1995, pp. 183–194.

[14] E. L. Christiansen, J. L. Crews, J. E. Williamsen, J. H. Robinson, and A. M. Nolen. "Enhanced meteoroid and orbital debris shielding." *International Journal of Impact Engineering*, vol. 17, no. 13, 1995, pp. 217–228.

[15] P. W. Cooper. *Explosives Engineering.* Wiley-VCH, 1996.

[16] J.K. Crosby and S.P. Gill. "Feasibility study of an explosive gun." Tech. Rep. NASA CR-709, Physics International Company, April 1967.

[17] Y. I. Fadeenko, V. F. Lobanov, V. V. Silvestrov, and V. M. Titov. "High speed gas flows in explosions of cavitated explosives." *Acta Astronautica*, vol. 1, no. 910, 1974, pp. 1171–1179.

[18] H. D. Fair. "Electromagnetic launch: a review of the U.S. national program." *Magnetics, IEEE Transactions on*, vol. 33, no. 1, 1997, pp. 11–16.

[19] L.A. Glenn. "On how to make the fastest gun in the west." International Workshop on New Models and Numerical Codes, Oxford, United Kingdom, 15-19 Sep 1997.

[20] G. R. Johnson and W. H. Cook. "A constitutive model and data for metals subjected to large strains, high strain rates and high temperatures." 7th International Symposium on Ballistics, The Hague, The Netherlands, April 1983.

[21] G. E. Jones, J. E. Kennedy, and L. D. Bertholf. "Ballistics calculations of R. W. Gurney." *American Journal of Physics*, vol. 48, no. 4, 1980, pp. 264–269.

[22] D. J. Kessler and B. G. Cour-Palais. "Collision frequency of artificial satellites: The creation of a debris belt." *J. Geophys. Res.*, vol. 83, no. A6, 1978, pp. 2637–2646.

[23] J. Loiseau, J. Huneault, M. Serge, A. Higgins, and V. Tanguay. "Phase velocity enhancement of linear explosive shock tubes." *AIP Conference Proceedings*, vol. 1426, no. 1, 2012, pp. 493–496.

[24] J. Loiseau, D. Szirti, A. Higgins, and V. Tanguay. "Experimental technique for generating fast high-density shock waves with phased linear explosive shock tubes." *Shock Waves*, vol. 22, no. 1, 2012, pp. 85–88.

[25] H. Mirels. "Shock tube test time limitation due to turbulent wall boundary layer." Tech. Rep. TDR-169(3230- lZ)TR-3, Aerodynamics and Propulsion Research Laboratory, 1963.

[26] E.T. Moore. "Explosive hypervelocity launchers." Tech. Rep. NASA CR-982, Physics International Company, 1968.

[27] W. F. Noh. "Errors for calculations of strong shocks using an artificial viscosity and an artificial heat flux." *Journal of Computational Physics*, vol. 72, no. 1, 1987, pp. 78–120.

[28] J. V. Parker. "Why plasma armature railguns don't work (and what can be done about it)." *Magnetics, IEEE Transactions on*, vol. 25, no. 1, 1989, pp. 418–424.

[29] A. J. Piekutowski and K. L. Poormon. "Development of a three-stage, light-gas gun at the University of Dayton Research Institute." *International Journal of Impact Engineering*, vol. 33, no. 112, 2006, pp. 615–624.

[30] K. Seifert. "Feasibility study of explosively driven hypervelocity projectiles." Tech. Rep. PIFR-559, Physics International Company, April 1974.

[31] A. E. Seigel. *The Theory of High Speed Guns*, vol. AGARDograph 91. AGARDograph, 1965.

[32] A. E. Seigel. *Theory of High-Muzzle-Velocity Guns*. Interior Ballistics of Guns. American Institute of Aeronautics and Astronautics, New York, 1979.

[33] M. Serge, J. Loiseau, J. Huneault, D. Szirti, A. Higgins, and V. Tanguay. "Implosion-driven technique to create fast shockwaves in high-density gas." *AIP Conference Proceedings*, vol. 1426, no. 1, 2012, pp. 489–492.

[34] D. Szirti. "Development of a single-stage implosion-driven hypervelocity launcher." Master's Thesis, 2008.

[35] D. Szirti. "Dynamics of explosively imploded pressurized tubes." *J. Appl. Phys.*, vol. 109, no. 8, 2011, p. 084526.

[36] J. von Neumann and R. D. Richtmyer. "A method for the numerical calculation of hydrodynamic shocks." *Journal of Applied Physics*, vol. 21, no. 3, 1950, pp. 232–237.

[37] J. D. Walker, D. J. Grosch, and S. A. Mullin. "A hypervelocity fragment launcher based on an inhibited shaped charge." *International Journal of Impact Engineering*, vol. 14, no. 14, 1993, pp. 763–774.

[38] J.D. Watson. "High-velocity explosively driven guns." Tech. Rep. NASA CR-1533, Physics International Company, 1970.

[39] J.D. Watson. "A summary of the development of large explosive guns for reentry simulation." Tech. Rep. PIFR-155, Physics International Company, August 1970.

[40] M. L. Wilkins. *Computer Simulation of Dynamic Phenomena*. Springer, 1999.

[41] P. Woodward and P. Colella. *High resolution difference schemes for compressible gas dynamics*, vol. 141 of *Lecture Notes in Physics*, chap. 67. Springer Berlin Heidelberg, 1981, pp. 434–441.